UNIVERSITY OF TRENTO

Doctoral School in Civil, Environmental and
Mechanical Engineering

Curriculum 1. Civil and Environmental Engineering

Federica Gucci

Experimental and numerical investigation of turbulence in Stable Boundary Layer flows

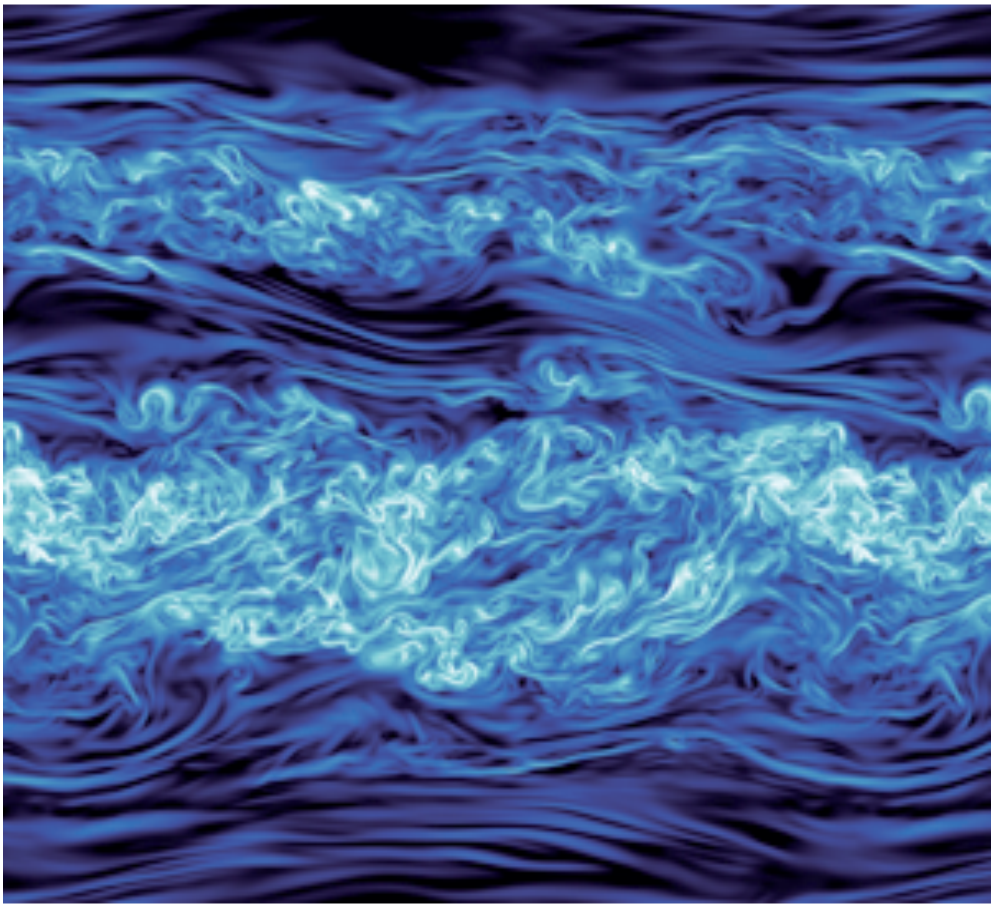

2023 - Doctoral thesis

UNIVERSITY OF TRENTO - Italy
Department of Civil, Environmental and Mechanical Engineering

Doctoral School in Civil, Environmental and Mechanical Engineering
Topic 1. Civil and Environmental Engineering - XXXIV cycle 2018/2021

Doctoral Thesis – February 2023

Federica Gucci

Experimental and numerical investigation of turbulence in Stable Boundary Layer flows

Supervisors
Prof. Lorenzo Giovannini, DICAM, University of Trento
Prof. Dino Zardi, DICAM, University of Trento

Reviewers
Prof. Christophe Brun, LEGI, Université Grenoble Alpes
Prof. Joan Cuxart, University of the Balearic Islands

Examination Committee
Prof. Simona Bordoni, DICAM, University of Trento
Prof. Christophe Brun, LEGI, Université Grenoble Alpes
Dr. Manuela Lehner, ACINN, Universität Innsbruck

Credits of the cover image:
Howland, C. J., Taylor, J. R. and Caulfield C.P., 2020. Published by Cambridge University Press

University of Trento
Doctoral School in Civil, Environmental and Mechanical Engineering
http://web.unitn.it/en/dricam
Via Mesiano 77, I-38123 Trento
Tel. +39 0461 282670 / 2611 - *dicamphd@unitn.it*

À Amour,
pour son soutien
de tous les jours

Contents

Chapter 1

Introduction

This thesis investigates atmospheric turbulence in the Planetary Boundary Layer (PBL), with a specific focus on strongly stratified conditions, which may occur over glaciers or during nights with strong radiative cooling at the surface. This introduction provides a conceptual basis for the research work. The first section introduces some theoretical concepts about turbulence in neutral conditions, which motivated part of this work (Section 1.1). In the following section, an overview of turbulence in the Stable Boundary Layer (SBL) is presented by investigating the concept of critical Richardson number, which is commonly used as a control parameter in turbulence parameterizations (Section 1.2). Section 1.3, instead, focuses on current issues in turbulence parameterizations over complex terrain, and how the same tool of analysis may help improving our understanding of turbulence over complex terrain and in SBL flows. In Section 1.3.2 a description of boundary-layer flows, such as low-level jets, which may affect turbulence structure over complex terrain and in SBL conditions is presented. The reader will then find a summary of the thesis in Section 1.4.

The introduction is intentionally concise, and avoids repeating equations, concepts or definitions which most of the readers are likely familiar with, to help them focusing on the state-of-the-art issues that motivated this work. The reader will then find more details in the next two chapters.

1.1 General background on turbulence in neutral condition

Turbulence is usually defined as a state of the fluid flow characterized by swirling motion. Such motions are observed in a variety of phenomena, covering a wide range of scales, from centimeter tap water vortexes to 10^2 km size hurricanes or 10^4 km light years galaxies (Dubrulle, 2019). The dynamics of turbulent flows is governed by the Navier-Stokes equations, where the quadratic nonlinear advection term is responsible for interactions among different length scales. Energy is transferred from one scale to the other through inertial processes, and is eventually dissipated into heat at the smallest scales by viscous processes.

The standard phenomenological description of turbulence is that of a cascade process

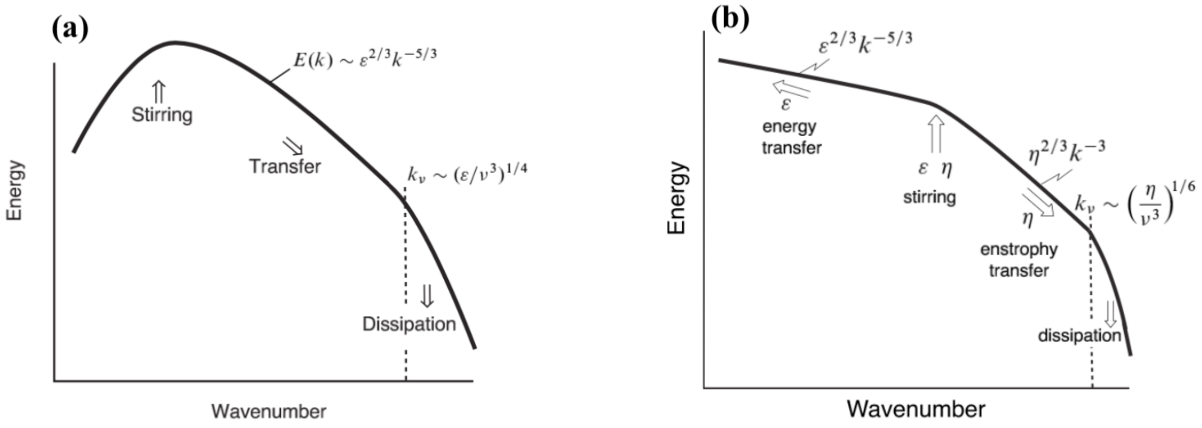

Figure 1.1: Energy cascade process in three- and two-dimensional flows, panel (a) and (b) respectively. Adapted from Vallis (2005), Figure 8.3 and 8.7.

[1]. The latter presents a substantial difference in two- and three-dimensional flows: while turbulent motions in two-dimensional flows transfer on average energy from the small to the large scales, the opposite occurs in three-dimensional flows (Boffetta and Ecke, 2011). Figure 1.1 compares the different characteristics of the energy spectrum in the two cases, and the cascades are respectively called *direct* (Figure 1.1a) and *inverse* (Figure 1.1b) energy cascade. The dynamical mechanism explaining the dramatic enhancement of dissipation in three-dimensional turbulence is the vortex stretching, as hypothesized by Taylor (Taylor, 1938) and resumed by Onsager (Onsager, 1949). This mechanism vanishes in two-dimensional flow, thus affecting the turbulent cascade process (Vallis, 2005, Pag. 368).

Vorticity is defined as the curl of the velocity field, $\omega = \nabla \times \vec{u}$, and its transport equation can be determined by taking the curl of the incompressible Navier-Stokes equations (with conservative forces) and using a few vector calculus identities[2][3]:

$$\frac{D\vec{\omega}}{Dt} = \frac{\partial \vec{\omega}}{\partial t} + (\vec{v} \cdot \nabla)\vec{\omega} = (\vec{\omega} \cdot \nabla)\vec{v} + \nu \nabla^2 \vec{\omega} \tag{1.1}$$

When $\frac{D\vec{\omega}}{Dt} = 0$, the vortex-stretching term, $(\vec{\omega} \cdot \nabla)\vec{v}$, is equal to -$\nu\nabla^2\vec{\omega}$. From an order of magnitude analysis, this balance occurs when $\frac{\omega u}{l} = \frac{\nu\omega}{l^2}$, where ω, u and l are the vorticity, velocity and size of turbulent motion, respectively. By using the definition of the Reynolds number, $Re = \frac{UL}{\nu}$, with U and L typical velocity and length scales of the flow, the balance occurs when $Re = 1$ (Chen, 2013). This corresponds to the common definition of the Kolmogorov scale η, which is the scale at which the local Reynolds number is of order one and kinetic energy is dissipated into heat by viscous processes. This is a very small scale for geophysical flows, of the order of millimeters or

---

[1] Historically the first use of the word *cascade* in the theory of turbulence seems to be in a letter sent by Lars Onsager to Chia-Chiao Lin in June 1945 (Eyink and Sreenivasan, 2006)

[2] $(\vec{u} \cdot \nabla)\vec{u} = \nabla\left(\frac{|\vec{u}|^2}{2}\right) - \vec{u} \times \vec{\omega}$ $\qquad \nabla^2\vec{u} = \nabla(\nabla \cdot \vec{u}) - \nabla \times (\nabla \times \vec{u}) = -\nabla \times (\nabla \times \vec{u})$

[3] $\nabla \times (\vec{u} \times \vec{\omega}) = (\vec{\omega} \cdot \nabla)\vec{u} - \vec{\omega}(\nabla \cdot \vec{u}) - (\vec{u} \cdot \nabla)\vec{\omega} + \vec{u}(\nabla \cdot \vec{\omega}) = (\vec{\omega} \cdot \nabla)\vec{u} - (\vec{u} \cdot \nabla)\vec{\omega}$

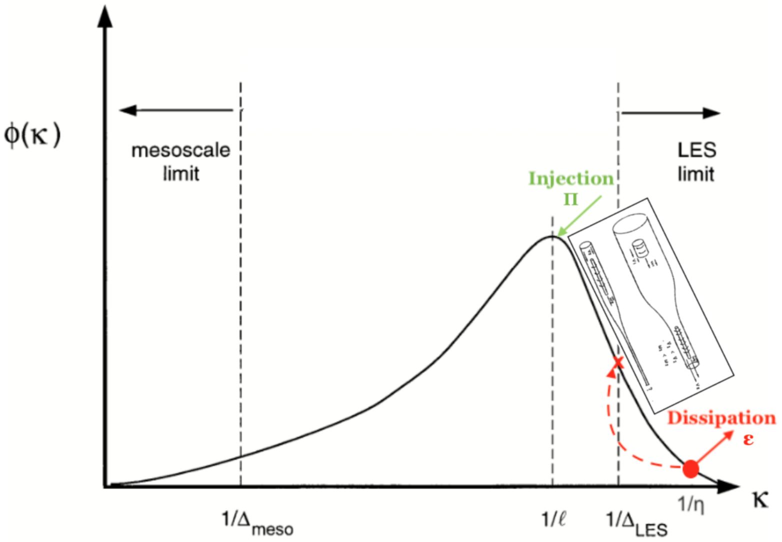

Figure 1.2: Schematic view of how weather and climate models include the energy cascade process of three-dimensional turbulent flows. The nonlinear dynamics evolves up to the grid scale of the model, then it is parameterized in terms of mean quantities with loss of possible bifurcations in the dynamics.

less, and such small scales can be generated at the boundaries or in the fluid interior. For example, in the former case, viscosity must become important to bring wind velocity to zero at the surface in order to satisfy the no-slip condition. In the latter case, such small scales are triggered by a primary dynamical instability of the flow, which will grow in amplitude and eventually the perturbation itself will become unstable to smaller perturbations. Thus, smaller perturbations will feed off its energy and grow, eventually becoming unstable, and so on, down to turbulent motions sufficiently small to feel the effects of viscosity (Vallis, 2005, Pag. 360).

The foundation of many theories of three-dimensional turbulence is the spectral theory of Kolmogorov for neutrally stratified flows, well documented in its trilogy of papers (Kolmogorov, 1941b,c,a). In the Kolmogorov picture, for high Reynolds flows with a large scale separation between the forcing scale l, and the dissipation scale η, there exists an intermediate range of scales where neither forcing nor dissipation are explicitly important to the dynamics. The nonlinear transfer of energy is assumed sufficiently local (in spectral space) in the so-called *inertial range*, and thus the rate Π at which kinetic energy is transferred inertially to smaller scales depends only on processes occurring at or near that scale. That is to say, the energy spectrum is a function only of Π and the wavenumber itself k, and there is no functional dependence on the forcing or dissipation scale. By further assuming that Π is independent of the wavenumber, and is constant throughout the inertial range extending down to the Kolmogorov scale, Π will be equal to the energy dissipation rate ϵ. Thus, no mechanism other than viscosity operates to remove kinetic energy from the turbulent hierarchy. These are the main physical assumptions to derive the $-5/3$ slope of the energy spectra of three-dimensional turbulence (Vallis, 2005, Section 8.2.2).

The assumption of a constant energy flux, also known as *non-intermittency* assumption, demands that rare events (in time or space) with large amplitudes do not dominate the energy flux or the dissipation rate. This was soon objected by Landau, who recognized that the fluctuations of the energy dissipation field matter (Frisch, 1995, Section 6.4), and led Obukhov and Kolmogorov to refine their previous results and formulate the *log-normal* model of turbulence (Oboukhov, 1962; Kolmogorov, 1962).

In Numerical Weather Prediction (NWP) models, most parameterizations of turbulence in the PBL follow the original theory of Kolmogorov for the expression of the energy dissipation rate, both in Reynolds-Averaged Navier-Stokes models (RANS) and in Large Eddy Simulations (LES). Figure 1.2 shows, schematically, how models deal with the energy cascade process, under the assumptions of the Kolmogorov theory. Dissipation is forced to occur at the grid size of the model, and, by doing so, any fluctuation in the energy dissipation rate is lost, as well as any dynamical bifurcation towards different regimes, which may occur during the cascade process. To overcome this limit, a current research approach is to introduce stochastic models for sub-grid scale turbulence (Berner et al., 2017).

1.2 Turbulence in stably stratified flows: The Richardson number

During the Medal Lecture at the 2015 General Assembly of the European Geosciences Union, Prof. Sergej S. Zilitinkevich introduced his work by claming that:

> *"99% of the atmosphere typically has Richardson number higher than* 100*. Nothing to do with the* 0.25 *critical number and at the same time the bulk of the atmosphere is always turbulent. This is puzzling and until recently we had no physical explanation for that."*

Also, during a lecture at the University of Trento (May 30, 2019, "Energy and Flux Budget Turbulence Closure Theory for Stably Stratified Flows) he pointed out that:

> *"Turbulence can be killed by Reynolds number, Richardson number can only reduce the size of eddies."*

At the beginning of this work on turbulence in stably stratified flows, those two sentences motivated me to review the concept of Richardson number, and how the 0.25 critical value is derived, in order to better understand why its application to turbulence modeling presents limitations, while still being broadly used.

1.2.1 Definition and different interpretations

Different definitions of the Richardson number exist in the literature, such as the *gradient*, *bulk* and *flux* Richardson number (Stull, 1988, Section 5.6). Here, we focus on the gradient Richardson number, Ri, which is a property of the mean flow and is commonly identified as a measure of the static stability of the atmosphere. It is a control parameter for the dynamics, as it controls the onset of a primary dynamical instability in a laminar flow, which eventually would lead to a turbulent flow (in this perspective, turbulence is considered as the results of a series, or *cascade*, of dynamical instabilities Manneville, 2010, Pag. 10). In a reference system aligned with the mean wind speed, the gradient Richardson number is defined as:

$$Ri = g\frac{dln\overline{\theta}(z)}{dz} / \left(\frac{d\overline{u}}{dz}\right)^2 = \frac{df}{dz} / \left(\frac{d\overline{u}}{dz}\right)^2 = \frac{N^2}{S^2} \tag{1.2}$$

and includes df, the buoyancy force per unit mass across a layer of thickness dz, and the variation of the horizontal mean velocity field along the vertical. These two quantities are related to two fundamental frequencies (and time-scales): that of the vertical shear S and the Brunt-Väisälä frequency N. The shear frequency characterizes the dynamical processes, and the Brunt-Väisälä frequency the stability (and gravity waves)(Schertzer and Lovejoy, 1985, Pag. 12-13). The dominant process has the highest frequency (smallest time scale): when Ri is small, the mechanical shear has time to wipe out vertical inhomogeneities in dz (fast mixing), whereas when it is large, the mechanical process is too slow compared to the time-scale of the restoring buoyancy force.

It is enlightening to analyze the Richardson number also as squared ratio of two length scales, a definition more common in the Geophysical Fluid Dynamics community. This type of expression shows how a parameter describing the vertical structure of the atmosphere may imply a horizontal scale (Navarra, 2019). By scaling Eq. 1.2 with a characteristic layer depth H, a typical horizontal velocity U and introducing a typical frequency f, Ri may be expressed as:

$$Ri = \frac{N^2H^2}{U^2} = \left(\frac{HN}{f}\right)^2 \left(\frac{f}{U}\right)^2 = \left(\frac{L_1}{L_2}\right)^2 \tag{1.3}$$

In large-scale dynamics, a typical frequency of the flow would be the Coriolis parameter, thus the Richardson number would be the ratio between the Rossby deformation radius and the typical horizontal length scale of the flow.

The interpretation of the Richardson number in terms of typical scales of the flow goes back to Batchelor (1953), who pointed out that there is a:

> *"Common misconception that the Richardson number has significance as a local quantity. It is a reference parameter for a whole flow field, just as is the Reynolds number. (...) It is not possible in general to regard the point-to-point variation of a Reynolds number in any given flow field as having any precise meaning."*

Motivated by these thoughts, he demonstrated the role played by the Richardson number in ensuring dynamical similarity of different motions of an atmosphere with variable density, under certain restrictions. This means that, it is possible to match the velocity distributions of two different flows, belonging to the class of motions under consideration, by an appropriate change of scales. Following the definition of Richardson number provided by Batchelor (1953), Bolgiano (1959) then found a correspondence between Ri and the size of an eddy (Eq. 13 of his paper).

As we will show in the following section, another physical interpretation of Ri is related to potential and kinetic energies, with the numerator being the potential energy barrier that mixing must overcome in order to occur, and the denominator being the kinetic energy that the shear flow can supply when smoothed away. This highlights again the coupling between horizontal and vertical motions, with kinetic energy in the horizontal field used to mix air vertically.

1.2.2 The critical Richardson number

The concept of the Richardson number as an important dimensionless parameter for the dynamics of stably stratified flows naturally comes out from linear hydrodynamic stability analysis of a laminar flow. Following Cushman-Roisin and Beckers (2009, Section 14.2), let us consider a two-dimensional (x, z) stratified shear flow in an inviscid, non-heat-conducting, incompressible fluid of density $\rho_0(z)$.

$$\begin{aligned}
\frac{\partial u}{\partial t} + u\frac{\partial u}{\partial x} + w\frac{\partial u}{\partial z} &= -\frac{1}{\rho_0}\frac{\partial p}{\partial x} \\
\frac{\partial w}{\partial t} + u\frac{\partial w}{\partial x} + w\frac{\partial w}{\partial z} &= -\frac{1}{\rho_0}\frac{\partial p}{\partial z} - \frac{\rho g}{\rho_0} \\
\frac{\partial u}{\partial x} + \frac{\partial w}{\partial z} &= 0 \\
\frac{\partial \rho}{\partial t} + u\frac{\partial \rho}{\partial x} + w\frac{\partial \rho}{\partial z} &= 0
\end{aligned} \tag{1.4}$$

Linear stability analysis studies the evolution of infinitesimal fluctuations, superimposed on a basic flow, which is solution of the governing equations. Stationary basic flows are commonly used, as time-dependent basic flows greatly complicate the analysis (Majda and Shefter, 1998). Our basic state and infinitesimal perturbations are the following:

Basic state	**Perturbations**
$u = \overline{u}(z), \quad w = 0$	$u'(x,z,t), \quad w'(x,z,t) \quad u', w' \ll u$
$\rho = \overline{\rho}(z)$	$\rho'(x,z,t), p'(x,z,t) \quad \rho' \ll \rho$

By linearizing the governing equations (Eqs. 1.4) around the basic state, we get a set of equations describing the evolution of the perturbation field:

$$\begin{aligned}
\frac{\partial u'}{\partial t} + \overline{u}\frac{\partial u'}{\partial x} + w'\frac{d\overline{u}}{dz} &= -\frac{1}{\rho_0}\frac{\partial p'}{\partial x} \\
\frac{\partial w'}{\partial t} + \overline{u}\frac{\partial w'}{\partial x} &= -\frac{1}{\rho_0}\frac{\partial p'}{\partial z} - \frac{\rho' g}{\rho_0} \\
\frac{\partial u'}{\partial x} + \frac{\partial w'}{\partial z} &= 0 \\
\frac{\partial \rho'}{\partial t} + \overline{u}\frac{\partial \rho'}{\partial x} + w'\frac{d\overline{\rho}}{dz} &= 0
\end{aligned} \tag{1.5}$$

In order to have a single prognostic equation to describe the perturbation, it is convenient to work with vorticity and introduce the perturbation streamfunction, ψ':

$$u' = \frac{\partial \psi'}{\partial z}, \quad w' = -\frac{\partial \psi'}{\partial x} \tag{1.6}$$

$$\zeta' = \left(\frac{\partial u'}{\partial z} - \frac{\partial w'}{\partial x} \right) \tag{1.7}$$

$$\frac{\partial}{\partial z}(Eq.1.5.a) - \frac{\partial}{\partial x}(Eq.1.5.b) = \frac{\partial \zeta'}{\partial t} \tag{1.8}$$

This leads to an equation for ψ' with wavelike solutions, such as plane waves $\psi'(x,z,t) = \phi(z)e^{ik(x-ct)} = \phi(z)e^{ikx}e^{-ikt(c_{Re}+ic_{Im})}$. The imaginary part, c_{Im}, of the phase velocity is the important variable in linear stability analysis. If c_{Im} is positive, the amplitude of the disturbance increases exponentially with time, the perturbation grows and the flow is unstable. If c_{Im} is negative, the amplitude of the disturbance decreases exponentially with time, and the flow is stable.
By replacing ψ' with a plane wave solution, we obtain:

$$(\overline{u} - c)\left(-k^2 + \frac{d^2}{dz^2}\right)\phi(z) + \left(\frac{N^2}{\overline{u} - c} - \frac{d^2\overline{u}}{dz^2}\right)\phi(z) = 0 \tag{1.9}$$

where N^2 is the Brunt-Väisälä frequency defined in Eq. 1.2. Eq. 1.9 is the *Taylor-Goldstein* (T-G) equation and governs the vertical structure of a wavelike perturbation in a stratified parallel shear flow. Its solutions exhibit singularity at critical levels (where the speed of the mean flow $\overline{u}(z)$ matches the phase velocity c). By applying the following boundary conditions to the flow:

$$\phi(0) = 0, \quad \phi(H) = 0$$

it is not possible to solve the eigenvalue problem in the general case of an arbitrary shear flow $\overline{u}(z)$. However, the method of deriving integral constraints allows to predict certain aspects of instability without solving the T-G equation. We can choose $\phi(z) = \sqrt{(\overline{u}(z) - c)}f(z)$ and replace that into Eq. 1.9, which then multiplied by the complex conjugate $f*$ and integrated over the domain of interest, according to boundary conditions, leads to:

$$\int_0^H \left[N^2 - \frac{1}{4}\left(\frac{d\overline{u}}{dz}\right)^2\right]\left(\frac{|f|^2}{|\overline{u} - c|^2}\right)dz = \int_0^H (\overline{u}(z) - c)\left(\frac{df}{dz}^2 + k^2|f|^2\right)dz \tag{1.10}$$

An integral constraint for the T-G equation is then found by taking the imaginary part of Eq. 1.10, with the red brackets identifying positive quantities:

$$c_{Im}\int_0^H \left[N^2 - \frac{1}{4}\left(\frac{d\overline{u}}{dz}\right)^2\right]\left(\frac{|f|^2}{|\overline{u} - c|^2}\right)dz = -c_{Im}\int_0^H \left(\frac{df}{dz}^2 + k^2|f|^2\right)dz \tag{1.11}$$

Thus the equality is satisfied with the following conditions:

$$\begin{aligned} &\left[N^2 - \frac{1}{4}\left(\frac{d\overline{u}}{dz}\right)^2\right] > 0 \quad \rightarrow c_{Im} = 0 \\ &\left[N^2 - \frac{1}{4}\left(\frac{d\overline{u}}{dz}\right)^2\right] < 0 \quad \rightarrow c_{Im} > 0 \quad \text{or} \quad c_{Im} < 0 \end{aligned} \tag{1.12}$$

The first is a sufficient condition for the linear stability of the basic flow with respect to the chosen perturbation, while the second does not provide any information on stability because both growing and decaying perturbations are allowed. The first condition corresponds to $Ri > 0.25$. It is worth noting that, although it is possible to discover sufficient conditions for stability by means of general integral methods, these lead only to necessary conditions for instability. If a flow field satisfies these necessary conditions, detailed calculations are still required to verify that the flow is actually unstable (Pedlosky, 1987, Pag. 508).

The same critical value for the Richardson number may be derived using simple energy considerations (Markowski and Richardson, 2010, Chapter 3). A fluid parcel in a stratified flow is pulled back by gravity force to its equilibrium level when it rises or sinks adiabatically. These vertical oscillations are the simplest mechanism for the generation of internal gravity waves. Despite the restoring force, the existence of vertical shear in the flow where the parcel moves, makes energy available for the perturbation. It may be possible that kinetic energy in the horizontal wind is used to mix air vertically. Consider two air parcels with unit mass at heights z_0 and $z_0 + \Delta z$ respectively, in a horizontal airflow with potential temperature and wind speed increasing linearly with height, as shown in Figure 1.3. The interchange of those two parcels requires work against gravity, because the atmosphere is stably stratified. The total work per unit mass to rise adiabatically one parcel up and the other down is $\delta W = 2\delta w = 2\left(g\frac{\Delta\theta}{2\theta}\Delta z\right)$. The energy for this work can be supplied by the kinetic energy per unit mass available in the flow, which is evaluated as the difference between the final and initial kinetic energy of the flow. Let us assume that the interchange of the two air parcels is done by a perturbation whose effect is to equalize momentum in the layer. The final velocity for both air parcels would then be the mean velocity over the layer, $u = \frac{u_0 + (u_0 + \Delta u)}{2}$, and $\Delta KE = \frac{1}{2}\left(u_0^2 + (u_0 + \Delta u)^2 - 2(\frac{u_0 + (u_0 + \Delta u)}{2})^2\right) = \frac{1}{4}(\Delta u)^2$. In order for the interchange to occur, the amount of kinetic energy available has to be larger than the work required for the interchange, thus:

$$\frac{1}{4}(\Delta u)^2 > g\frac{\Delta\theta}{\theta}\Delta z$$

$$\frac{1}{4} > \frac{g\frac{\Delta\theta}{\theta}\Delta z}{(\Delta u)^2} = \frac{\frac{g}{\theta}\frac{d\theta}{dz}(\Delta z)^2}{(\Delta z)^2\left(\frac{du}{dz}\right)^2} = Ri \tag{1.13}$$

that is the Richardson criterion for instability with $Ri_{cr} = 0.25$.

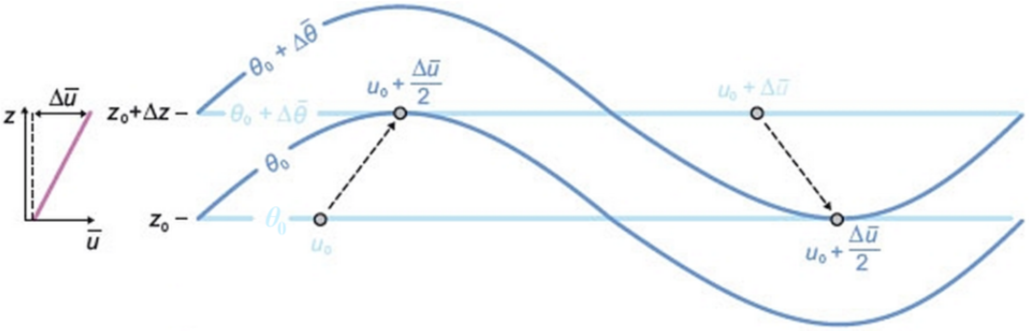

Figure 1.3: Schematic atmospheric layer for a simple physical diagnosis of instability in a stratified shear flow. The critical Richardson number $Ri_{cr} = 0.25$ is derived from energy considerations. Potential temperature surfaces are perturbed in a wavelike manner, with light (dark) blue surfaces before (after) the perturbation. Adapted from Markowski and Richardson (2010), their Figure 3.21.

1.2.3 How critical is the critical Richardson number?

So far, we have shown that the Richardson criterion is a sufficient condition for the stability of a stratified, parallel shear flow with respect to infinitesimal perturbations. Stable Boundary Layer (SBL) flows with large Richardson number are characterized by many non-stationary submeso motions, such as wave-like modes, microfronts, solitary modes, meandering motions, drainage flows. Those motions may have large amplitudes and trigger shear-instabilities with the subsequent development of turbulence, as the Richardson criterion is no valid for finite perturbations (Zilitinkevich et al., 2008). The important generation of turbulence by the submeso shear is poorly understood, since the dynamics of the submeso motions varies significantly between sites, depending on topography and vegetation, and vary between nights at a given site (Mahrt, 2010). Submeso motions can also transport instabilities generated in regions with $Ri < Ri_{cr}$ to regions with larger Ri. Moreover, large Richardson numbers often occur with low wind speed, thus even perturbations with small amplitude might not be considered anymore infinitesimal with respect to the basic flow. Also, the basic flow previously considered to derive $Ri_{cr} = 0.25$ was stationary, which is generally not the case for SBL flows with high Reynolds numbers. Last but not least, horizontal layering of strongly stratified flows is observed in numerical (Godeferd and Staquet, 2003) as well as laboratory studies (Billant and Chomaz, 2000), with typical vertical length scale of order U/N. The organization of the flow into quasi-horizontal vertically decorrelated vortex structures further complicates the use of the Richardson number. In fact, the spatial vortex structure is close to a thin pancake shape and it is expected that horizontal shear starts to play a role, leading to enhanced horizontal mixing. Galperin et al. (2007) (their Figure 2) have shown that for strong stratification two effects become noticeable. While the vertical eddy viscosity and heat diffusivity are reduced compared to their values in the neutral case, their horizontal counterparts are enhanced. There is also a significant difference between the vertical heat diffusivity and vertical viscosity, with the former becoming vanishingly small and approaching its molecular value, and the latter remain-ing finite even on the largest scales strongly dominated by stratification. None of these mechanisms is considered in the derivation of Ri_{cr} or included in the definition of Ri. All that supports the observation of turbulence at any stratification, regardless of the sufficient condition for stability related to the Richardson number.

However, many attempts have been made in the last decades to find a critical threshold for turbulence development in SBL flows. Many of those efforts aimed at improving predictions of boundary-layer height, h, by means of both observational and modelling studies. In fact, it is commonly assumed that h is located where the Richardson number $Ri(z)$ exceeds a critical threshold, with $Ri(z)$ computed over the entire layer from the surface up to z (bulk Richardson number). Many of those studies were based on the idea that Ri_{cr} should not be universal, but dependent on some physical variables. For example, recently, Richardson et al. (2013), based on LES database and wind-tunnel data, proposed a stability-dependent relationship of Ri_{cr}, increasing with increasing h/L, where L is the Obukhov length. The validity of that result was re-examined and confirmed by Basu et al. (2014) using a different set of observational data. A similar dependence was previously found by Nieuwstandt (1985) in his analytical model for the stationary SBL. Zilitinkevich and Baklanov (2002) suggested that Ri_{cr} should increase with increasing surface roughness length (confirmed by Jeričević and Grisogono, 2006 over urban areas), as higher turbulent mixing is expected in SBLs with equal wind speed and thermal stratification, but larger roughness length. They also recommended to include the Brunt-Väisälä frequency of the free atmosphere immediately above the SBL in the definition of Ri_{cr}.

Limits in the concept of a critical Richardson number lead researchers to impose ad-hoc Ri-dependencies of the turbulent Prandtl number in modern turbulence closures, preventing the appearance of Ri_{cr}, or non-zero background diffusivities (as the YSU PBL scheme in the WRF model), in order to guarantee turbulence mixing at large Ri. Those limits also motivated research towards turbulence closure models which naturally avoid the long-standing issue of a finite Ri_{cr}, without requiring any artificial tricks. Recently, Cheng et al. (2020) developed a second-order closure (SOC) turbulence model, including new horizontal and vertical heat flux equations with respect to common closures (Mellor, 1982 level 2.5 or Galperin et al., 1988). They traced the origin of a finite Ri_{cr} to the presence of vertical momentum fluxes in the budget equations for horizontal heat fluxes, and modified that with a new closure for the return-to-isotropy of the pressure-temperature correlation term (Canuto et al., 2008). This led Ri_{cr} to extend to infinity. Model results, compared with available observational, experimental, and high-resolution numerical data, showed significant improvements in the representation of the SBL. Previously, Zilitinkevich et al. (2007) proposed a SOC model based on budget equations for key turbulent fluxes (turbulent kinetic and potential energies, vertical turbulent fluxes of momentum and buoyancy), which also allows the existence of turbulence driven by shear at any Richardson number. Few months later, Canuto et al. (2008) proposed a different SOC, based on a larger set of budget equations for second-moments with respect to Zilitinkevich et al. (2007), and without parameterizing the horizontal heat fluxes as part of the "effective dissipation rate" of vertical momentum fluxes. All those models suggest the existence of a transitional range of Ri, which separates a regime of very high efficiency of momentum and heat transfer ($Ri < 0.1$) from one of much larger efficiency of momentum transfer than heat transfer. The latter can be explained by a dominant contribution of internal gravity waves (IGW) (Zilitinkevich et al., 2008), which efficiently transport momentum but sustain only little (or in the linear approximation, no Nappo, 2002) heat fluxes (Monti et al., 2002).

The dual nature of fluctuations in stably stratified flows, representing both turbulence and waves, complicates the design of closures for variances and covariances of fluctuations. All previous models were compared to the same data sets, which included wave-driven data for large Richardson number (Cheng et al., 2020), characterised by larger scatter in vertical momentum diffusion than in heat diffusion. Models were unable to reproduce this scatter because they did not account for the vertical transport of momentum due to IGW, but this contribution should be included for a more complete picture. Zilitinkevich et al. (2009) did include this contribution in a revised version of their model, together with turbulence generated by the waves, and the model explained the IGW mechanism leading to counter-gradient heat fluxes at high Richardson number, as well as the weakening of the boundary-layer turbulence by trapped IGW.

1.3 Boundary-layer approximation: turbulence over complex terrain

Turbulence closures used in NWP models are mostly developed in the framework of the *boundary-layer approximation* (Trini et al., 2001). Some of the closures described in the previous section included equations for turbulent stresses and fluxes, solved by neglecting terms including horizontal derivatives and subsidence. Those types of closure are often called "1D PBL schemes". Although frequently applied, those assumptions are rarely valid in the atmosphere (Stull, 1988). For example, in strongly stably stratified conditions, once the horizontal layering of the flow develops, the horizontal shear may become important to describe turbulence (Galperin et al., 2007). In NWP models generally the horizontal diffusion, when included, is handled in a separate way from the vertical diffusion, and is actually introduced more for numerical stability reasons than physical ones. When the horizontal grid cell spacing is relatively coarse (on the order of 10 km), horizontal gradients in momentum, heat, and scalar quantities are relatively small compared to vertical gradients of the same quantities (Kosović et al., 2020). In these situations, turbulence is fully parameterized, and the traditional approach of neglecting the horizontal gradients of mean quantities and applying a 1D (vertical) turbulence closure model to handle the vertical turbulent mixing is convenient and appropriate (Juliano et al., 2021). With the enhancement of computational power, leading NWP models towards high-resolution mesoscale simulations ($\Delta x \sim$100 m - 1000 m), able to resolve surface heterogeneities and topographic details, there is a need to develop closures which relax, at least partially, the assumptions of the boundary-layer approximation. Such treatment is not valid as the grid cell spacing approaches what is known as the "gray zone" or "terra incognita" (Wyngaard 2004), especially in regions of complex terrain.

Wyngaard (2004), by means of measurements in the unstable atmospheric surface layer from the Horizontal Array Turbulence Study (HATS), suggested that a first-order closure with a second-order tensor for eddy diffusivity (instead of a scalar) would be the simplest reasonable model for reproducing turbulent fluxes in the gray zone. In convective boundary-layers, Honnert and Masson (2014) found, by means of idealised simulations, a critical horizontal resolution, close to half the PBL height, for which horizontal-shear production of turbulence should be accounted for. Goger et al. (2018) evaluated the performance of turbulence closures in mesoscale simulations over an Alpine valley, with and without horizontal-shear production (still included with a LES approach), during days when a thermally-driven circulation was present. When introducing a length scale for the horizontal-shear contribution, dependent on physical processes which vary in time and space instead of the constant value depending on the grid resolution assumed in LES, the model better reproduced the up-valley wind phase (Goger et al., 2019). The closest attempt towards a three-dimensional closure was done by Kosović et al. (2020) for convective boundary layers, following the level 2.5 model of Mellor and Yamada (Mellor, 1982). They accounted for both vertical and horizontal turbulent mixing within an energetically consistent framework, which requires applying the same closure assumptions when computing the turbulent stresses and fluxes. Horizontal derivatives in the diagnostic equations of turbulent stresses and fluxes, and in the prognostic equation of turbulent kinetic energy are included, and the system of linear algebraic equations at each model grid cell solved where the Richardson number is below a critical threshold. Details about the model implementation can be found in Juliano et al. (2021).

While those 3D closures are up to now more oriented towards a better representation of convective situations in high-resolution mesoscale simulations, it seems, for the reasons introduced in the previous section, that the representation of stably stratified flows would also benefit from the development of this type of closures.

1.3.1 Anisotropy of turbulent motions

For near-surface turbulence, a general approach that seems promising in both convective and stable conditions for improving our understanding of turbulence, as well as its representation in models, is the investigation of the departure of the Reynolds stress tensor from the isotropic form. It is worth stressing here that this is only one aspect of the anisotropy of turbulence, which can exhibit anisotropy that is dynamically significant and not captured in the Reynolds stresses (Kassinos et al., 2001). Turbulence anisotropy can be characterised in many different ways, such as: anisotropy of structures in physical space (Sagaut and Cambon, 2018, Figure 10.5), anisotropy of kinetic energy spectra (Lang and Waite, 2019, Figure 8), anisotropy of the viscous dissipation tensor (Pope, 2000, Figure 7.39), anisotropy of transport properties (Galperin et al., 2007, Figure 2). In certain cases, counterintuitive results can only be explained in terms of a combined description of different one-point statistics tensors (Kassinos et al., 2001).

Analysing the anisotropy of the Reynolds stress tensor, Stiperski and Calaf (2018) found that during daytime shear-generated near-surface turbulence is very anisotropic and thus governed by multiple length scales. Large scatter for stably stratified flows may also be understood in terms of turbulence anisotropy, characterised by motions dominantly in the horizontal plane of the streamwise coordinate system, and by large non-local contributions. Breakdown of traditional similarity relationships in the surface-layer in complex conditions thus relates to the presence of strong anisotropic turbulence, which cannot be described as usual by a single characteristic length scale, the local Obukhov length scale L. There are relevant processes within the surface layer that cannot be described by L, but information about them may be encoded in turbulence anisotropy, even if this parameter is calculated locally (Stiperski et al., 2021). How to unequivocally connect anisotropy to large-scale governing parameters, which would allow predicting the type of anisotropy that occurs in a set of given conditions, however, remains an open question.

In the Boussinesq model[4], the anisotropic Reynolds stress tensor is considered aligned with the mean strain tensor, and the proportionality constant is the eddy viscosity. This is the simplest way to parameterize turbulence and is common to all closures up to order 1.5 (the ones commonly implemented in large-scale atmospheric numerical models Shin and Hong, 2011), each one having its own way to model eddy viscosity. The latter is generally considered equal along the horizontal and vertical direction, and function of a single length scale. Investigating the properties of the anisotropic Reynolds stress tensor, according to different characteristics of the mean flow, thus may give insights on how to differentiate the horizontal and vertical viscosities, and provide the simplest way to include three-dimensional effects in turbulence parameterizations. While this is beyond the scope of this work, this was the reason that motivated me to span from numerical simulations of the SBL over complex terrain to the analysis of turbulence anisotropy from measurements collected over a glacier. However, it should be said that when the horizontal and vertical eddy viscosity coefficients are not equal, the analogy between turbulence and molecular friction is more difficult (Pedlosky, 1987, Pag. 184).

1.3.2 Nighttime circulation and influence on turbulence structure

The boundary layer approximation assumes that turbulent transport exceeds that associated with the mean flow, especially in the vertical direction (Rotach et al., 2015), and that horizontal advection can be neglected. Over spatially heterogeneous landforms or land cover, the transport in the PBL is also affected by baroclinicity due to differential heating or cooling, which leads to local wind systems, such as slope and valley winds in mountainous areas. Together with turbulent mixing, these flows control exchange processes in the PBL, enhancing the transport in the horizontal direction and favouring the departure of the turbulence features from those reported over flat terrain regions. Indeed, over mountains thermally driven circulations can cause non-negligible horizontal shear, which contributes to turbulence production (Lehner and Rotach, 2018; Goger et al., 2019), and strong horizontal gradients are commonly observed, for instance in

---

[4] It is surprising to note that the publication usually cited for the introduction of the concept of Reynolds averages is Reynolds (1895), while the publication cited for the introduction of the Boussinesq model for the Reynolds stresses is Boussinesq (1877), thus much earlier! Boussinesq indeed implicitly introduced the Reynolds stress tensor, as explained by Schmitt (2007).

connection with diurnal flow along curved valleys, mountain venting above mountain tops, or nocturnal valley-exit jets (Serafin et al., 2018).

The latter are a specific type of Low Level Jet (LLJ), which is broadly defined as a narrow current with characteristic scales from the regional to the mesoscale, and corresponding to a maximum in the wind-speed profile in the boundary-layer (Haikin and Castelli, 2022). LLJs may have different origins (Banta et al., 1996, 2007; Chrust et al., 2013; Tuononen et al., 2017; Nikolic et al., 2019; Svensson et al., 2019), as summarised in Stensrud (1996), and in complex terrain they have been documented at canyon (Banta and Gannon, 1995; Chrust et al., 2013; Muoz et al., 2020) or valley exits (Pamperin and Stilke, 1985; Drobinski et al., 2006; Spengler et al., 2009; Sasaki et al., 2010; Hellström et al., 2017; Jiménez et al., 2019), where topography abruptly changes opening onto a basin or a plain. In this case, LLJs are a local modification of down-valley flows, and occur during nights of weak synoptic forcing and clear skies as thermally-driven winds or during nights of strong synoptic forcing as dynamically-driven winds, with channeling from aloft of synoptic flows nearly aligned with the valley axis. The initiation, maintenance and dissipation of the jet, and thus its duration, are closely tied to the times of sunset and sunrise, with maximum speed usually attained close to sunrise. However, the mechanism responsible for the flow acceleration near the exit is not always well understood. In some cases, hydraulic theory and transition of the flow from subcritical to supercritical state may explain the basic dynamics: a deep layer of cold air drains out of the canyon/valley, sinks and compresses, accelerating downward into a shallower layer forming the jet, with the increase of wind speed caused by the conversion of potential into kinetic energy (Chrust et al., 2013). Surface friction at the sidewalls also contributes to the structure of the jet. On the one hand, the release from the frictional effects at the valley exit may contribute to the acceleration of the down-valley flow (Banta and Gannon, 1995). On the other hand, friction at the sidewalls may generate potential vorticity, which is conserved in adiabatic and frictionless conditions and thus influences the tendency of the flow to maintain its shape beyond the exit region, where the effect of the sidewalls is no more present and stable atmospheric stratification inhibits friction-induced dissipation of potential vorticity by surface turbulence (Zängl, 2004). In valleys with a narrow pass at their exit, a Bernoulli mechanism under the assumption of a steady, frictionless and irrotational fluid may be a simple model for the increase of the down-valley wind speed at the exit (Whiteman, 2000; Arduini et al., 2016; Jiménez et al., 2019), associated with the convergence of airstreams on the upstream side of the constriction. In other cases, however, the strongest winds are not observed in the narrowest region, but downstream of the exit (Chrust et al., 2013), and it is argued that the wind acceleration is mainly due to the increase of the along-valley pressure gradient, which is often largest at the exit (Whiteman, 2000). Atmospheric conditions downwind of the topographic constriction, such as the development of cold pools in mountain basins, may also influence the structure of the exit flow, such as inhibiting its intrusion, and leading the flow to split or become an elevated flow, as observed for downslope winds (Fast et al., 1996; Cuxart, 2008).

The occurrence of LLJs in the very SBL can greatly affect either submeso structures or turbulence, contributing to the production of intermittent turbulence both inside and above the SBL, to the generation of horizontal meandering at the jet nose (Mortarini et al., 2018) or to trigger waves through Kelvin-Helmholtz instability (Cuxart, 2008; Petenko et al., 2020). Relations between turbulence below the jet and LLJ characteristics have been explored by defining a jet Richardson number, computed from jet strength and height (Banta et al., 2003), but useful only for moderately stable cases. On the one hand, turbulence anisotropy seems to be enhanced by the presence of a LLJ, due to larger damping of vertical turbulent motion in such stably stratified conditions (Lampert et al., 2016), and, on the other hand, turbulent potential energy, stored in the vicinity of the jet nose, can be released into localized bursts of sensible heat flux, with intermittent generation of TKE in the vertical direction (Cava et al., 2019). The propagation of exit jets towards the foothills and plain for several kilometers may affect the PBL structure even over apparent flat terrain, and may hinder the formation of a nocturnal inversion layer at the ground, through downward heat fluxes generated by the strong shear below the jet maximum (Banta et al. 2004; Pinto et al. 2006; Kutsher et al. 2012 Figure 3; Mahrt and Acevedo 2022). On the other hand, spreading and collapsing of the exit flow are sensitive to local topographic characteristics, as well as to case by case atmospheric conditions, thus the spatial and temporal evolution may be different from one place to another (Neiman et al., 2019).

A correct representation of such local flows in NWP models, both over flat and complex terrain, is thus important to better capture SBL dynamics. At the same time, this also calls for quantifying the extent to which turbulence and submeso motions are enhanced by such flows, and for including in PBL parameterisation the corresponding mixing, which affects transport both in the horizontal and vertical direction.

1.4 Summary of the thesis

The above introduction focused on the many issues in our understanding of turbulence in stably stratified flows and the related challenges in NWP models, enhanced over complex terrain, which motivated this work. However, not all of them are developed in the following chapters. First, the analysis of sonic anemometer measurements over an Alpine glacier is presented, with a main focus on the anisotropy of the Reynolds stress tensor. We investigate if turbulent motions dominantly in the horizontal plane, and associated with strong anisotropic Reynolds stress tensor, are characterised by different properties of the energy cascade. The contribution of non-turbulent motions to the anisotropy of the Reynolds stress tensor is evaluated, with a main focus on the occurrence of IGWs. Then, we focus on an evaluation of the ability of the Weather Research and Forecasting (WRF) model to correctly reproduce, in high-resolution mesoscale simulations ($\Delta x \sim 300\,\mathrm{m}$), a cold pool event in an Alpine valley and its interaction with the nocturnal local flow, which presents characteristics similar to a valley exit jet close to the intersection of a tributary valley with the main one. Attention is paid to different turbulence closures in the PBL to see if they affect the performance of the model for the case study over complex terrain and in stable conditions. Then, we speculate on possible reasons for the different performance of the turbulence parameterizations, and we discuss the influence of exit jets, and more generally low-level jets, on turbulence production and anisotropy in the SBL.

The overall approach aims at testing several methods that could improve our understanding of turbulence in stratified flows, with the background question of how it would be possible to include these new aspects in turbulence closures.

Chapter 2

Sources of anisotropy in the Reynolds stress tensor in the Stable Boundary Layer

2.1 Introduction

Under a variety of meteorological conditions, the planetary boundary layer (PBL) is characterized by stable stratification. It may develop due to significant radiative cooling of the surface during nighttime under clear sky, or due to advection or subsidence of warm air masses over cold seas or ice, as frequently found in polar regions. Despite its relevance for various environmental hazards of societal importance, such as high concentrations of pollutants, frost and fog formation, a comprehensive understanding of all the processes involved in the stable boundary layer (SBL) is still missing. This is particularly true for very stable conditions, for which turbulence dynamics is hard to predict. In those conditions, turbulence is non-stationary, it strongly interacts with small-scale non-turbulent motions that may have propagated over long distances, and there is a strong interplay between velocity fluctuations and stratification.

Recent contributions focused on identifying different dynamic regimes in the SBL and attempted to parameterize turbulence accordingly. In particular, a classification of the SBL in two dynamic regimes depending on the wind speed was proposed by Sun et al. (2012), and then verified by many experimental (Mahrt et al., 2015; Vignon et al., 2017; Acevedo et al., 2021) and numerical studies (Maroneze et al., 2019a,b; Baas et al., 2019). A site and height-dependent wind speed threshold was found to discriminate between a SBL "decoupled regime", where turbulence is weak, intermittent, mainly controlled by the local shear and does not directly interact with the ground (low wind speed cases), and a "coupled regime", where turbulence is strong, continuous and controlled by the bulk shear (high wind speed cases). As eddies detach from the ground, the Monin-Obukhov similarity theory (MOST) predicts that z is no longer a scaling parameter, and turbulence follows z-less scaling in the decoupled state. However, in very stable conditions, the decoupled state exhibits departures even from this ad-hoc theory. On the other hand MOST was shown to work well for experimental data with close to isotropic Reynolds stress tensors (Stiperski and Calaf, 2018), which implies an equal contribution from the three velocity components of the turbulent kinetic energy (TKE), and experimental data following the -5/3 Kolmogorov power law in the inertial subrange (Grachev et al., 2013).

For very stable stratification, the Reynolds stress tensor is far from isotropic. In fact, Large Eddy Simulations (LES) (Ali et al., 2018) have shown that the most remarkable difference between unstable, neutral and stable atmospheric conditions is the tendency of turbulent stresses for stable stratification to be characterised by velocity fluctuations along one dominant direction in the coordinate system made of the tensor's eigenvectors. This state of anisotropy of the Reynolds stress tensor is called one-component turbulence (Pope, 2000, Table 11.1). Analogous results were found by Falocchi et al. (2019) analysing the dependence of turbulence anisotropy on wind intensity and atmospheric stability. It is worth noting that anisotropic turbulence may exist even in neutral conditions, as it has been observed in canonical turbulent boundary layers, such as fully developed pipe flows (Krogstad and Torbergsen, 2000). In fact, the axisymmetric and isotropic turbulence observed at the core region, close to the centre-line, becomes less axisymmetric and more anisotropic in the logarithmic wall region, with a tendency towards the two-component limit as the wall is approached. This behaviour is further complicated in case of stably stratified boundary layer flows.

For very stable stratification, turbulence does not satisfy the assumptions implied in the derivation of the $-\frac{5}{3}$ power law (Kolmogorov, 1941b). In fact, Kolmogorov theory for the inertial subrange is valid only in neutral conditions and follows from the assumption of a universal character (independent of the flow geometry) of small-scale turbulent motions, determined entirely by the rate at which they receive kinetic energy from the large scales and dissipate it into heat through viscosity. Turbulence in a stable atmosphere is strongly influenced by density stratification, which leads to a viscous dissipation rate that is significantly smaller than the rate of generation of TKE, as part of it is converted into potential energy and smoothed out by molecular conductivity (Bolgiano, 1959; Finnigan et al., 1984; Zilitinkevich et al., 2019). For sufficiently stable stratification, the inertial subrange in the vertical spectra of the horizontal velocity may even disappear (Lang and Waite, 2019) and the entire spectrum is anisotropic (Bolgiano, 1959). Nevertheless, most of the parameterizations for PBL turbulence, both in Reynolds Averaged Navier-Stokes (RANS) simulations and in LES, assume local isotropy for the smallest eddies in order to parameterize the dissipation tensor, which is then computed parametrising only one out of nine terms. RANS simulations generally use closures up to 1.5 order, including a TKE budget equation with viscous dissipation parameterised according to Kolmogorov's law, $\epsilon \propto u^3 l^{-1}$ (Pope, 2000; Vassilicos, 2015). The most common LES models are based on the assumption that the filtering scale is in the inertial subrange and that large scale anisotropic eddies are fully resolved. The unresolved motions are hence expected to be locally homogeneous and isotropic and are parameterized accordingly.

A proper representation of the SBL needs an improvement of the classical theories adopted so far to describe boundary layer flows. This in turn requires a better understanding of the physical processes that cause deviations of turbulence properties from classical theories. In particular, the physical processes leading to turbulence anisotropy will be investigated here.

Sources of anisotropy for eddy-motion in the inertial subrange have been investigated by direct numerical simulations (DNS) (Smyth and Moum, 2000; Lang and Waite, 2019; Kit et al., 2021), laboratory experiments (Atta, 1991) and field studies (Kit et al., 2021). Results suggest that departures from local isotropy may occur because of interactions between the temperature and velocity fields at small scales and direct interactions between the large scale and small scale eddy motions (Katul et al., 1995). Considering anisotropy at larger turbulent scales, Stiperski and Calaf (2018) found that the horizontal velocity spectrum of one-component turbulence has a spectral slope of -2.4 in the low-frequency range, and they pointed out that the value is close to a -3 slope, characteristic of both turbulence, when constrained to a quasi-2D flow, and the canonical gravity wave spectrum, derived from strong nonlinear interactions between turbulence and internal gravity waves (IGWs) (Sukoriansky and Galperin, 2012). Following up on that study, Vercauteren et al. (2019a) showed that one-component turbulence occurred when submeso scale motions and turbulent scales overlapped.

In this work we explore the hypothesis that strong temperature stratifications, such as those occurring over glaciers and typical of the decoupled SBL where one-component turbulence dominates, attenuates turbulent vertical motions enough to enable the development of quasi-2D dynamics. In such quasi-2D dynamics the vortex stretching term is null and the conservation of enstrophy, as well as energy conservation, prevent the downscale cascade of energy. In the spectral range below the forcing wavenumber, the transfer of energy is towards the large scales (backscatter), leading to an inverse cascade (Vallis, 2005, Section 8.3). The organization of the flow into horizontal layers of eddies separated by strong vertical shear, with the formation of horizontal pancake-like structures in physical space (classified as two-dimensional modes by Mahrt, 2014), has already been observed, combined with a tendency of energy to accumulate in the vertical conical region in Fourier space (Sagaut and Cambon, 2018, Figure10.5) for increasing stratification (Sukoriansky and Galperin, 2012). Since a -3 slope with an inverse cascade of energy is usually found in the synoptic range of the energy spectrum, where large-scale flows are constrained by Earth rotation and stratification, we are also indirectly wondering if phenomena generally attributed to large-scale dynamics might also occur at smaller scales. For example, it has been shown by solving numerically and analytically the two-dimensional RANS equations under the assumptions of constant horizontal gradients of wind velocity components and pressure, and neglecting the horizontal gradients of the Reynolds stresses (Oettl et al., 2005), that meandering, a phenomenon occurring at low wind speed in the boundary layer and related to the horizontal oscillations of the wind direction, is an inherent property of the flow when it approaches the geostrophic balance, which is usually attributed to large-scale dynamics. Our hypothesis was also motivated by theories (Schertzer and Lovejoy, 1985; Lovejoy et al., 1993; Lovejoy and Schertzer, 2013) suggesting that there is no spectral gap or a strict separation between two and three dimensional atmospheric motions: small-scale structures are continuously deformed and flattened at larger and larger scales by a scale invariant process, and scaling methods with anisotropic cascades should be proposed.

In large-scale dynamics, both potential energy and kinetic energy need to be included in modelling eddy motions, and the importance of the energy exchanges between them is well known. This concept was also introduced for boundary layer flows in stably stratified atmosphere (Zilitinkevich et al., 2007). By properly scaling the equation for temperature variance to have a prognostic equation for turbulent potential energy (TPE), it becomes apparent that the buoyancy term involving vertical heat fluxes may transfer energy between the potential energy reservoir and the kinetic energy of the turbulent field, as the same term appears with opposite sign in the TKE equation. One-dimensional RANS simulations highlight the importance of this energy exchange mechanism for resolving the transition between the coupled and decoupled regime of the SBL. By comparing results from models with an increasing number of prognostic equations for turbulent variables, Maroneze et al. (2019a) showed that the weak-wind regime can be properly reproduced only if the vertical heat flux and the temperature variance are solved by prognostic equations. Further investigations with a second-order closure numerical model (without prognostic equations for the horizontal momentum flux and the vertical velocity variance) have shown that the vertical heat flux controls the transition between the coupled and decoupled regime of the SBL, despite its small magnitude (Maroneze et al., 2019b).

An important source of temperature fluctuations at low frequencies in strongly stratified flows are IGWs. Stiperski and Calaf (2018) proposed IGWs as the other possible cause to explain the spectral slope found in the low-frequency range of one-component Reynolds stresses, in agreement with the spectral transition from -3 to $-\frac{5}{3}$ observed at the Ozmidov wavenumber in strongly stratified flows (Alisse and Sidi, 2000; Sukoriansky and Galperin, 2012; Lang and Waite, 2019). Thus, the second hypothesis that we explore in this work is if IGWs are related to the occurrence of Reynolds stresses towards the one-component limit, also at smaller scales. More generally, it has been shown that submeso motions, such as wave-like motions, gravity currents or vortical structures between the mesoscale and the largest turbulent eddies, may trigger turbulence events in the most stable regime with Richardson number above the critical value 0.25, and affect vertical velocity fluctuations at small scales (Vercauteren and Klein, 2015; Vercauteren et al., 2016). The lack of a spectral energy gap in the SBL between the submeso scales and the turbulence in the case of strong submeso activity, and the relation with a Reynolds stress tensor towards the one-component limit have been recently pointed out by Vercauteren et al. (2019a) with a statistical clustering technique. DNS of turbulence resulting from Kelvin-Helmholtz instability in stably stratified shear flow indicate that one-component eddies are mainly present in the decay phase of the disturbance (Smyth and Moum, 2000; Wingstedt et al., 2015), and some authors associate that with jet-like motions (Wingstedt et al., 2015). By performing analogous DNS but in a very large computational domain, Watanabe et al. (2019) attested the formation of highly elongated structures with positive and negative streamwise velocity fluctuations, and Watanabe and Nagata (2021) showed that their contribution to the Reynolds stress tensor is towards the one-component limit. DNS including the effect of rotation, which corresponds to the stably stratified Ekman flow, also revealed elongated streaky regions (slow-moving fluid) close to the wall (Harikrishnan et al., 2021). Laboratory experiments

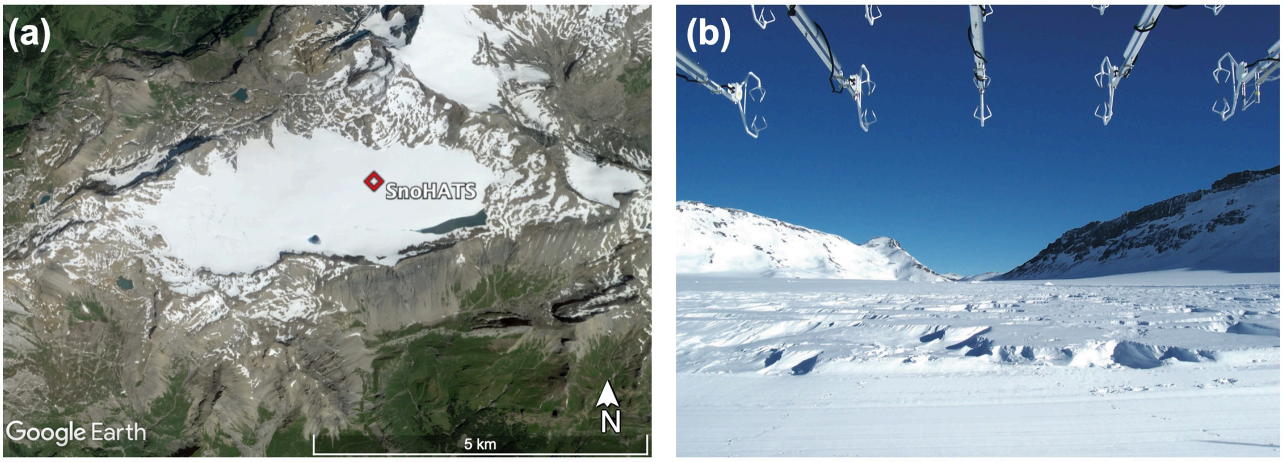

Figure 2.1: Experimental site of the field campaign Snow-Horizontal Array Turbulence Study (SnoHATS). Panel (a) shows the location of the sonic anemometers on an aerial photo of the Plaine Morte Glacier (background map from Google Earth), and panel (b) shows the two arrays of sonic anemometers, pointing to the East direction.

performed in wave flumes (Longo et al., 2017; Singh et al., 2021) found evidences that one-component eddies are related to surface waves superimposed over steady currents, suggesting that the modulation of the flow at lower frequencies may alter turbulence fluctuations at higher frequency.

Thus, the main questions that will be addressed in the present chapter are: how are the coupled and decoupled regimes of the SBL related to the anisotropy of the Reynolds stress tensor at small scales? Are the mechanisms of exchange of energy in one-component limiting state similar to those in quasi-2D flows, both in large/small scales energy transfer and in TKE/TPE transfer? Is there a relation between IGWs and the anisotropy of the Reynolds stress tensor? We address these questions analysing data from the Snow-Horizontal Array Turbulence Study (SnoHATS) dataset, which is described in Section 2.2. Section 2.3 introduces the invariant decomposition to study the anisotropic properties of the Reynolds stress tensor, together with a filtering approach to investigate energy transfers across scales, and a diagnostic method for IGWs detection based on cross-spectral analysis. Results are then presented and discussed in Section 2.4, while conclusions are drawn in Section 2.5.

2.2 Observations

The analysis performed in this work is based on field measurements from the SnoHATS experimental campaign (Bou-Zeid et al., 2010). The dataset was collected over the Plaine Morte Glacier in the Swiss Alps (46.38638 °N, 7.51788 °E, 2750 m a.s.l., Figure 2.1a) from February 2 to April 19, 2006 and the instruments' setup was originally designed to study small-scale turbulence in the stable atmospheric surface layer and related parameterizations in LES. Twelve sonic anemometers (sampling frequency 20 Hz)

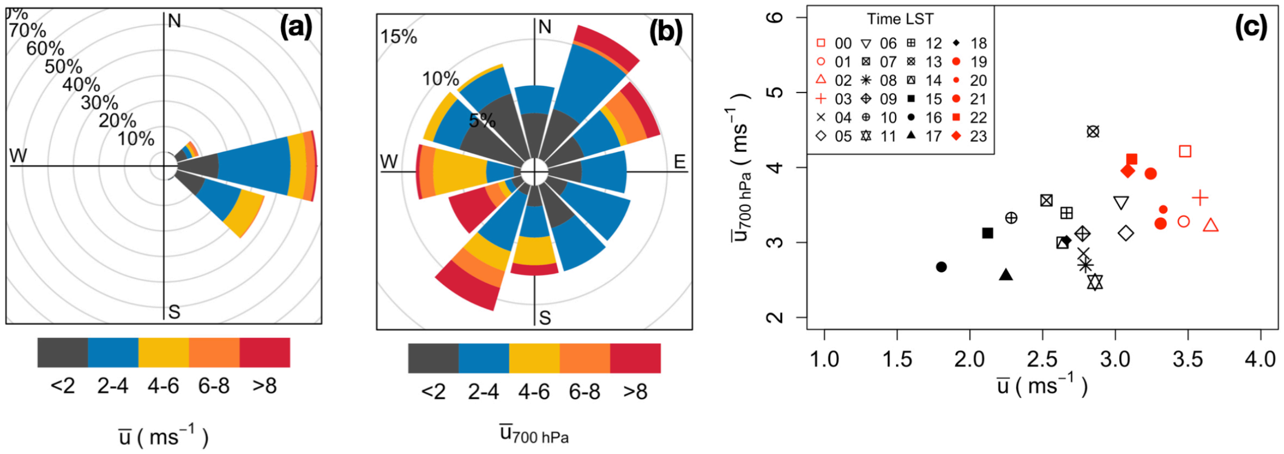

Figure 2.2: Hourly wind roses from SnoHATS measurements and the ERA5 dataset. Panel (a) shows the wind rose computed collecting hourly averages from all the sonic anemometers, based on $\sim$ 1 min windows selected for data analysis. Panel (b) shows the wind rose based on ERA5 hourly averages, at 700 hPa at the geographical point closest to the SnoHATS location. Both wind roses include only hours corresponding to periods with at least 50% of $\sim$ 1 min windows selected for data analysis. Panel (c) compares those hourly wind speed, averaged according to the hour of the day.

were deployed for the campaign, arranged in two vertically-separated horizontal arrays with five sonics in the top layer and seven in the bottom layer (Figure 2.1b), in order to allow for computation of the full three-dimensional gradients of the measured fields. The separation between neighbouring sonics was 0.80 m in the horizontal and 0.77 m in the vertical direction for data collected until March 14, then the vertical distance was increased to 0.82 m. Instruments' height above ground level changed according to snow cover on the surface of the glacier, with the bottom array at a height between 0.62 m and 2.92 m above snow level. Sonic anemometers pointed to the East and data analysis was restricted to winds blowing from ±60° with respect to this direction. This ensures that the instruments are in the internal equilibrium layer because winds are blowing over a long fetch of flat snow (Figure 2.1b, $\sim$ 1500 m). Additionally, easterly winds at the field site are typically dry and associated with days of clear sky, low-synoptic forcing conditions and no precipitations (Bou-Zeid et al., 2010), thus ensuring the best operating conditions for the instruments. Low-quality data (including snow-covered sonics, power outages, and other instrumental issues) were removed, thus leaving non-continuous periods equivalent to 14×24 hours of data for the analysis. The data selected were collected under weak synoptic forcing conditions, as shown in Figure 2.2b by the wind rose referring to the standard isobaric level closest to the measurement altitude (700 hPa) at the geographical point closest to the SnoHATS location. The wind rose is obtained from hourly data from the ERA5 reanalysis, provided by the European Centre for Medium-Range Weather Forecasts (ECMWF), including only hours corresponding to periods with at least 50% of 1-min windows selected for data analysis. Wind speed at 700 hPa is mainly below 6 m s^{-1} and without any preferred direction, highlighting that the selected observed easterly winds (Figure 2.2a) are decoupled from large-scale motion. On the other hand, the observed easterly winds might be associated with thermally-driven local flows. Indeed, the upwind fetch has a gently rising inclination ($\sim 2°$), ending with a ridgeline, which might drive thermally-driven katabatic winds. Figure 2.2c compares hourly wind speeds at 700 hPa with those measured by the sonics, averaged according to the hour of the day. The latter were obtained by computing hourly averages from $\sim$ 1 min periods, including only hours with at least 50% of periods selected for data analysis. The length of the data periods was chosen consistently with the turbulence analysis, as will be explained in Section 2.3.1. This comparison confirms that the measured wind speed, which exhibits low variability, is not influenced by the synoptic wind. On the other hand, stronger wind speeds are clearly characterizing nighttime hours, marked in red in Figure 2.2c, thus supporting the hypothesis that topography contributes to the development of stronger easterly winds during nighttime.

To evaluate turbulent quantities, previous analyses of the cospectral gap (Vercauteren et al., 2016) suggested 1-min averaging windows, which should minimise the contamination from non-turbulent motions for weak-wind stable conditions. This time window is also used in this work. Data were processed using double rotation and applying linear detrending. The influence of the latter procedure to evaluate the state of turbulence anisotropy will be discussed in Section 2.3.1. The anisotropy analysis is based on quantities that are invariant to the coordinate system, hence the double rotation has no influence on the results. In case the planar-fit technique is used for data analysis, attention should be paid to a possible influence on the results, but this method is not used in the present work.

2.3 Methods

2.3.1 Anisotropy of the Reynolds stress tensor

The Reynolds stress tensor is a (symmetric) second-order 3D tensor (positive semidefinite) and, as such, it may be decomposed into an isotropic and an anisotropic deviatoric (trace-free), part:

$$\overline{u_i' u_j'} = \frac{2k}{3}\delta_{ij} + a_{ij} \tag{2.1}$$

where u_i' are velocity fluctuations with respect to a time average, denoted by an overbar, δ_{ij} is the Kronecker delta and $k = \frac{1}{2}\left(\overline{u_1'^2} + \overline{u_2'^2} + \overline{u_3'^2}\right)$ is the TKE. The TKE is half the trace of the Reynolds stress tensor, and since the trace is the first principal invariant of a tensor, TKE does not depend on the frame of reference in which velocity fluctuations are measured. Only the deviatoric part a_{ij} is effective in transporting momentum, while the isotropic stresses can be simply absorbed in a modified mean pressure term. The analysis of the normalized anisotropic Reynolds stress tensor $b_{ij} = \frac{a_{ij}}{2k} = \frac{\overline{u_i' u_j'}}{2k} - \frac{1}{3}\delta_{ij}$ has recently received increasing attention to improve turbulence parameterizations in the atmospheric surface layer (Stiperski and Calaf, 2018) or to develop new methodologies for uncertainty quantification of turbulence closures in RANS or LES approaches (Emory et al., 2013; Jofre et al., 2018; Mishra et al., 2020). The symmetry of b_{ij} ensures diagonalizability of the matrix, whose components in the diagonal form in the principal coordinate system (pcs) are the three matrix's eigenvalues, $(\lambda_1, \lambda_2, \lambda_3)$ with $\lambda_1 \geq \lambda_2 \geq \lambda_3$, which are real and can be computed by built-in functions in different programming languages (such as the *eigen()* function in R language). The sum of the three eigenvalues is equal to the trace of b_{ij}, which is identically zero by definition, thus the tensor has only two independent eigenvalues, (λ_1, λ_2). Moreover, from Eq. 2.1 it can be seen that a diagonal $b_{ij,pcs}$ corresponds to a diagonal Reynolds stress tensor $\overline{u_i'u_j'}_{pcs}$. Since the eigenvalues of $\overline{u_i'u_j'}_{pcs}$ are non-negative by definition and their maximum value is $2k$, none of the eigenvalues of b_{ij} can be smaller than $-1/3$ (corresponding to a vanishing $\overline{u_i'u_j'}_{pcs}$ in that component), or greater than $2/3$ (corresponding to only one not-vanishing $\overline{u_i'u_j'}_{pcs}$ component). Combining the information of two independent eigenvalues with these constraints, it is possible to define two-dimensional maps, where any turbulent state is represented by a point in a bounded region.

The barycentric map, used in this work and proposed by Banerjee et al. (2007), is represented by an equilateral triangle, whose vertices correspond to the three limiting states of the turbulent stress tensor: one-component limit (1c) with one eigenvalue much larger than the other two, two-component limit (2c) with two eigenvalues of comparable magnitude, much larger than the third eigenvalue, three-component limit (3c) corresponding to the isotropic case with three equal eigenvalues. Eigenvalues can also be called component-energies (Lumley, 1987, Pag 131), because they relate to the TKE distribution, and the map shows the shape of the energy ellipsoid associated with the turbulent stress tensor. It is important to stress that this shape is not the shape of the turbulent structures in physical space: one-component turbulence is not a turbulent eddy with a cigar-like (1D) spatial structure, but with a cigar-like energy ellipsoid, while two-component turbulence is not a pancake-like (2D) spatial eddy, but a turbulent eddy with a pancake-like energy ellipsoid. The Reynolds stress tensor carries only information on componentiality (i.e. the relative strength of different velocity fluctuations in the principal coordinate system) not on dimensionality (i.e. the relative uniformity of structures in different directions), which can be studied with other one-point tensors (Kassinos et al., 2001). Moreover, componentality is defined in the principal coordinate system, thus it is not straightforward to relate measured velocity-variances and limiting states of anisotropy. This would be possible only if the measured Reynolds stress tensor is diagonal because principal axes would coincide with those of the reference system used.

To plot a point inside the barycentric map, corresponding to a specific Reynolds stress tensor, barycentric coordinates (x_B, y_B) have to be computed from the two independent and largest eigenvalues λ_1, λ_2 of b_{ij}:

$$\begin{aligned} C_{1c} &= (\lambda_1 - \lambda_2) \quad C_{2c} = 2\,(2\lambda_2 + \lambda_1) \quad C_{3c} = (1 - 3\lambda_1 - 3\lambda_2) \\ x_B &= C_{1c}x_{1c} + C_{2c}x_{2c} + C_{3c}x_{3c} \\ y_B &= C_{1c}y_{1c} + C_{2c}y_{2c} + C_{3c}y_{3c} \end{aligned} \tag{2.2}$$

where (x_{ic}, y_{ic}) are the coordinates of the limiting states located at the vertices of the equilateral triangle and can be arbitrarily chosen. In this work we chose to have the two-component axisymmetric limit in the origin of the coordinate system, with $(x_{2c}, y_{2c}) = (0, 0), (x_{1c}, y_{1c}) = (1, 0), (x_{3c}, y_{3c}) = (1/2, \sqrt{3}/2)$ (Figure 2.3). The map has the advantage that every point is associated with a triplet C_{1c}, C_{2c}, C_{3c}, that quantifies the contribution of each limiting state of anisotropy to that particular state of the tensor. The center represents turbulence with an equal contribution of the three limiting states and any vertex has only one non-zero contribution equal to 1, decreasing to zero on the side opposite to that vertex. As summarized in Banerjee et al. (2007, Section 2.4), many types of two-dimensional maps with different boundary lines can be constructed to characterize the anisotropy of the Reynolds stress tensor. They are all based on the eigenvalues or invariants of the tensor, thus not dependent on the frame of reference in which the Reynolds stress tensor is measured. In this work the barycentric map is adopted because it avoids visual distortions occurring in other maps, such as visual impression of axisymmetry for turbulent flows that fall in the center of the barycentric map (Banerjee et al., 2007, Figure 5), thus it is the most suitable map to investigate Reynolds stress tensors towards the one-component limit, which is commonly observed in the SBL (Vercauteren et al., 2019a). We adopt this map to investigate anisotropy of turbulent eddies within the SnoHATS dataset and we mainly focus on the pure anisotropic states, following the method suggested by Stiperski and Calaf (2018, their Figure 4). Pure states are determined as those periods falling inside the kite-shaped regions of the barycentric map, as shown in Figure 2.3. The limiting lines were chosen to cover 70% of the sides of the equilateral triangle, with the left region (blue lines) representing Reynolds stress tensors towards the two-component state, the right region (red lines) those towards the one-component limit and the upper region (yellow lines) those towards the isotropic state.

Effects of linear detrending

Reynolds averaging method to estimate turbulent statistics should be applied to steady-state conditions, which are rarely encountered in the atmosphere. The diurnal cycle and/or changes in meteorological conditions may contaminate the turbulent signal with trends, adding low-frequency contributions. It is then common to remove the long term trends, which are generally approximated as linear. It is up to the investigator to choose the length of the measurement period and whether or not detrending should be used, but it is generally applied to windows of 30 min (Forrer and Rotach, 1997) or more (Foken, 2008). Detrending of shorter time windows may remove part of the turbulent energy in the calculated statistics and it is a disputed point of turbulence data analysis

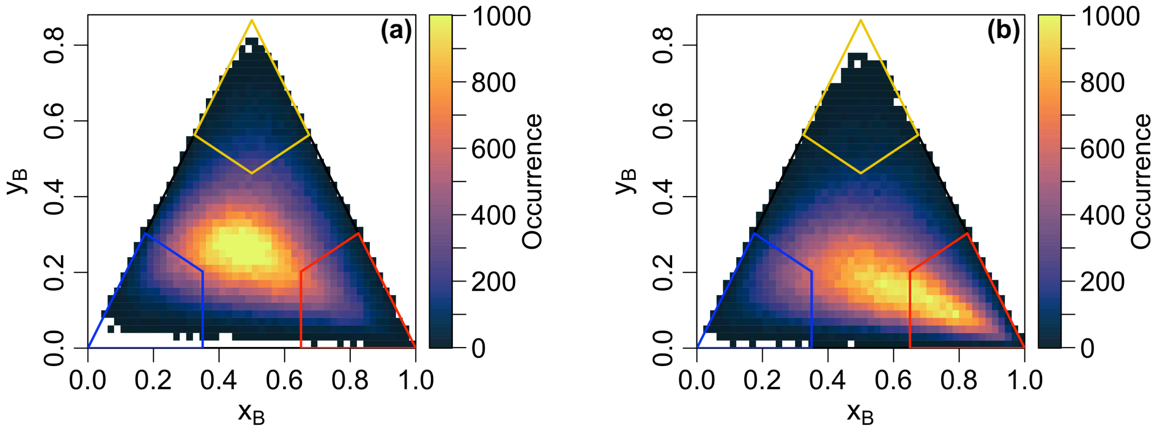

Figure 2.3: Barycentric maps with the occurrence of all ∼1 min Reynolds stresses computed from measurements from the twelve sonic anemometers. Red, blue and yellow edges correspond to the area selected as one-component turbulence, two-component axisymmetric turbulence and isotropic turbulence (Stiperski and Calaf, 2018). Panel (a) shows the occurrence of the Reynolds stress tensors computed by linear detrending the data before stresses' computation. Panel (b) shows the occurrence without applying a linear detrending procedure.

(Večenaj and De Wekker, 2015). The influence of nonstationarity can also be reduced by decreasing the size of the window and previous studies in the SBL have shown that averaging times shorter than a few minutes often correspond to the observed cospectral gap, that separates turbulence and larger-scale processes (Vickers and Mahrt, 2003).

Linear detrending is not frequently applied to 1-min (or few minutes) time windows (Mahrt et al., 1998; Sun et al., 2012; Mahrt et al., 2020; Boyko and Vercauteren, 2021), but it was found to strongly influence the anisotropy analysis of the Reynolds stress tensor in our study. Figure 2.3 shows the 2D probability density distribution of points in the barycentric map for data subjected a) or not b) to this procedure. In particular, detrending the data reduces the amount of periods falling towards the one-component limit. As the existence of a trend may be interpreted as non-stationarity within the observed time interval, our results are in agreement with Stiperski and Calaf (2018), who found that the amount of one-component stresses is strongly reduced when non-stationary nighttime counter-gradient fluxes are discarded from the analysis. The detrending procedure mainly tends to move periods towards the center of the triangle, where turbulence has an equal mix of the three limiting states, but there are also a few detrended periods that come closer to the one-component limit.

Since we are interested in evaluating the anisotropy of turbulence, we chose to apply the detrending procedure even to this small time window, in order to avoid including this specific contribution from non-stationary external forcings in the components of the Reynolds stress tensor. We will explore linear trends and their sources as a physical reason for one-component anisotropy in Section 2.4.5.

2.3.2 Energy transfer across scales: Coarse-graining approach

In order to investigate the hypothesis that an inverse cascade of kinetic energy may occur in the SBL, according to the state of anisotropy of the Reynolds stress tensor, we employ a coarse-graining approach, commonly used as a modelling tool by the LES community for subgrid scale processes (Pope, 2000, Chapter 13). This approach allows a direct computation of subfilter contributions from highly-resolved fields, such as the ones measured during SnoHATS campaign and testing the assumptions of LES, in order to improve subgrid scale parameterizations. For example, Bou-Zeid et al. (2010) used the SnoHATS dataset to investigate the effects of different filter scales and the role of thermal stability on the coefficients of the Smagorinsky model, when the filter scale is not supposed to be in the inertial subrange of the turbulence spectrum. Many other field campaigns were performed in the atmospheric surface layer for similar purposes (Davis99 experiment: Porté-Agel et al., 2001; HATS experiment: Horst et al., 2004; SLTEST: Carper and Porté-Agel, 2004; SGS2002: Higgins et al., 2007). However, this approach is very general and, when applied to compute the kinetic energy of the unresolved scales, it may be interpreted as a tool to study the energy transfer across scales, and this is the way we use this approach in this work. Unlike Kolmogorov theory, this method does not rely on assumptions and can assess the direction of the energy flux directly, in contrast to the usual spectral analysis where the same power-law scaling may have multiple interpretations (as in the case of the -3 slope found in Stiperski and Calaf, 2018 or the long-standing debate about the synoptic-to-mesoscale transition, Callies et al., 2014).

The method is exactly derived from the equations governing the conservation of mass and momentum by applying a filtering operator to the atmospheric fields, which leads to the following equations:

$$\begin{aligned}
\frac{\partial \widetilde{u}_i}{\partial t} + \frac{\partial \widetilde{u}_i \widetilde{u}_j}{\partial x_j} &= -\frac{1}{\rho}\frac{\partial \widetilde{p}}{\partial x_i} - \delta_{i3}\frac{\widetilde{\theta} - \langle \widetilde{\theta} \rangle}{\widetilde{\theta}_0} g + \nu \frac{\partial^2 \widetilde{u}_i}{\partial x_j \partial x_j} - \frac{\partial(\widetilde{u_i u_j} - \widetilde{u}_i \widetilde{u}_j)}{\partial x_j} \\
\frac{\partial \widetilde{u}_i}{\partial x_i} &= 0
\end{aligned} \tag{2.3}$$

where buoyancy effects are accounted under the Boussinesq approximation, with the brackets $\langle\rangle$ used to represent a horizontal average (Carper and Porté-Agel, 2004). The filtered field ($\widetilde{\cdot}$) is obtained by a convolution of the original field with a function $G_\Delta(\vec{x})$, defined on a compact support or with fast decay, which is normalized and has a characteristic width Δ. In the Fourier space it corresponds to a low-pass filter of cutoff wavenumber $k_c = \frac{\pi}{\Delta}$. This filtering operation allows to obtain a decomposition of the flow, locally both in space and time, at any desired scale Δ. The kinetic energy of scales larger than Δ is defined as $KE^\Delta = \frac{1}{2}\widetilde{u}_i\widetilde{u}_i$ and its evolution in time can be derived by taking the dot product of Eq. 2.3 with $\widetilde{u}_i$:

$$\frac{\partial KE^\Delta}{\partial t} + \widetilde{u}_j \frac{\partial KE^\Delta}{\partial x_j} = -\frac{1}{\rho}\widetilde{u}_i \frac{\partial \widetilde{p}}{\partial x_i} - \widetilde{u}_3 \frac{\widetilde{\theta} - \langle \widetilde{\theta} \rangle}{\widetilde{\theta}_0} g + \nu \widetilde{u}_i \frac{\partial^2 \widetilde{u}_i}{\partial x_j \partial x_j} - \widetilde{u}_i \frac{\partial \tau_{ij}}{\partial x_j} \tag{2.4}$$

where $\tau_{ij} = \widetilde{u_i u_j} - \widetilde{u}_i \widetilde{u}_j$ is the subgrid stress term. The last term on the right-hand side can be written as:

$$\widetilde{u}_i \frac{\partial \tau_{ij}}{\partial x_j} = \frac{\partial \widetilde{u}_i \tau_{ij}}{\partial x_j} - \tau_{ij} \frac{\partial \widetilde{u}_i}{\partial x_j} = \frac{\partial \widetilde{u}_i \tau_{ij}}{\partial x_j} - \tau_{ij} \frac{1}{2} \left(\frac{\partial \widetilde{u}_j}{\partial x_i} + \frac{\partial \widetilde{u}_i}{\partial x_j} \right) = \frac{\partial \widetilde{u}_i \tau_{ij}}{\partial x_j} - \tau_{ij} \widetilde{S_{ij}} \qquad (2.5)$$

where $\widetilde{S_{ij}}$ is the resolved strain rate tensor.

The inertial contribution, $\Pi^{\Delta} = -\tau_{ij}\widetilde{S_{ij}}$, corresponds to the rate at which kinetic energy is transferred, by the nonlinear term, from motions of size larger than Δ to motions of smaller size, with positive (negative) values corresponding to a forward (backward) transfer of energy. This term is usually called subgrid scale dissipation by the LES community, but this terminology is inappropriate because, unlike the true dissipation, Π^{Δ} is due entirely to inviscid, inertial processes and it can be negative (Pope, 2000, Section 13.3.3). In fact, while on average the value of Π^{Δ} is positive, DNS of isotropic turbulence (Domaradzki et al., 1993) and DNS of a fully developed pipe flow (Brun et al., 2006), as well as studies about LES parameterizations in the atmospheric surface layer based on field measurements (Carper and Porté-Agel, 2004), suggest that, locally, backscatter contributes significantly to the overall transfer of energy across the filter scale and it should be suitably represented in models to yield correct flow statistics. Boussinesq eddy-viscosity models are absolutely dissipative (unless negative eddy-viscosities are allowed) and backscatter is generally included in models by adding nonlinear contributions to the relation between the subgrid stress tensor τ_{ij} and the resolved strain rate tensor $\widetilde{S_{ij}}$ (Kosović, 1997). Backscatter of energy is generally associated with the formation of large coherent structures in the flow field (Carper and Porté-Agel, 2004) and in this work we investigate, through Π^{Δ}, if it can also be related to different turbulent topologies, according to the state of anisotropy of the Reynolds stress tensor, driven by strong thermal stratification. Such a coarse graining approach based on Π^{Δ} was recently used to characterize the energy transfer in the hurricane boundary layer from aircraft measurements (Sroka and Guimond, 2021) and to map out the energy pathways in the North Atlantic Ocean from simulated global ocean data (Aluie et al., 2018).

To compute Π^{Δ}, we follow the procedure applied by Bou-Zeid et al. (2010) to the SnoHATS dataset, where the tilde in Eq. 2.5 corresponds to a 2D horizontal spatial filter, while no filtering is applied in the vertical direction. The filtering operation is separately applied to four groups of five sonics each (as summarized by the scheme in Figure 2a of Bou-Zeid et al. (2010)) and consists first of a box filter of size Δ in the spanwise direction, which is simply the spatial average of the five measured fields in each group, and second to a Gaussian filter in the streamwise direction. Taylorâs hypothesis is invoked to convert time series to streamwise spatial series and the second filtering operation is applied in the wavenumber space, thus taking the product of the Fourier transform of the four (box filtered) time series with $G(k_1) = \frac{1}{24} \exp\left(-\Delta^2 k_1^2\right)$, where k_1 is the streamwise wavenumber. Taylor's hypothesis may not be appropriate for the most stable regimes, but it is commonly used also in the SBL due to the lack of a better alternative. Possible inaccuracies mainly concern smaller eddies in the inertial subrange, as it is suggested that they are advected at lower velocities than the mean wind speed

(Cheng et al., 2017), and submeso motions, which might not be transported by the local flow (Lang et al., 2018; Pfister et al., 2021). We do not expect these issues to critically influence our results, as we applied the hypothesis to short enough windows, with an averaging time of ~1 min. The characteristic width Δ of the box filter is not simply the spatial distance ($4 \cdot 0.8\,\mathrm{m}$) between the five sonic anemometers in each group. As explained in Carper and Porté-Agel (2004), their Figure 1b, a factor $\cos\delta$, with δ the angle between the direction of the mean wind and the direction perpendicular to the horizontal arrays of sensors, has to be included, in order to account for the true separation between neighbouring sensors in the spanwise direction. Thus, $\Delta = 4 \cdot 0.8\,\mathrm{m} \cdot \cos\delta$, and according to our restriction on wind direction, described in Section 2.2, $\Delta_{min} = 1.6\,\mathrm{m}$ and $\Delta_{max} = 3.2\,\mathrm{m}$, with 90% of data in the range $[2.2\,\mathrm{m}, 3.2\,\mathrm{m}]$. The same width Δ is used to define the Gaussian filter in the streamwise direction and these values of Δ are the smallest achievable with the SnoHATS setup, if the same spatial resolution is required in both horizontal directions.

Filtered fields are then available at four points (P1,P2,P3,P4) and streamwise, spanwise and vertical derivatives are obtained at point P2 by finite differences (as summarized by the scheme in Figure 2b of Bou-Zeid et al. (2010)).

2.3.3 Internal gravity waves: Cross-spectral analysis

Key ingredients of stably stratified turbulence are wave-like motions (Mahrt, 2014), such as dirty waves, solitary waves (which are characterised by a single cycle) or IGWs, which may be generated by several mechanisms, including topographic forcing, dynamical instabilities (*i.e.* shear instability, microfronts or mesoscale fronts) and wave-wave interactions (Staquet and Sommeria, 2002). They manifest as fluctuations in the velocity, pressure, and temperature fields. Different methods may be used to separate IGWs from turbulent motions (Sun et al., 2015a) to properly filter out wavy oscillations, which may lead to turbulent flux overestimation (Cava et al., 2015). In this work a simple diagnostic method is applied, since our goal is to identify the existence of waves and investigate their influence on the anisotropy of the Reynolds stress tensor at small scales. Our approach is based on linear wave theory (Stull, 1988), which provides most of our understanding of waves. Although it ignores turbulence and irreversible interactions between background flows and waves, it is found to approximately capture the important wave characteristics (such as wave periods, wavelengths and phase velocity), even for observed nonlinear waves (Sun et al., 2015b, Section 2.1).

Linear wave theory predicts a phase shift of ±90° between the time series of vertical velocity and scalars for gravity wave events (Stewart, 1969). Thus, the wave-related heat flux $w''\theta''$ (where the double prime denotes wave perturbations with respect to the mean field) would be zero when averaged over an integer number of wave periods. The individual components u'' and w'', instead, are ±180° out of phase, thus linear waves can transport momentum vertically, but cannot transport heat or other scalars. The portion of any spectrum composed of linear IGWs can be identified using cross-spectral techniques, which determine the relationship between the two time series, in our case vertical velocity and temperature, as a function of the frequency. From the Fourier transform of

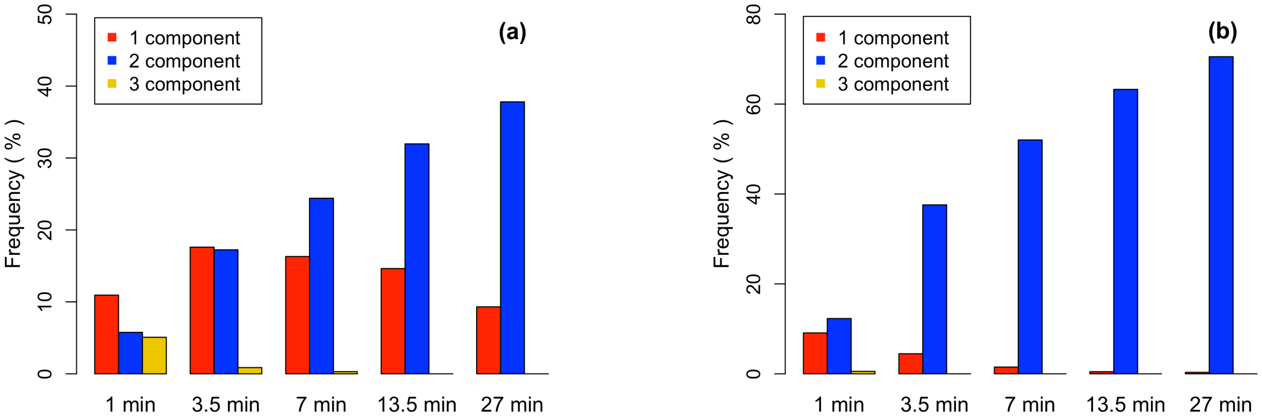

Figure 2.4: Barplots showing the percentage of Reynolds stress tensors in different limiting states of anisotropy, as defined by the edges in Figure 2.3. Each group corresponds to a different time averaging period. Panel (a) corresponds to periods with $\overline{u} \leq 3.5\,\mathrm{ms}^{-1}$ and panel (b) to periods with $\overline{u} > 3.5\,\mathrm{ms}^{-1}$.

their cross-correlation, the real part defines the cospectrum $Co_{w\theta}(f)$, whose integral represents the covariance, and the imaginary part defines the quadrature spectrum $Q_{w\theta}(f)$, which is equal to the spectrum of the product of w and θ phase shifted by 90°. The phase spectrum can be constructed from $Co_{w\theta}(f)$ and $Q_{w\theta}(f)$, generally averaged over similar periods, as:

$$Ph_{w\theta}(f) = \arctan\left(\frac{Q_{w\theta}(f)}{Co_{w\theta}(f)}\right) \tag{2.6}$$

$Ph_{w\theta}$ represents the average phase difference between w and θ that yields the greatest correlation at each frequency. IGWs and turbulence have different cross-spectral phase signatures: frequencies characterized by IGWs are identified by a phase shift of $\pm 90°$, while turbulence, being a chaotic motion, has phase angles randomly distributed between $-180°$ and $180°$. This difference provides a method to discriminate IGWs from turbulence, which is widely used in the SBL (Rees et al., 2000; Ohya and Uchida, 2003; Cava et al., 2004; Zeri and Sá, 2011; Cava et al., 2015). In this work cross-spectral analysis is applied to ∼14 min periods, motivated by the typical wavelengths of IGWs in the SBL. These periods are classified according to the anisotropy of the Reynolds stress tensors at ∼1 min, in order to investigate if Reynolds stresses towards the one-component limit may be related to the contribution of IGWs. A period is labelled as one- or two-component if at least 50% of the included 1-min periods belongs to that particular state of anisotropy, as further explained in Section 2.4.4.

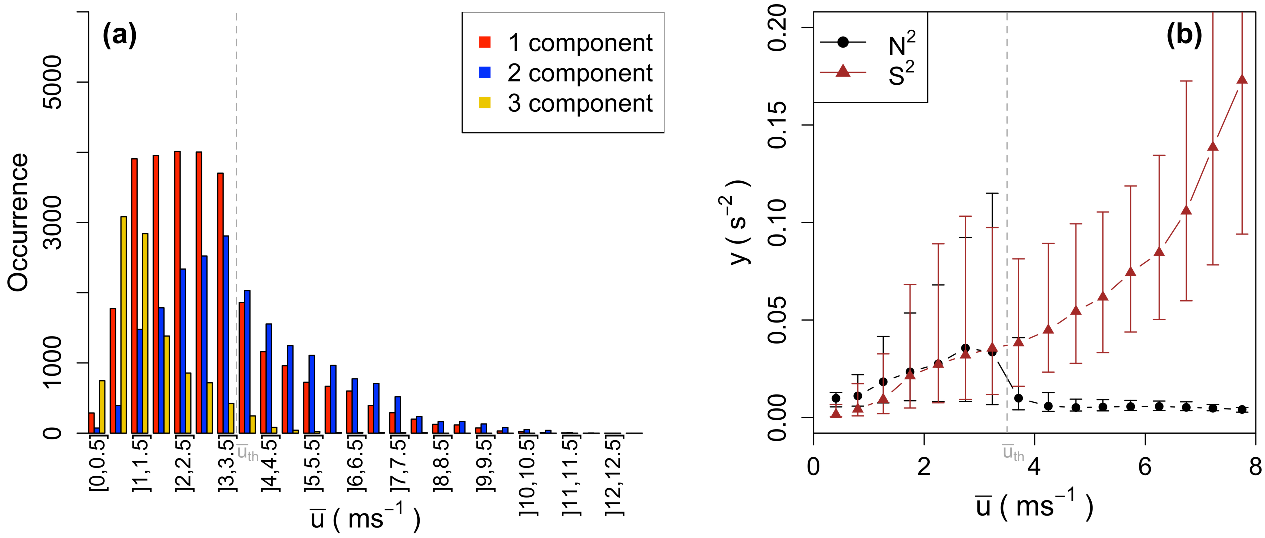

Figure 2.5: Panel (a) shows a barplot with the percentage of Reynolds stress tensors, with a time averaging period of $\sim$1 min, belonging to a particular limiting state of anisotropy, where each group corresponds to a range of mean wind speed. Stresses and mean wind speed are computed for each sonic anemometer and then collected together. Panel (b) shows the median and the interquartile range (Q_1, Q_3) of the squared Brunt-Vaisala and shear frequencies, computed using finite differences and averaging measurements from the upper and lower arrays of sonics.

2.4 Results

2.4.1 Anisotropy of the Reynolds stress tensor

Turbulence in a stratified shear layer exhibits significant anisotropy both at large and small scales (Piccirillo and Atta, 1997; Smyth and Moum, 2000; Lang and Waite, 2019). Figure 2.4 shows the distribution of the three limiting states of anisotropy according to different scales, obtained changing the data-window from $2^{10} \sim 1$ min to $2^{15} \sim 30$ min. Anisotropy of the Reynolds stress tensor may be affected by many external parameters, and it is difficult to quantify the influence of each of them. Here we focus on stratification and wind speed, and we do not separate data according to the height above snow level. However, previous studies (Vercauteren et al., 2019a, their Figure 7), with measurements spanning from 1 m to 30 m above ground level, have shown an almost constant percentage of one-component states with height, which is the limiting state of anisotropy mainly addressed in this work. We use data from all sonic anemometers and we classify them into weak wind speed ($\overline{u} \leq 3.5\,\mathrm{ms}^{-1}$, Figure 2.4a) and strong wind speed ($\overline{u} > 3.5\,\mathrm{ms}^{-1}$, Figure 2.4b) periods. Figure 2.4b shows that two-component axisymmetric Reynolds stress tensors are the most frequent for large wind speed, regardless of the window size investigated. However, they become increasingly more common with the longer time averaging period, which is also the case in the low wind speed regime (Figure 2.4a). As suggested by Ali et al., 2018 and Chowdhuri et al., 2020, this may be related to lower wall-normal velocity compared to the horizontal velocity components in larger structures, constrained by their interaction with the surface. The percentage of eddies in the one-component edge is very different for the two cases, with a negligible occurrence at large wind speed, decreasing with the size of eddies (Figure 2.4b). For low wind speed (Figure 2.4a), instead, the percentage of one-component Reynolds stress tensor is almost constant, prevailing over two-component anisotropy at the smallest scale. It is interesting to note that, even close to the ground, isotropic eddies can exist at the smallest scales at low wind speed. This seems to be typical of the decoupled SBL, where local-shear generated eddies are too small to interact with the ground directly (Sun et al., 2012), and thus turbulent kinetic energy is distributed more uniformly in the three components. Multi-resolution flux decomposition (MRD, Vickers and Mahrt (2003), explained in detail in Appendix A) analysis shows that the cospectral gap scale depends on the wind speed regime (not shown), but most of the turbulent transport occurs at scales below ∼1-min even for large wind speed. Thus, the following analysis is based on ∼1-min averaging windows, which minimise the contamination from non-turbulent motions for weak-wind stable conditions. In strong-wind conditions, on the one hand this choice may discard a small part of turbulent contributions to the Reynolds stress tensor due to larger eddies, however their contribution would always be towards the two-component axisymmetric limit (Figure 2.4b). On the other hand, additional one-component states are included in the analysis, but we do not expect them to significantly influence the results.

As shown in Figure 2.3a, mixed states of anisotropy, i.e. towards the middle of the barycentric map, are the most common ones, in agreement with the results of Vercauteren et al. (2019a). They also found a different distribution of the anisotropic limiting states for dynamic regimes classified according to submeso activity, showing that ∼1-min one-component stresses are the most frequent when submeso scales are most active. This is generally the case of the decoupled SBL. Figure 2.5a shows the distribution of the three limiting states of anisotropy according to the mean wind speed, in order to explore their relation with the SBL regimes' classification provided by Sun et al. (2012). Each time average is computed from the measurements of a specific sonic anemometer and results from the analysis of data from all sonic anemometers are then collected together. While Stiperski and Calaf (2018) did not find any correlation between anisotropy and the wind speed regime when working with 1-min time averages, our analysis suggests that around a wind speed of $3.5\,\mathrm{ms}^{-1}$ there is a change in turbulence topology, corresponding also to a change in mean flow quantities (Figure 2.5b), which led us to define this value as a threshold wind velocity $\overline{u}_{th}$. Isotropic eddies only occur under low wind speed, and the transition also influences the relative occurrence of one- and two-component axisymmetric eddies. While below the threshold value one-component eddies in each wind speed cluster are more frequent than two-component ones, above the threshold the opposite is true. Most of the one-component eddies (75%) are distributed below the threshold value, while two-component eddies are distributed almost equally in both dynamic regimes (53% below $\overline{u}_{th}$). Looking at the value of the mean wind shear and the Brunt-Vaisala frequency, computed from the measurements of the upper and lower arrays using finite differences and with a reference temperature obtained by averaging over all the instruments at each time step, $S^2 = \frac{(\overline{u}_{up}-\overline{u}_{down})^2}{(\Delta z)^2}$ and $N^2 = \left(\frac{g}{\overline{\theta}}\right)^2 \frac{(\overline{\theta}_{up}-\overline{\theta}_{down})^2}{(\Delta z)^2}$, it is found that the wind speed threshold separates a regime where local stratification slightly increases with $\overline{u}$ and is comparable to the local wind shear (Bulk Richardson number $Ri = N^2/S^2 \sim 1$), to one dominated by the wind shear.

The increase of N^2 and then its sharp decrease above $\overline{u}_{th}$ is an interesting feature. The sharp decrease may be understood as a result of turbulent mixing, generated by shear instability as soon as there is enough kinetic energy in the mean flow. The increase in the low-wind speed regime, instead, seems to be associated with katabatic flows. We observed a similar behaviour for stable cases in other datasets collected over a glacier (not shown), but not in datasets collected over flat terrain. For katabatic flows, indeed, we expect an increase in wind speed with thermal stability (Prandtl, 1942), together with a decrease of the jet maximum height, which in turn increases the wind shear. Recent experimental (Charrondiére et al., 2020; Charrondière et al., 2022) and numerical studies (Brun, 2017) have investigated the anisotropy of the Reynolds stress tensor in katabatic SBL flows over steep slope. They observed a classical turbulent boundary layer below the maximum-wind-speed height, characterised by a logarithmic law profile, slightly corrected to take into account gravity effects. They found different anisotropic properties above and below the jet height, and it would be interesting to relate their results with the behaviour observed in Figure 2.5. However, the lack of tower measurements, to sample the wind speed profiles and eventually isolate katabatic events, doesn't allow this comparison. Looking at the normalized wind speed ($u^+ = \overline{u}/u_* = \overline{u}/(\overline{u'w'}^2 + \overline{v'w'}^2)^{\frac{1}{4}}$) against height in wall units ($z^+ = zu_*/\nu$, ranging in our case between 10^2-10^5 in the low wind speed regime, taking the dynamic viscosity $\mu = 1.725 \times 10^{-5}\,\mathrm{kg\,m^{-1}\,s^{-1}}$) a decreasing trend is observed for individual sonic anemometer (not shown). In presence of katabatic flows, this behaviour should be observed above the jet height (Charrondière et al., 2022, Figure 10a), however without information about the wind speed profile, and analysing all data together, we cannot draw robust conclusions. Analogous results are observed when isolating intervals characterized by one-component stresses at all sonic anemometers simultaneously.

The presence of katabatic flows may lead to an increasing number of wave-like motions, sometimes observed at the top of drainage currents (Princevac et al., 2008; Viana et al., 2010) and generated by the upward motion of air parcels induced by the irruption of the katabatic flow. Thus, the increase of N^2 may be related also to an increase in wave-activity: wave-like motions need a minimum amount of kinetic energy in the mean flow to develop, which is proportional to the mean wind speed, and larger vertical displacements against gravity need larger wind speeds. The increase of N^2 in turn would affect temperature variances, with a larger amount of energy stored into potential energy, as we will see in Section 2.4.3. There might be also other causes to consider in order to explain this behaviour in the low-wind speed regime, and one working hypothesis we would like to investigate more in future studies is the relation with a general increase in submeso activity with wind speed. Submeso motions may lead to strong temperature anomalies affecting the vertical stratification of the atmospheric layer during their passage. For example, warm submesofronts would increase $\Delta\overline{\theta}$ (Pfister et al., 2021, Figure

Table 2.1: Kinetic energy transfers across scale $\Delta \in [1.6\,\mathrm{m}, 3.2\,\mathrm{m}]$, classified according to the state of anisotropy of the Reynolds stress tensor, with a time averaging period of ∼1 min. Anisotropy is computed from the sonic anemometer at the centre of the lower array, see the text for details about this choice. From left to right: percentage of backscatter events, median of the kinetic energy transfer ($\mathrm{m^2s^{-3}}$) during backscatter events, mean of the kinetic energy transfer ($\mathrm{m^2s^{-3}}$) during backscatter and forward transfer events, and percentage of backward energy transfer over the total energy transfer.

Anisotropy state	$\#_{BK}(\%)$	Median(Π_{BK})	$\overline{\Pi_{BK}}$	$\overline{\Pi_{FW}}$	$\frac{\lvert\overline{\Pi_{BK}}\rvert}{\lvert\overline{\Pi_{BK}}\rvert+\overline{\Pi_{FW}}}(\%)$
1 component	34	-0.00023	-0.0065	0.0150	30
2 component	30	-0.00039	-0.0080	0.0217	27
1 component (ND)	32	-0.00023	-0.0102	0.0147	41
2 component (ND)	29	-0.00049	-0.0087	0.0206	30

BK, backscatter; FW, forward transfer; ND, without linear detrending.

5) and they are found to occur preferably for local mean flow with wind speed around $3.5\,\mathrm{ms^{-1}}$ (Pfister et al., 2021).

In the clusters with mean wind speed below $1\,\mathrm{ms^{-1}}$, where stratification and shear are both low, the occurrence of one-component eddies is still not dominant over the other types, but it increases approaching the threshold value, after which it sharply decreases, similarly to the Brunt-Vaisala frequency. In the following sections, we investigate this relation between strong stability and the occurrence of one-component eddies, how it influences the energy transfer in stratified anisotropic turbulence and the occurrence of wave-turbulence interaction.

2.4.2 Inertial kinetic energy transfer across scales

Thermal stratification over the glacier during the SnoHATS campaign reached values up to 8 $^\circ\mathrm{Cm^{-1}}$ (Vercauteren and Klein, 2015), which may lead to the horizontal layering of eddies and constrain the flow to a quasi-2D dynamics. Results obtained by applying the coarse-graining approach described in Section 2.3.2 at scale Δ are shown in Table 2.1 and Figure 2.6. Since the method used to compute the three gradient components evaluates derivatives at the point P2 corresponding to the sonic anemometer at the centre of the lower array, the state of anisotropy of the Reynolds stress tensor is estimated from the measurements taken by this instrument. The backscatter episodes, corresponding to a negative Π^{Δ}, occur more frequently for one-component stresses than for two-component ones, but the mean energy transfer is always towards smaller scales for both limiting states of anisotropy. The same occurs even when one-component states at large wind speed are not considered. These results led us to reject the hypothesis of the development of 2D turbulence, at least at the scale Δ considered. The mean and the median for the backscatter distribution differ by one order of magnitude, thus showing a strongly asymmetric distribution for both one- and two-component eddies. The former transfers a smaller amount of energy across the scale Δ, both up- and down-ward.

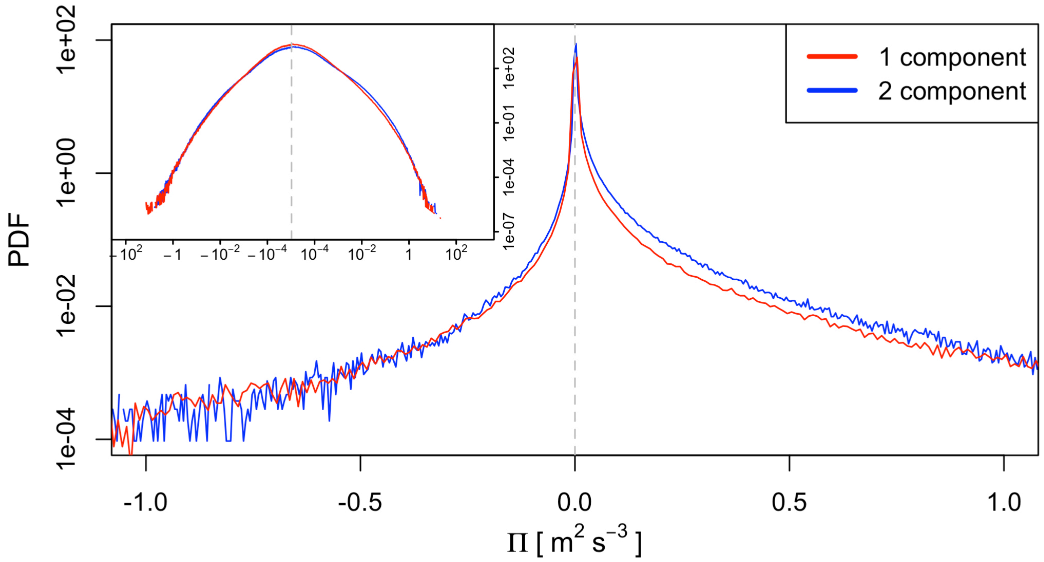

Figure 2.6: Probability density distribution of kinetic energy transfers ($\Pi^\Delta = -\tau_{ij}\widetilde{S_{ij}}$) across scale $\Delta \in [1.6\,\mathrm{m}, 3.2\,\mathrm{m}]$ obtained from the measurements of the arrays of sonic anemometers. Each color corresponds to the probability density distributions computed collecting all ∼1 min periods belonging to the same state of anisotropy of the Reynolds stress tensor. Anisotropy is computed from the sonic anemometer at the centre of the lower array (see the text for details about this choice). The insert plot shows the full range of values of Π^Δ of the two distributions.

For comparison, the analysis was performed also on the non-detrended dataset (Figure 2.3b and Table 2.1). While results for two-component eddies are not significantly affected by this change, results for one-component eddies exhibit appreciable differences. Figure 2.3 already highlighted the increased representation of one-component stresses without detrending. Here, it is worth noting that there is an increase in the mean backscatter for one-component eddies, while the median remains unchanged. The fact that the low-frequency range contributes to the mean backscatter may be attributed to a high correlation between wavelengths in this spectral range, whose interaction leads to backscatter events. It might be argued that, without linearly detrending the data, the fast Fourier transform (FFT) may suffer from red noise (Stull, 1988) and results may not be reliable. However, the mean forward transfer should be affected in the same way, which does not seem to be the case.

Figure 2.6 shows the PDFs of Π^Δ according to one- and two-component Reynolds stresses, and both distributions are non-Gaussian with heavy tails. Tails' asymmetry is large and towards positive values, as expected for a total downward energy transfer, and it is slightly more marked for the two-component cases.

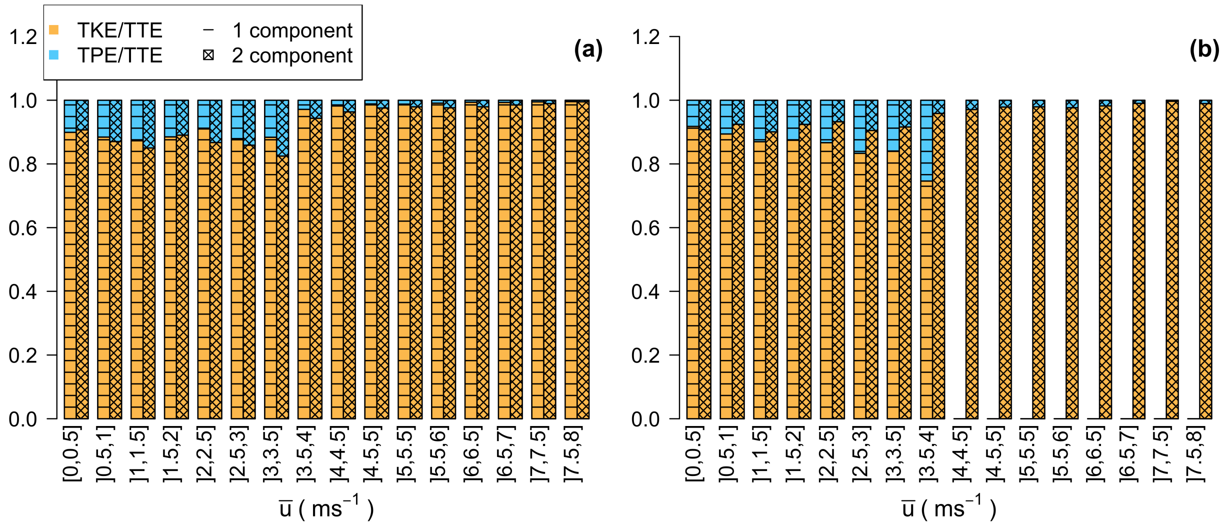

Figure 2.7: Barplots showing the contribution of TPE and TKE to TTE. Each group corresponds to a range of wind speed, and the two bars refer to different limiting states of anisotropy of the Reynolds stress tensor. Panel (a) refers to a time averaging period of ∼1 min, while panel (b) to ∼14 min, and contributions are computed from the medians of TPE and TKE in each cluster.

2.4.3 Partition of energy between TKE and TPE

In strongly stable nighttime conditions, Stiperski and Calaf (2018) found that one-component eddies with 30-min averaging periods generally occur when turbulence destruction by stratification significantly exceeds shear generation in the TKE budget equation. It is now well understood that a negative contribution to the TKE budget due to the buoyancy term may also act as a source term in the TPE budget equation ($\mathrm{TPE} = \frac{1}{2}\left(\frac{g}{\Theta_0 N}\right)^2 \overline{\theta'^2}$) and thus a complete description of turbulence in stably stratified atmosphere has to include both turbulent energies (Zilitinkevich et al., 2007; Ďurán et al., 2018). Sun et al. (2016) hypothesised that it is the dynamic coupling between TKE and TPE through the buoyancy flux that explains the transition observed at a particular wind speed threshold in the SBL, as at low wind speed the increase of TKE is limited by the energy consumption for increasing TPE, but at high wind speed this mechanism does not occur anymore, leading to a dramatic increase of TKE with wind speed. Motivated by the results of Stiperski and Calaf (2018), we therefore investigated if this dynamic coupling also implies a particular state of anisotropy of the Reynolds stress tensor.

The TKE and temperature variance budget equation for a horizontally homogeneous atmosphere, neglecting subsidence, are as follows:

$$\begin{aligned}\frac{\partial \overline{k}}{\partial t} &= \frac{g}{\overline{\theta}_v}\overline{w'\theta'} - \overline{u'w'}\frac{\partial \overline{u}}{\partial z} - \overline{v'w'}\frac{\partial \overline{v}}{\partial z} - \frac{\partial \overline{w'k}}{\partial z} - \frac{1}{\overline{\rho}}\frac{\partial \overline{w'p'}}{\partial z} - \epsilon \\ \frac{1}{2}\frac{\partial \overline{\theta'^2}}{\partial t} &= -\overline{w'\theta'}\frac{\partial \overline{\theta}}{\partial z} - \frac{1}{2}\frac{\partial \overline{w'\theta'^2}}{\partial z} - \epsilon_\theta\end{aligned} \tag{2.7}$$

where it can be noted (in red) that a negative heat flux in stable stratification contributes to decrease the TKE and at the same time to increase the potential temperature variance, thus converting part of the TKE into TPE (proportional to the potential temperature variance). A larger potential temperature variance in turns has a larger positive contribution to the heat flux budget equation, thus implying a weakening of the total negative value of the heat flux in stable stratification:

$$\frac{\partial \overline{w'\theta'}}{\partial t} = -\overline{w'}^2 \frac{\partial \bar{\theta}}{\partial z} - \frac{\partial \overline{\theta' w' w'}}{\partial z} + g \frac{\overline{\theta'^2}}{\bar{\theta}} - \frac{1}{\bar{\rho}} \left[\frac{\partial \overline{p'\theta'}}{\partial z} - \overline{p' \frac{\partial \theta'}{\partial z}} \right] - \epsilon_z \tag{2.8}$$

A smaller negative heat flux thus leads to a reestablishment of TKE by a counter-gradient mechanism, which should be included in the parameterization of the heat flux, such as $\overline{w'\theta'} = K_\theta \overline{\theta'^2} - K_{Heat} \frac{\partial \bar{\theta}}{\partial z}$.

TPE and TKE were computed for each sonic anemometer and then collected together, according to the state of anisotropy of the Reynolds stress tensor. Contributions of TKE and TPE to the total turbulence energy (TTE), defined as TTE = TKE + TPE, are shown in Figure 2.7a according to the wind speed, for one- and two-component eddies using ∼1 min time windows. As expected, the low wind speed regime is characterised by a higher contribution of TPE with respect to the high wind speed regime, but the two limiting states are comparable, with the TKE contribution being much larger than the TPE one. It is worth noting that the percentage of TPE never exceeds 20%, as was also shown in Kurbatskii and Kurbatskaya (2012, Figure 3) from numerical simulations performed with a RANS model including balance equations for the viscous dissipation ϵ, TKE and TPE. These results are in agreement with the Energy and Flux Budget (EFB) turbulence closure in a stably stratified sheared flow (Zilitinkevich et al., 2007), where the TPE is parameterised as a function of the flux Richardson number (R_f): TPE = TTE $\cdot$ R_f. Since R_f reaches a maximum asymptotic value of 0.20 - 0.25 increasing the thermal stability of the mean flow, the EFB theory predicts that the TPE growth is also limited, as validated by LES data and measurements in the laboratory and in the atmosphere (Zilitinkevich et al., 2008, Figure1).

Extensions of the EFB theory (Zilitinkevich et al., 2009; Kleeorin et al., 2019) showed that the maximum R_f is no longer a universal constant when the contribution of large-scale IGWs is taken into account, but it increases with wave activity, and so does the TPE (Zilitinkevich et al., 2009, Figure 5) for vertically homogeneous stratification (Zilitinkevich et al., 2009, Figure 1). We thus look at longer time windows of ∼14-min, in order to include part of the wave contribution to eddy energetics and seek for possible significant differences between one-component and two-component states. Figure 2.7b shows that in this case the wind speed threshold is sharp and one-component periods only occur for low wind speed. At this scale, the contribution of TPE to TTE for one-component periods slightly increases approaching the wind speed threshold, and it is generally larger than the TPE contribution for the two-component periods. This may be explained by the additional production of TPE by IGWs, thus supporting the hypothesis that one-component Reynolds stress tensors may occur more frequently when there are IGWs. Nevertheless, the maximum percentage of TPE contribution to TTE is

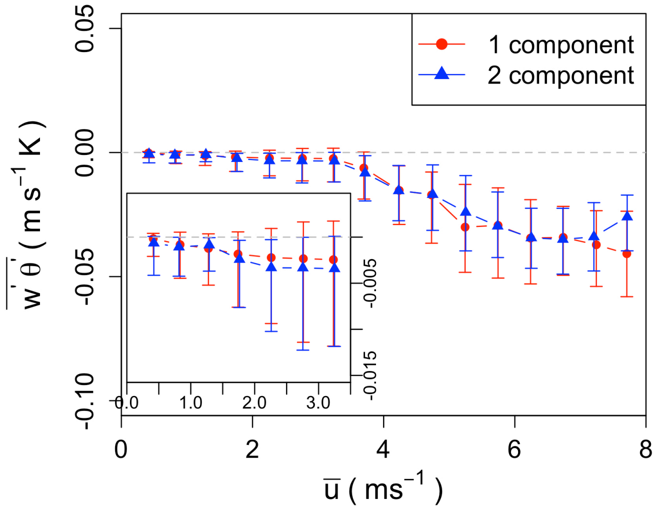

Figure 2.8: Dependence of the heat flux on the mean wind speed, with a time averaging period of ∼1 min. Data from individual sonic anemometers are analysed separately and then binned together. Points correspond to the median for each range of wind speed, with the bar showing the interquartile range (Q_1,Q_3). The inner plot is a zoom in the low wind speed regime.

still below 25% for every wind speed, which may depend on a low kinetic energy of the wave that can be converted to TPE (Zilitinkevich et al., 2009) or to the close distance to the surface and a dominant contribution of TKE production by the mean shear. In fact, it has been shown by numerical simulations that the TPE contribution increases with height (Maroneze et al., 2019b, Figure 8) and reaches values as high as 90% of TTE for shear-free stably stratified flows (Kleeorin et al., 2019, Figure11).

As the heat flux plays an essential role in driving SBL regime transitions (Maroneze et al., 2019b), we also checked its dependence on the wind speed, as shown in Figure 2.8 for one- and two-component ∼1 min Reynolds stresses. While there is no significant difference in the overall behaviour for the two limiting states of anisotropy, the interquartile range (Q_1,Q_3) of one-component stresses shows that positive heat fluxes may occur below the wind speed threshold, which is not the case for two-component stresses. The temperature gradient is positive for all the considered cases, thus a positive flux implies a counter-gradient contribution. In very stable conditions with weak vertical velocity-variance, positive heat fluxes may happen because of the dominant contribution of the temperature variance term in the heat flux budget equation, which is always positive and may be driven also by horizontal temperature gradients. Since TPE is proportional to this term, the dominant mechanism in one-component stresses with counter-gradient heat fluxes is the conversion of TPE into TKE and not viceversa, because positive heat fluxes will contribute as a source term in the TKE budget equation and a sink term in the budget equation for temperature variance. In the literature, counter-gradient heat fluxes have been observed for waves strongly interacting with turbulence (Einaudi and Finnigan, 1993; Sun et al., 2015a). Vercauteren et al. (2019a, Figure 8) showed that counter-gradient heat fluxes in the SBL occur more frequently with one-component

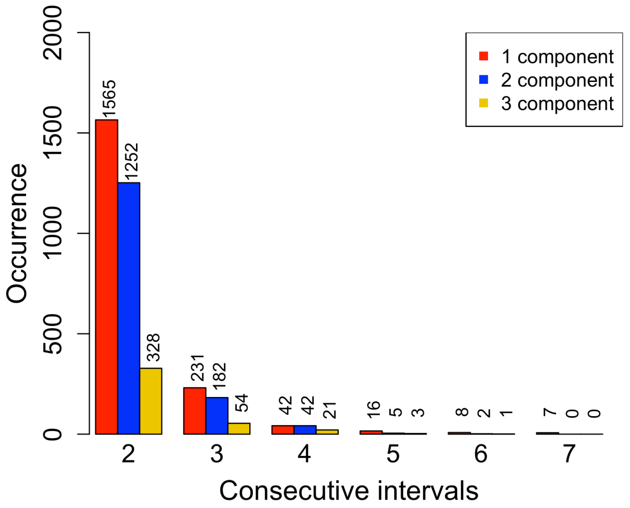

Figure 2.9: Barplot showing the occurrence of periods including consecutive intervals ($\sim$ 1 min time average) with the same state of anisotropy of the Reynolds stress tensor. Each group corresponds to a number of consecutive intervals, and there are no periods including more than 7 consecutive intervals with the same state of anisotropy. Data from individual sonic anemometers are analysed separately and then collected together.

turbulence, even if they are not always present, concluding that it is not possible to uniquely relate one-component states to counter-gradient heat fluxes, and thus waves. Analogous results are observed here, as the averaged heat flux for all one-component periods is still negative, but with possibility of counter-gradient episodes for low wind speed.

The separation of internal waves from turbulence is still a vexing problem, and generally a fixed time averaging period is adopted in eddy-covariance analysis. This fixed period might directly include contributions from waves in some cases, while not in others, for example depending on thermal stratification, which influences the period of IGWs. Waves can produce large errors in sign and magnitude of the computed turbulent fluxes, and waves of different periods impact the turbulence statistics and flux calculations differently (Durden et al., 2013; Cava et al., 2015). Since only wave time-scales are characterised by counter-gradient heat fluxes, our results and those from Vercauteren et al. (2019a) might also be interpreted as: 1-min periods with counter-gradient heat fluxes are mostly including wave contribution in turbulent statistics, and 1-min one-component periods may or may not include this contribution, thus not all one-component periods have a counter-gradient heat flux. Nevertheless, it is still possible that IGWs influence the anisotropy of the Reynolds stress tensor at smaller scales (as in the case of wave flume experiments), even if their contribution is not directly included in turbulent statistics, thus relating all one-component periods to waves. Therefore, we proceed in the analysis by further exploring this possibility and working on longer periods of data, classified according to the anisotropy of shorter periods.

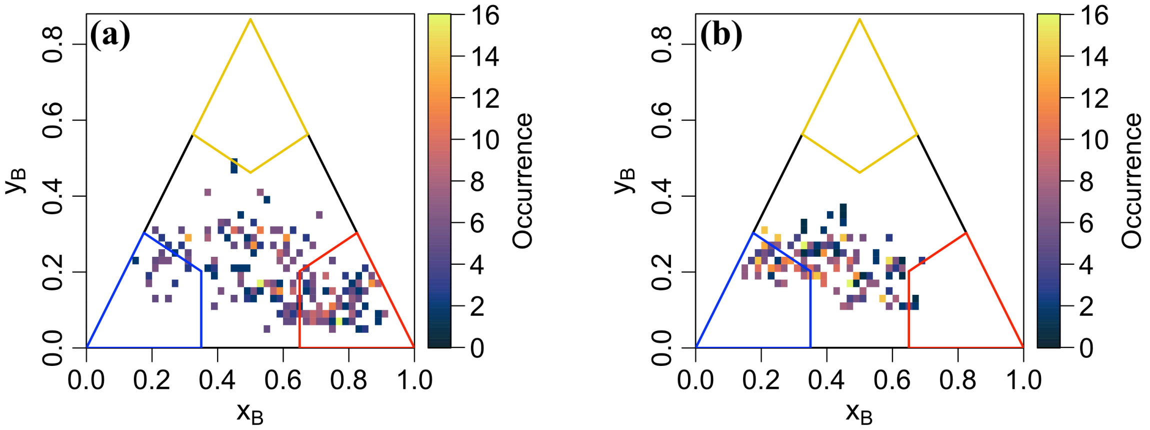

Figure 2.10: Barycentric maps with the occurrence of all short periods of $\sim$ 1 min, included in the 14-min periods used in the cross spectral analysis. One (two)-component periods include at least eight ~1-min Reynolds stresses in the one (two)-component state. Panel (a) shows the barycentric map for the 50 one-component periods, and panel (b) shows the barycentric map for the 39 two-component periods.

2.4.4 Linear IGWs and 1-min Reynolds stress tensor

Typical periods of IGWs in the SBL range from 1 to about 10 min (Rees et al., 2001; Sun et al., 2004; Durden et al., 2013; Cava et al., 2015; Zaitseva et al., 2018). In order to study the influence of IGWs on the anisotropy of turbulence, we selected data-windows of about 14 min (2^{14} data points), so that the cross-spectral analysis covers the whole range of typical IGW frequencies. The resolved bandwidth then spans from 0.0013 Hz to 10 Hz. Only continuous periods of data were used to select the windows, thus reducing the equivalent of 14×24 hours of data to 8×24 hours. Each window includes 16 short-time averages of 2^{10} data points ($\sim$ 1 min time average), which are linearly detrended before computing the Reynolds stress tensor, used to classify periods according to the state of anisotropy. As there are no 16 consecutive 1-min averages with the same type of anisotropy, a criterion to label periods as one- or two-component had to be chosen. Figure 2.9 in fact shows that over all the selected data from all the sonic anemometers there are at most 7 consecutive 1-min windows whose anisotropy is classified as one-component limit and 6 for the two-component limit. Turbulence in the same limiting state generally persists for only two consecutive 1-min periods, then the occurrence sharply decreases for more consecutive intervals. We thus chose to label a 14-min period as one- or two-component if at least 50% of the included 1-min time averages belongs to that particular state of anisotropy. This was a compromise between having enough periods to perform ensemble averages for the cross spectral analysis and having enough short time averages to properly associate a period with a well defined 1-min anisotropy. The method selects a total of 34 one-component 14-min periods for the lower array and 16 for the upper array, including mostly low-wind speed one-component ($\sim$ 80%, not shown). For the two-component periods, there is a big difference in the amount of 14-min periods selected for the two arrays, with just 3 periods for the upper array, while 36

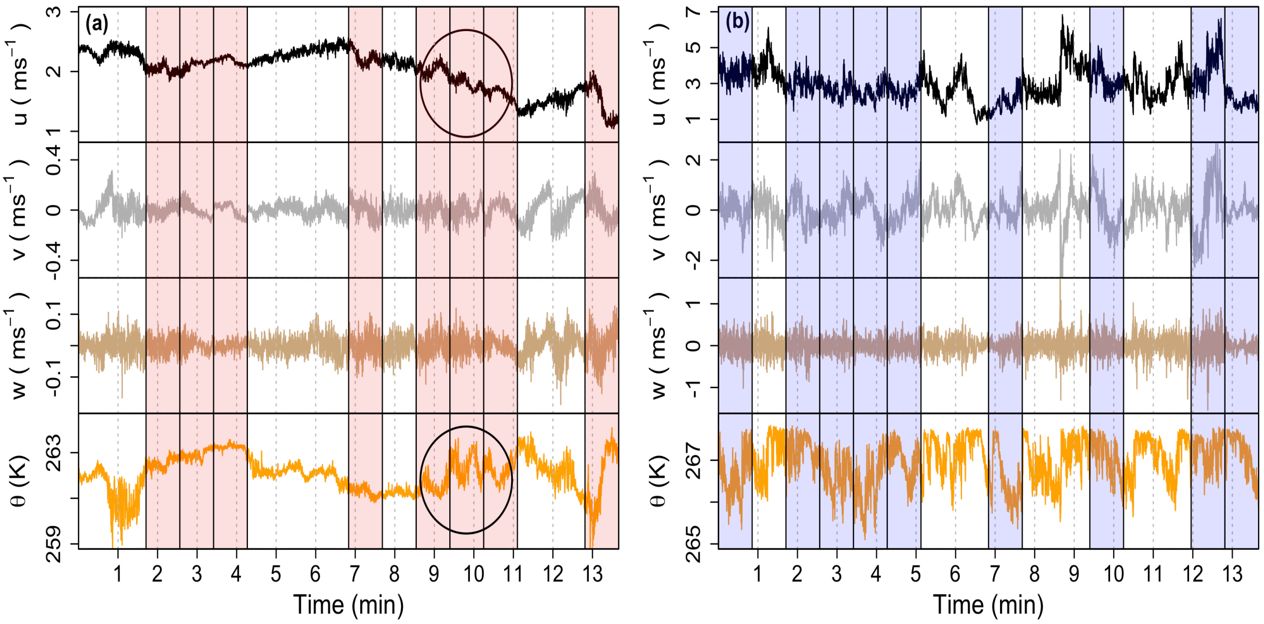

Figure 2.11: Wind speed (double-rotated) and temperature time series extracted from the measurements of the central sonic anemometer in the bottom array. Panel (a) shows the time series for a period classified as one-component, 2006-02-04 from 00:57:38 to 01:11:24. Panel (b) shows the time series for a period classified as two-component, 2006-04-17 from 02:51:14 to 03:05:10. The red (blue) background color identifies the 1-min time windows classified as one- (two-) component.

for the lower one. This is in agreement with the increasing occurrence of two-component periods presented in Figure 2.4 at larger time-windows and explained by a stronger interaction of eddies with the ground. In fact, it is expected that at a fixed time scale, as done here, eddies closer to the surface interact more with the ground than eddies at higher levels, thus leading to a larger number of periods in the two-component edge. The barycentric map of the 1-min anisotropy for the selected 14-min periods is shown in Figure 2.10. The spread of the one-component distribution (characterised by 800 short windows) is much larger than for the two-component distribution (characterised by 624 short windows) and the anisotropy of turbulence is closer to the limiting state. The example of a period selected by the method is shown in Figure 2.11, where Figure 2.11a (Figure 2.11b) shows the wind speed and temperature time series for a period classified as one- (two-) component, with the red (blue) background color identifying the short time averages with that type of anisotropy.

In Figure 2.11a a wavelike pattern, highlighted by an ellipse, can be recognised from minute 9 to 11 in the temperature time series, with a wave period shorter than the averaging time window used to compute turbulent stresses. Similar patterns are not easily identified by visual inspection in the two-component case in Figure 2.11b.

Following the cross spectral method explained in Section 2.3.3, we computed the median cospectra and quadrature spectra for the 50 one-component and 39 two-component periods, with the former shown in Figure 2.12a. Frequencies are normalized by the mean wind speed, according to Taylor's hypothesis, and are made dimensionless with measure-

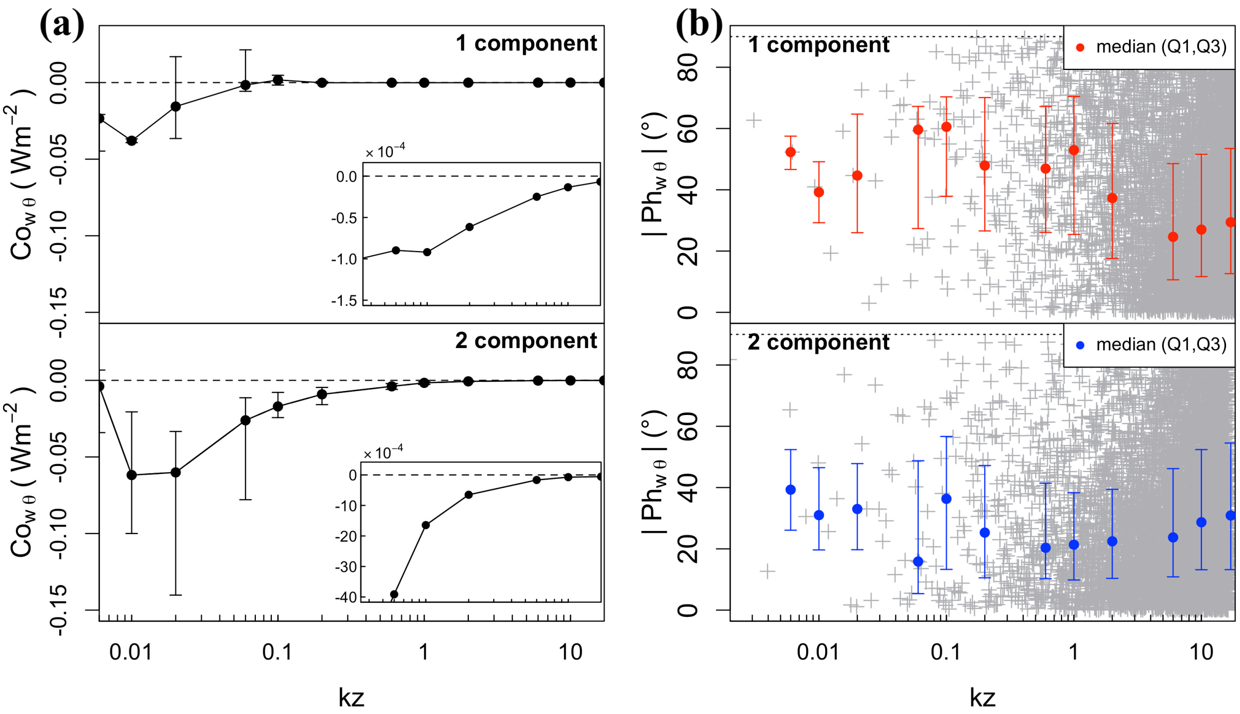

Figure 2.12: Cross spectral analysis of vertical velocity and temperature for 14-min periods, with one (two)-component periods including at least eight ∼ 1-min Reynolds stresses in the one (two)-component state. Panel (a) shows the median per bin of normalised frequencies of the median cospectrum over all the individual 14-min periods (50 one-component periods and 39 two-component periods) and the corresponding interquartile range (Q_1,Q_3), with the insert plot zooming into the high frequency range. Panel (b) shows the corresponding phase spectrum in absolute value and the interquartile range (Q_1,Q_3), with individual data points shown in grey.

ment height. At each scale, both one- and two-component periods contribute negatively to the heat flux, but two-component periods have larger negative values because eddies of this type are characterised by larger wind speed (Figure 2.5a), leading to stronger turbulence production. The corresponding phase spectra with the interquartile range (Q_1, Q_3) are shown in Figure 2.12b in absolute value. For IGWs a ±90° phase angle is expected at the wave frequency. One-component periods, which we hypothesised to be more influenced by IGWs, show a tendency towards larger absolute phase shifts at large scales. The fact that there is not exactly a tendency towards 90° might be due to the analysis considering all one-component periods together, without a further classification. Waves of different frequencies or not pure linear waves and contributions from other types of submeso motions are hence considered together, thus smoothing out the phase signal when the median is taken. Nevertheless, a clearly distinct behaviour can be recognized according to anisotropy, with the two-component periods having smaller phase shifts with respect to the one-component ones at larger scales. Instead, they have a similar behaviour at the smallest scales where the effect of IGWs is not expected to be important. There is thus evidence that periods characterised by one-component anisotropy at smaller scales may be related to IGWs at larger scales. To further inves-

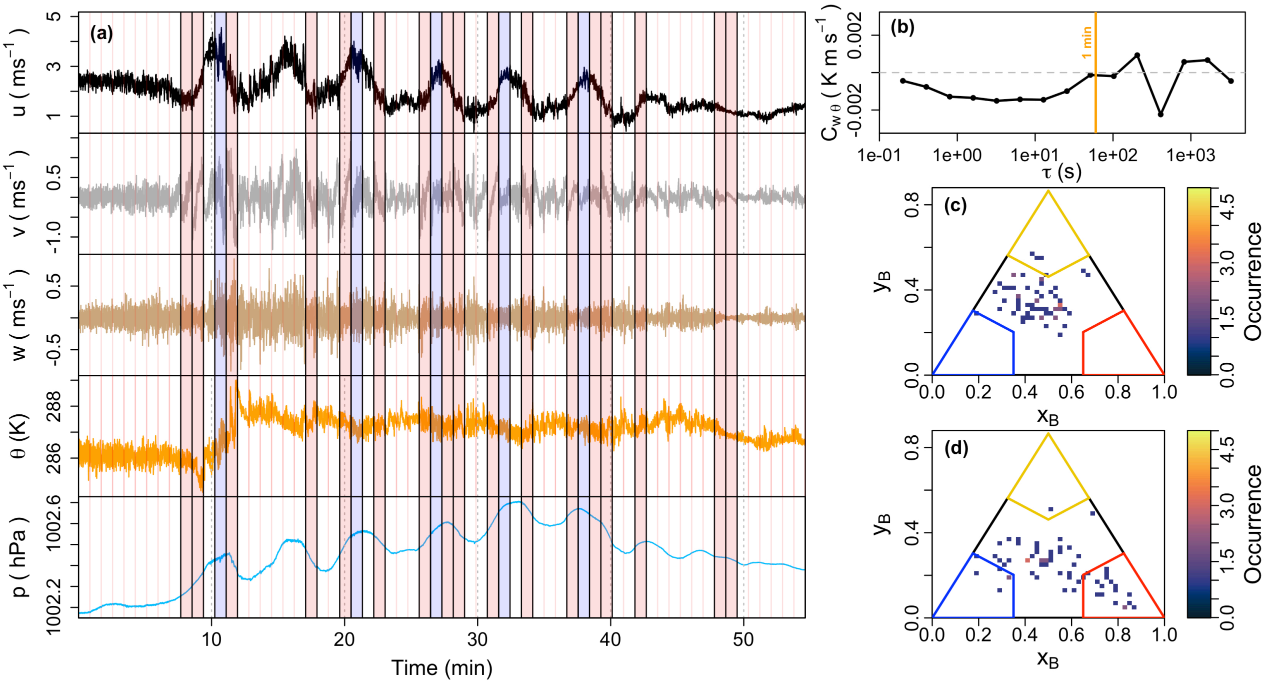

Figure 2.13: Analysis of a wave observed in Dumosa, Australia. Panel (a) shows the wind speed (double-rotated), temperature and pressure time series, with red lines delimiting each time window. The red (blue) background color identifies the 1-min time windows classified as one- (two-) component. Panel (b) shows the heat flux MRD cospectrum, while panel (c) and panel (d) show the corresponding barycentric maps with the occurrence of Reynolds stresses, computed applying (c) or not (d) a linear detrending procedure to individual periods.

tigate this relationship we proceed in the next section with a complementary analysis: given a detected wave, what is the corresponding anisotropy of the Reynolds stress tensor at small scales?

2.4.5 Anisotropy analysis of a clean wave

In order to answer the question above, we need observations of a wave whose characteristics are as close as possible to ideal conditions. These are found for waves with oscillations of approximately constant amplitude and period, also referred to as clean waves (Sun et al., 2015a). Clean waves are uncommon and were not detected in the SnoHATS campaign, thus only for this analysis we use a different dataset from a field campaign over a flat site in Dumosa (−35.868304°S, 143.343323°E), Australia (Lang et al., 2018; Mahrt et al., 2021). Figure 2.13a shows the time series of wind speed, temperature and pressure in a window selected from measurements at 3 m a.g.l. collected by a sonic anemometer at a frequency of 10 Hz. The MRD technique is used to determine the appropriate averaging period for the anisotropy analysis of turbulent scales (see Appendix A for details) and, as shown in Figure 2.13b, the cospectral gap is found around 1-min and thus 2^9 data windows are selected (marked by red lines in Figure 2.13a). The double-rotation method is applied to data, as done for the previous analyses. A wave with a period of around 6 min (~ 0.003 Hz) is observed for half an hour during the night between 15:57 UTC and 16:33 UTC and consists of few cycles with decreasing amplitude. The wave period corresponds well to the second peak observed in the MRD cospectrum at $\tau = 409$ s, thus showing that even this clean wave is not purely monochromatic, as most waves encountered in the atmosphere, and therefore the total wave-heat flux could be different from the zero value prescribed by the linear wave theory. The observed wave seems to be generated by the passage of a microfront, as the temperature time-series exhibits a sharp increase of about 2 K in 3 min, characterised also by small quasi-periodic fluctuations. This is an interesting feature, as it corroborates the hypothesis previously presented in Section 2.4.1 that the increase of atmospheric stability with mean wind speed in the decoupled SBL may be related to microfronts, which, as shown here, can in turn imply wave activity. The barycentric coordinates (Eq. 2.2) of the full window (2^{15} data) are close to the one-component limit with $(x_B, y_B) = (0.89, 0.02)$, and the same occurs if the interval is decreased to $\sim$ 7-min (closer to the period of the observed wave), with 6 out of 8 windows falling in the one-component edge (not shown). One-component states are observed throughout the wave event when the interval is further decreased to $\sim$ 1-min, except at the wave peaks, where two-component states occur due to the enhancement of the wind shear by the wave itself, as shown in Figure 2.13a by the red and blue strips, respectively.

It follows that a wave contributes to drive the Reynolds stress tensor towards the one-component limit in two ways: if many (or at least one) wave cycles are included in the time interval or if just the fraction of the wave cycle corresponding to the trend in the time series is included. The latter contribution can be a priori removed in those turbulence studies interested to limit the effects of low-frequency (submeso) contributions to turbulence statistics. Figure 2.13c, indeed, shows that a linear detrending method is sufficient to move the one-component Reynolds stress tensors towards the centre of the barycentric map. However, this method is effective on waves with periods larger than the averaging interval, while all the others will still contribute to drive the Reynolds stress tensor towards the one-component limit. The wavelike pattern identified in the time series in Figure 2.11a shows exactly that, with windows labelled as one-component during the passage of a wave with a period shorter than $\sim$ 1 min. From this wave analysis, it follows that Reynolds stresses towards the one-component limit may include non-turbulent contributions from waves, which should be considered as spurious contribution if we are only interested in turbulence characteristics.

2.5 Conclusions

The study presented in this chapter examined the shape of the Reynolds stress tensor in the SBL. The SnoHATS dataset, collected over a glacier at the height of about 2 m a.g.l, was used for the analysis, and the frequent occurrence of one-component states under strongly stably stratified conditions was investigated, in relation with two hypotheses. One is that strong temperature stratification may enable the development of quasi-2D dynamics, as suggested by the formation of horizontal layers observed in stratified turbulent flow, and thus leads to 2D turbulence, characterised by an inverse energy cascade. The other hypothesis is that internal gravity waves, ubiquitous in the SBL, may influence the shape of the Reynolds stress tensor at small scale, contributing to the one-component cases, and may lead to a different distribution of turbulent energy into kinetic and potential energy.

Vercauteren et al. (2019a) already observed frequent occurrence of one-component Reynoldsâs stresses in the SBL and attributed it to a non-stationary interaction between submeso motions and turbulence scales. Our findings suggest that these non-stationary forcings may introduce trends in the time window used to compute turbulence (1-min is mainly adopted in the present study), and that those trends lead the small scale contribution to the Reynolds stress tensor towards one-component limit. Nevertheless, after linear trend removal, we found that one-component states still dominate the low-wind speed regime, characterised by strong stratification. The three limiting states of anisotropy (isotropic, two-component and one-component) show a clear relation to wind speed, suggesting a wind speed threshold, $\overline{u_{th}}$, of about $3.5\,\mathrm{ms}^{-1}$. Isotropic and one-component states occur almost exclusively below $\overline{u_{th}}$, while larger wind speeds are mainly connected with two-component states. The latter start to become more frequent than one-component states when the threshold wind speed is crossed, and dominate the high wind speed regime especially if time averages larger than 1-min are adopted. The change in turbulence topology between two-component and isotropic/one-component states is found to be related to a change in the relative contribution of local static stability and wind shear. While larger wind speed implies larger wind shear close to the surface, this does not lead to an increasing occurrence of isotropic turbulence. This seems related to the fact that shear-generated turbulent eddies at large wind speed are coupled with the surface, and the straining effect due to shear leads energy to be distributed along two dominant directions. At low wind speed, instead, isotropic eddies may be produced by localised weak shears, related to submeso activity, and they are decoupled from the surface, with turbulent kinetic energy distributed more uniformly in three directions. This interpretation is in agreement with Vercauteren et al. (2019a), where the proportion of isotropic stresses was found to increase with distance above the ground, while that of two-component was found to decrease (their Figure 7).

By quantifying the energy exchange between large and small scales, our findings do not support the hypothesis that one-component turbulence is related to 2D turbulence. The backward mean kinetic energy transfer was always smaller than the forward energy transfer, about half of it at the scale $\Delta = 3.2\,\mathrm{m}$ considered. Analogous results were obtained for two-component cases, with no significant difference in the energy exchange across scales between these two types of anisotropic stresses.

On the other hand, our results show that waves play an important role in modulating anisotropy at small time averages towards the one-component limit. Investigation of 14-min periods with dominant 1-min one-component and 1-min two-component states showed that the phase shifts between temperature and vertical velocity in the low frequency range were larger (close to 60°) for one-component than two-component spectra. At larger scales, a possible wave signature was also found in 14-min Reynolds stress tensors towards the one-component limit at low-wind speed, as they were characterised by an increasing contribution of potential energy to the total energy of the fluctuations, following the behaviour of local stability. Further evidences for the role of waves in one-component turbulence was obtained by analysing a clean wave signal measured at 3 m a.g.l in Dumosa (Australia). The Reynolds stress tensor of a complete wave cycle has a one-component signature, as well as the Reynolds stress tensor of an approximately linear trend caused by sampling only a fraction of the wave cycle. A wavelet representation based on MRD for heat fluxes does not remove such trends, thus the turbulence time scale estimated from MRD cospectra may include non-turbulent contributions to the Reynolds stress tensor. For those SBL studies interested to limit the effect of submeso motions on turbulence statistics, such contributions are spurious and we recommend to apply the MRD technique together with a linear detrending procedure. The influence of trends is a specific case supporting the general understanding that non-stationary interaction between submeso motions and turbulence scales may drive one-component Reynolds stress tensors. It also suggests that the existence of trends in measured velocity-variances leads to one-component Reynolds stress tensors, because turbulent kinetic energy is mainly distributed along the direction of the submeso forcing. However, a key point in tensor analysis of anisotropy is that the off-diagonal terms of the Reynolds stress tensor matter, which is why a direct link between measured velocity-variances (dependent on the coordinate system) and component-energies (eigenvalues, independent of the coordinate system) is not straightforward, unless the measured Reynolds stress tensor is almost diagonal. In this specific case, the coordinate system used would coincide with the principal component coordinate system. This is not usually the case, and the observed one-component stresses seem to be also characterised by large $\overline{u'v'}$ (Stiperski et al., 2021, Figure S1a, Supplemental Material). It would be interesting for a future study to extract different types of submeso motions (Kang et al., 2014, 2015; Vercauteren et al., 2019b) and analyse their contribution to the anisotropy of the Reynolds stress tensor. For example, it is known that meandering motions may lead to tendencies in the spanwise and streamwise velocity-variance, but their specific contribution to anisotropy still has to be explored.

Our results thus support the idea that, for improving turbulence modeling in the decoupled regime of the SBL, a necessary step is to include wave forcing. A promising technique is to combine recent approaches based on potential/kinetic energy conversion processes and on the anisotropy of the Reynolds stress tensor.

Chapter 3

Numerical modeling of a valley-exit wind and sensitivity analysis to PBL schemes in the WRF model

3.1 Introduction

Atmospheric circulations over mountainous regions are much more complex than over flat terrain, due to the interaction between the flows and the orography at different spatial and temporal scales (Lehner and Rotach, 2018). Almost 50% of the Earth's land surface is covered by hilly and mountainous terrain (Meybeck et al., 2001), and the understanding of the atmospheric circulation over complex terrain is an important issue for many sectors, including weather forecasting, pollutant dispersion and renewable energy sources assessment.

Under fair weather conditions, different types of thermally-driven circulations typically develop over mountain regions (Zardi and Whiteman, 2013), driven by pressure gradients produced by differential heating of the atmosphere in adjacent areas. In particular, mountain valleys are affected by the development of cross- and along-valley circulations, generally called slope and valley winds respectively. Up-slope and up-valley winds typically blow during daytime, while down-slope and down-valley winds are present during the night (Whiteman, 1990; Rucker et al., 2008; Schmidli et al., 2009; Giovannini et al., 2017). Common features of these circulations include a wind reversal twice per day, driven by the diurnal temperature cycle, but local features depend on the valley landforms and cannot be generalized from one valley to the other. For example, along-valley variations such as local constrictions may induce a local flow acceleration to ensure mass conservation (Pamperin and Stilke, 1985), or local topographic curvatures (Weigel and Rotach, 2004) and tributary valleys may alter the main flow structure (O'Steen, 2000).

When the surface energy budget results in radiative loss, the near-surface atmospheric layer becomes stably stratified, reducing vertical motion and turbulent mixing. These situations are prone to the accumulation of pollutants close to the surface, with a continuous increase of their concentrations. Thermally-driven down-valley and down-slope flows are a key factor in these conditions. They strongly influence mixing processes in the Planetary Boundary Layer (PBL) (Steyn et al., 2013; Sabatier et al., 2020; Giovannini et al., 2020), such as with the formation of ventilation zones at the valley exit (Quimbayo-Duarte et al., 2019), as well as contribute, through convergence from tributary valleys and sidewalls, to strengthen the stratification of the valley atmosphere, with the development of strong thermal inversions and cold-air pool (CAP) episodes (De Wekker and Whiteman, 2006). CAPs consist of a topographically confined, stagnant layer of air close to the surface colder than the atmosphere above (Whiteman et al., 2001). Two types of CAP may be defined: a diurnal one, which forms during the evening/night and decays after sunrise of the next day, and a persistent one, which can last for several consecutive days. There is a mutual interaction between the local airflow and the CAP. Convergence of down-slope flows contributes to increasing the depth of the CAP until the down-valley flow is fully developed. Once a CAP has formed, it may in turn influence the local circulation. A deep stable layer, in fact, may behave as a material surface (sometime referred as *effective mountain*) to the airstream impinging on it, as shown by observations and numerical simulations (Neff and King, 1987, 1989; Lin et al., 2005; Reeves and Lin, 2006). Drainage flows during nighttime may experience an upward forcing as they merge with the cold air inside the main valley and sometimes sharp front-like features are observed between the two air masses (Muoz et al., 2020, Figure 16). Numerical simulations have shown that downslope winds may split when they reach the cold air accumulated inside a basin, partly flowing close to the surface and partly above the CAP (Cuxart et al., 2007, Figure 7a). Similar results are obtained in idealized simulations of katabatic flows over a moderate slope, and towards an ice shelf, where a secondary elevated peak in wind speed is observed once the two air masses meet (Renfrew, 2004, Figure 8).

In this context, the present chapter focuses on the reproduction of a local drainage current in the basin of Bolzano (Italian Alps) and on its interaction with the CAP developing during wintertime in this area. This drainage flow presents characteristics similar to the valley-exit jets, which typically develop at the exit of narrow valleys into a wider area or of a canyon-like valley into a plain. Valley-exit jets have been documented at various locations around the world (Pamperin and Stilke, 1985; Banta and Gannon, 1995; Chrust et al., 2013; Jiménez et al., 2019). It is primarily a thermally-driven phenomenon, but it may exhibit aspects in common with gap winds (Chrust et al., 2013). Gap winds develop when airflows approach a topographic width constriction in the form of a channel, a corridor, a narrow pass, or a mountain gap. Differences in the characteristics of the air masses between the two sides of the gap can force air parcels to accelerate along the pass, reaching the highest velocities at the exit (Zängl, 2004) or further downstream (Jiménez et al., 2019). Enhanced horizontal pressure gradients occur near the exit of the valley (Whiteman, 1990), further accelerating the flow. When the increase in kinetic energy, related to the acceleration of the flow, is compensated by a decrease in potential energy, the flow is constrained to a forced descent, and a slow and deep flow turns into a fast and shallow one. This dynamic mechanism, for example, was observed at the exit of the Inn Valley (Zängl, 2004), where the flow reached the maximum intensity ($15\,\mathrm{m\,s^{-1}}$ at a height of 200 m AGL) close to sunrise, and the acceleration was interpreted as a transition from subcritical to supercritical hydraulic flow. A subcritical state was not restored farther downstream through a hydraulic jump, and a possible explanation was the lower potential temperature of the flow exiting the Inn Valley with respect to the surrounding air in the Bavarian plain.

In the present chapter, the valley-exit wind in the Bolzano basin is reproduced in two different atmospheric conditions through numerical simulations with the Weather Research and Forecasting (WRF) model, evaluating the performance of four PBL schemes. Meteorological data from the Bolzano Tracer EXperiment (BTEX), collected in January and February 2017 (Tomasi et al., 2019; Falocchi et al., 2020; Zardi et al., 2021), providing both surface measurements and vertical profiles of temperature and wind speed and direction, are used for model validation. Then, results from the numerical model are also used, together with observations, to get an insight on the spatial structure of the valley-exit wind and obtain a more complete view of its interaction with the air in the Bolzano basin, focusing on the influence of the atmospheric stratification in the basin. For this analysis, one simulation for each case study is adopted.

The chapter is organised as follows: Section 3.2 describes the area of interest and the two case studies, together with the BTEX experiment and the measurements used to validate the model. Section 3.3 focuses on the setup and initialization of the subkilometer numerical simulations, identifying the main variables to pay attention to when initializing high-resolution numerical simulations over complex terrain. Results from the numerical simulations are presented in Section 3.4, with a qualitative as well as quantitative evaluation of the performance of the simulations with the different PBL schemes. Section 3.4.3 mainly focuses on the evaluation of the interaction between the valley-exit wind and the air in the Bolzano basin. Finally, conclusions are drawn in Section 3.5, together with a discussion on the influence of low-level jets (LLJs), such as valley-exit jets, on turbulence characteristics in the SBL, with a particular focus on turbulence anisotropy.

3.2 Area of interest and observations

3.2.1 The area of Bolzano

The city of Bolzano (258 m a.s.l.) lies where the Adige Valley, in the northeastern Italian Alps, widens into a nearly basin-like area with two tributary valleys: the Sarentino Valley from North and the Isarco Valley from East. Mountain peaks surrounding the basin range between 1200 m and 2000 m a.s.l. (Figure 3.1). The Isarco Valley is a V-shaped valley, with a very narrow valley floor close to its exit onto the Bolzano area and a dominant southwest-northeast orientation, although it includes several bends along its length of about 80 km. In winter, during nighttime, ground-based temperature inversions frequently occur in the Bolzano area under weak synoptic forcing and clear sky conditions. They start to develop in the late afternoon and end some hours after sunrise, when the energy input from solar radiation is sufficient to break up the inversion layer. However, in winter, due to the weak solar radiation and the sky-view factor reduced by

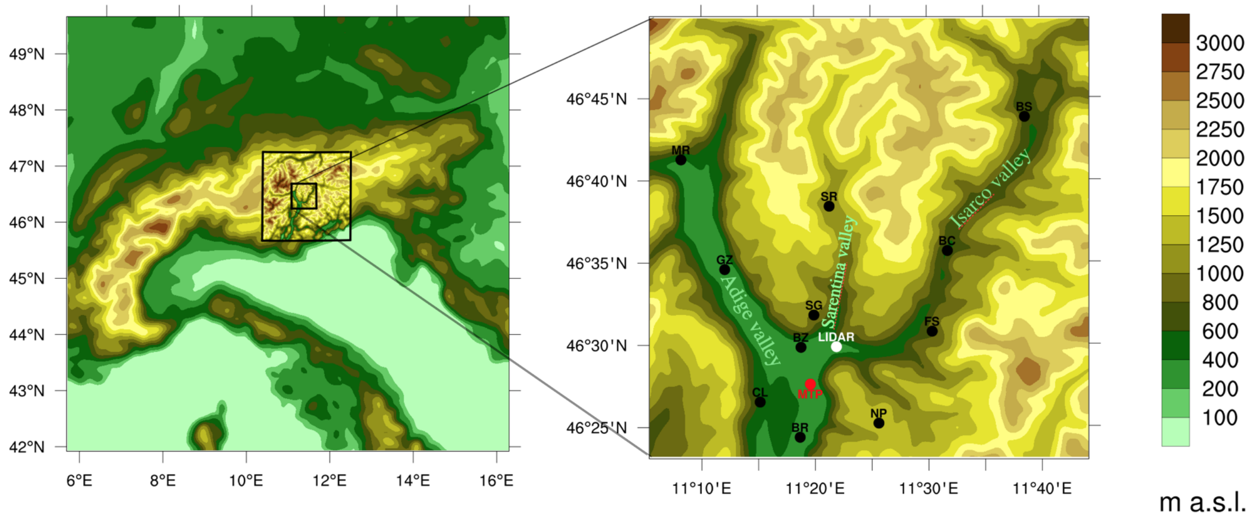

Figure 3.1: Map of the three nested domains used for the WRF simulations, with a zoom in the innermost domain shown on the right panel. The latter also shows the location of the instruments used to validate model results: lidar, temperature profiler (MTP) and 11 ground weather stations.

topography, it is not uncommon that the CAP persists also during daytime, lasting for several consecutive days. The interaction between the CAP and the local circulations in the Bolzano basin affects dispersion processes in the area, where significant emissions due to traffic, domestic heating and industrial activities are present (Bisignano et al., 2022), contributing to frequent poor air quality conditions.

3.2.2 BTEX experiment

The Bolzano Tracer Experiment (BTEX) took place in winter 2017 to study pollutant dispersion processes from a waste incinerator, located 2 km southwest of the city of Bolzano (Falocchi et al., 2020; Zardi et al., 2021). A passive gas tracer was released from the stack of the incinerator and then air samplings were collected in different locations at the ground. Different modelling chains were tested, where the WRF model was used to get meteorological variable fields required to drive different dispersion models, in order to evaluate their performance in reproducing dispersion patterns in the basin (Tomasi et al., 2019). During BTEX different instruments were used to monitor atmospheric conditions in the area, including a Doppler Wind Lidar, a thermal profiler and 15 ground weather stations (GWSs). The Doppler Wind Lidar, a WINDCUBE 100S manufactured by Leosphere (France), was installed on the roof of a building close to the exit of the Isarco Valley. It provided vertical profiles of the wind along 106 vertical levels, 10-m spaced (from 335 m to 1385 m a.s.l) and with a vertical resolution of 25 m, which are averaged over 10 min. The thermal profiler, a MTP-5HE passive microwave radiometer manufactured by ATTEX (Russia), was operated by the Environmental Protection Agency of the Province of Bolzano and installed south of the city at the local airport, providing temperature measurements every 10 min and interpolated along 21

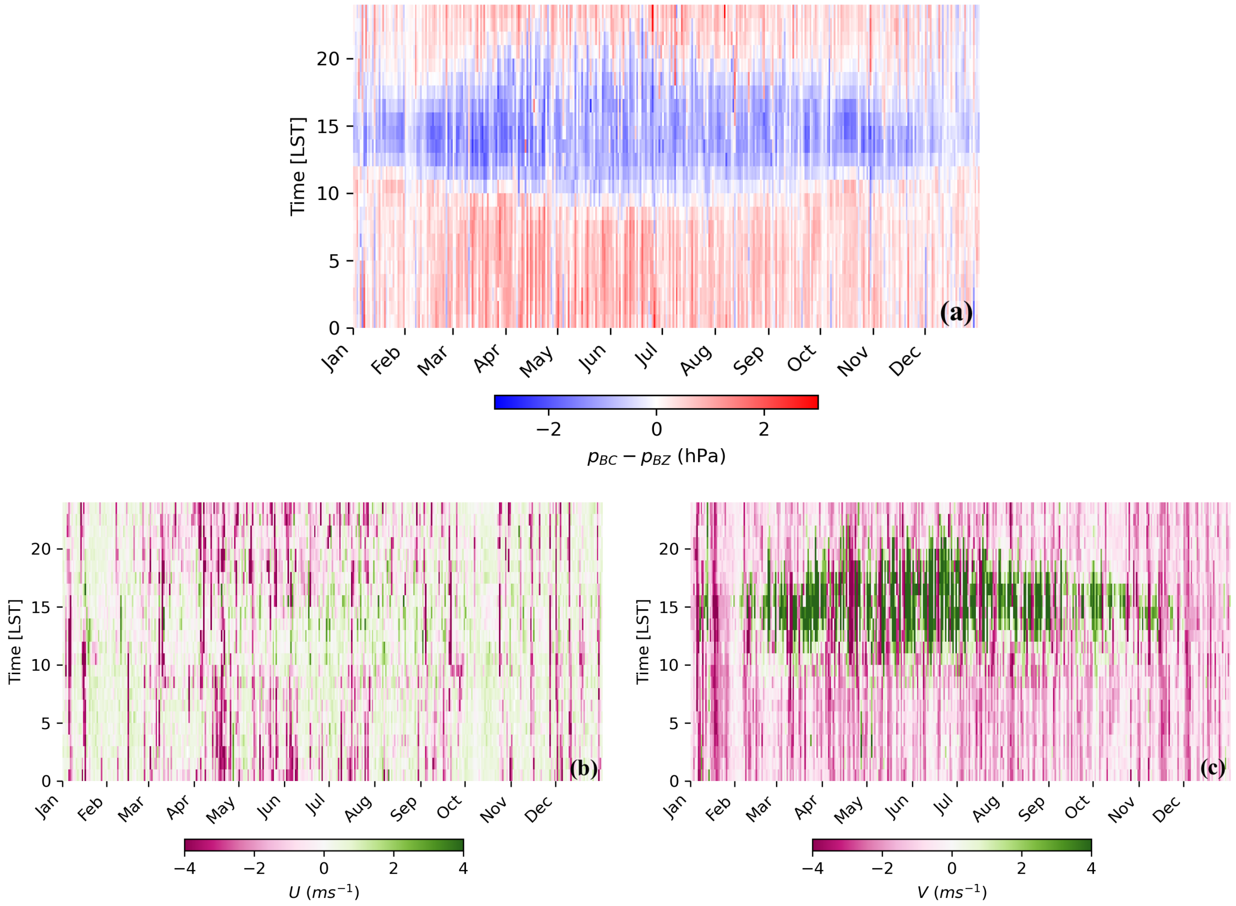

Figure 3.2: Annual evolution for year 2017 of (a) hourly mean pressure difference between BC GWS and BZ GWS and (b) hourly west-east component of the 10-m wind speed at BZ GWS and (c) hourly south-north component of the 10-m wind speed at BC GWS. Negative wind speed corresponds approximately to down-valley winds from the Isarco Valley.

vertical levels, 50-m spaced (from 250 m to 1250 m a.s.l.). GWSs were operated by the Meteorological Office of the Province of Bolzano. In this work 11 out of 15 GWSs are used, because two of them are located outside our domain of interest and two were not working during the selected case studies. The GWSs provide 10-min average data and are quite homogeneously distributed over the area, covering different heights from 226 m a.s.l. to 1470 m a.s.l.. Further information on the measurement set up can be found in (Falocchi et al., 2020), while a map with their location is shown in Figure 3.1 (right).

3.2.3 Local circulation and case studies

To illustrate some key aspects of the local circulation in the area, the results from the analysis of measurements performed in one year by two GWSs, as well as in two winter months by the thermal profiler, are presented here.

Figure 3.2a shows the diurnal and seasonal evolution of the pressure difference, on

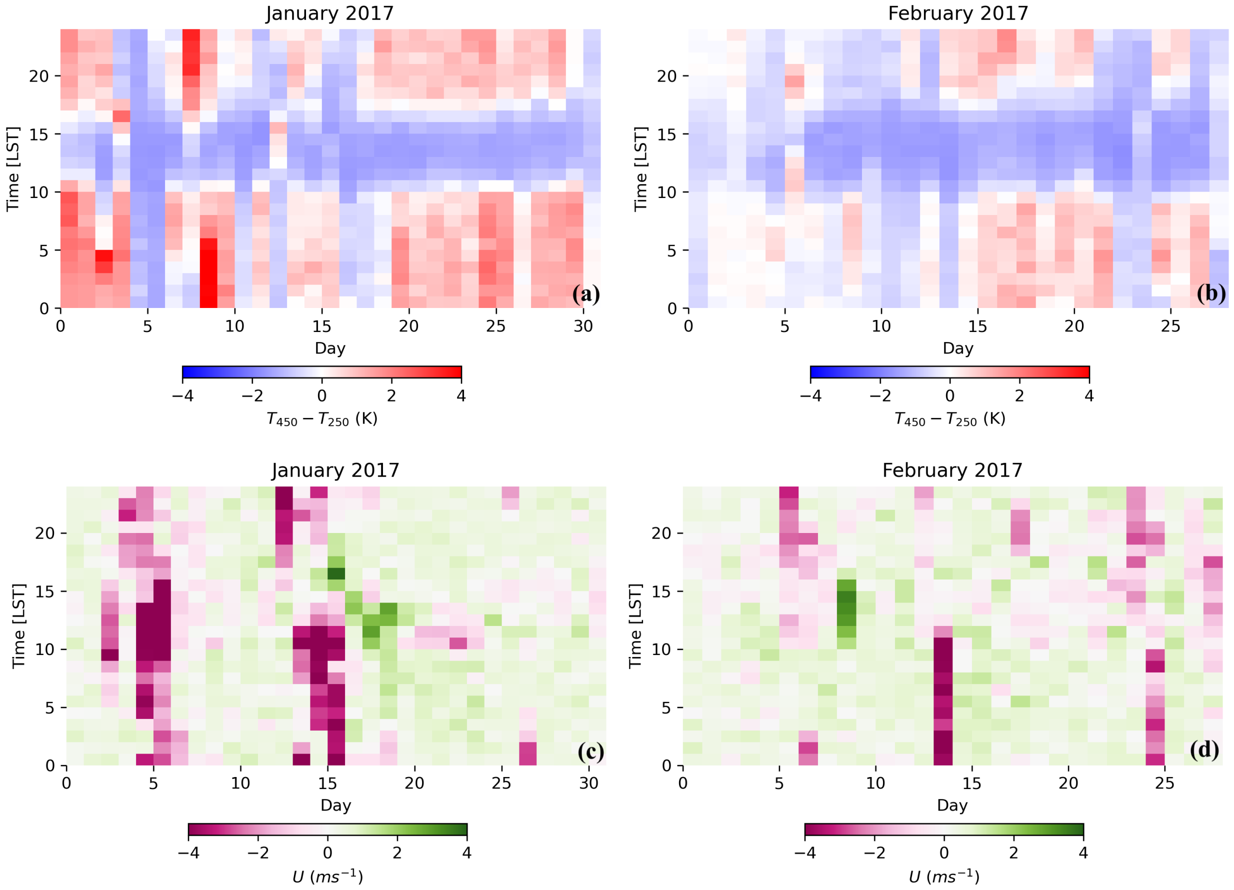

Figure 3.3: Monthly evolution of hourly temperature difference between 450 m and 250 m a.s.l from thermal profiler measurements in January (a) and February (b). Monthly evolution of hourly west-east component of the 10-m wind speed measured at BZ GWS, as in Figure 3.2b, in January (c) and February (d).

an hourly basis, between the GWS of Barbiano-Colma (BC), along the Isarco Valley, and the GWS of Bolzano (BZ), inside the basin, for the year 2017. To eliminate the effect of the different altitudes of the two stations (Table 3.1), the analysis is based on anomalies of pressure measurements with respect to their corresponding daily mean value. Overall, a diurnal evolution of horizontal pressure gradients, typical of thermally-driven circulations in valleys, is observed. Positive values dominate during nighttime, due to stronger cooling of the atmosphere in the Isarco Valley, and negative values during daytime, due to stronger warming of the Isarco Valley. Positive gradients, driving down-valley winds along the Isarco Valley, are stronger in spring and early summer, and their duration varies seasonally, according to times of sunrise and sunset. Figure 3.2b shows the west-east component of the 10-m wind speed measured at Bolzano, so that negative values are associated with the down-valley flow from the Isarco Valley. Larger pressure gradients in spring and early summer at night and in the morning are closely tied to stronger easterly winds at BZ GWS. Figure 3.2c shows the south-north component of the 10-m wind speed measured at BC GWS in the Isarco Valley. Down-valley flows (negative values) in winter in the Isarco Valley correspond less frequently to easterly winds at the

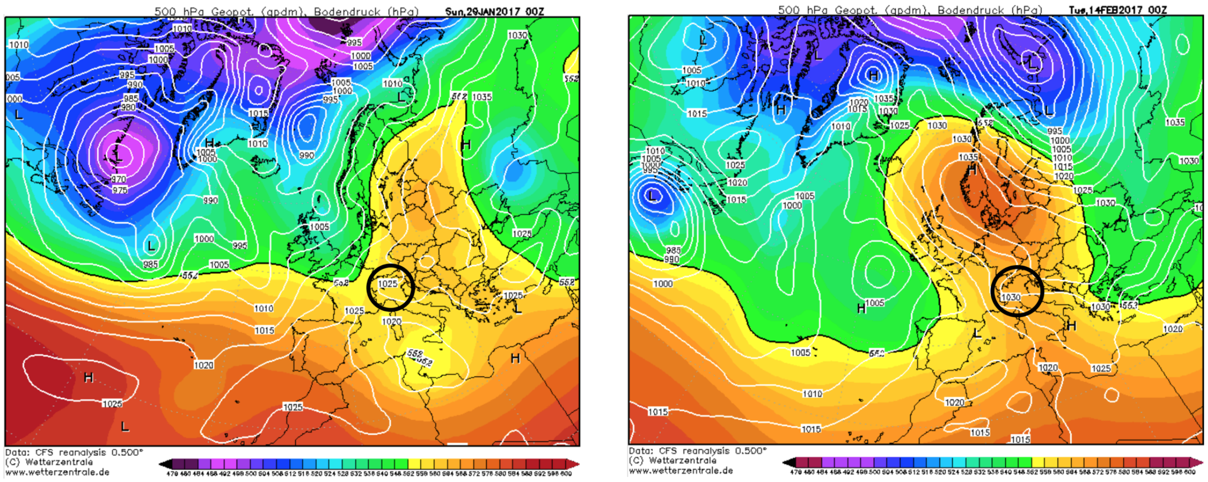

Figure 3.4: Synoptic situation in Europe at 00 UTC, 29 January 2017 (left panel) and at 00 UTC, 14 February 2017 (right panel). Colors show the 500 hPa geopotential height and isolines the sea-level pressure (https://www.wetterzentrale.de/).

ground in Bolzano with respect to spring and early summer. One of the mechanisms which might explain this fact is the frequent development of CAPs in the basin during wintertime. Indeed, the accumulation of cold air in the basin may lead the (potentially warmer) air exiting the Isarco Valley to rise above the CAP, without reaching the ground. To have further insights on this feature, measurements from the thermal profiler located at the Bolzano airport are related to wind speed measurements at BZ GWS for January and February 2017. Figure 3.3a,b shows the temperature difference between two levels, 450 m and 250 m a.s.l., with red colors corresponding to the occurrence of temperature inversions in the basin. While persistent CAPs are not observed, diurnal ones frequently occur, especially in January. Comparing this behaviour with Figure 3.3c, corresponding to the January data reported in Figure 3.2b, easterly winds at BZ during nighttime develop with no temperature inversion or with weak stratification in the basin. In February (Figure 3.2d), easterly winds are rarely observed at the ground, and the night between 13th and 14th appears to be an exceptional case of strong wind, occurring when a thermal inversion is not present in the basin. Due to few wintertime data available from the temperature profiler, it is not possible to draw statistically significant conclusions about a direct connection between temperature inversion and the penetration at ground level of the down-valley flow in the basin. However, case studies can be selected and investigated to better understand this mechanism.

In the present chapter, two fair-weather episodes with weak synoptic forcing and well-developed diurnal local circulations are studied. The two cases differ by the thermal stratification in the Bolzano basin, in order to investigate the interaction between the drainage flow at the outlet of the Isarco Valley and the air inside the basin.

Figure 3.4 shows the synoptic situation over Europe, with isobars at sea level and geopotential height at 500 hPa for the two case studies. In the 28-29 January 2017 case (Episode 1), northern Italy was under a high-pressure system with no appreciable synoptic winds (Figure 3.4 left) and the area of Bolzano was cloud free. These features

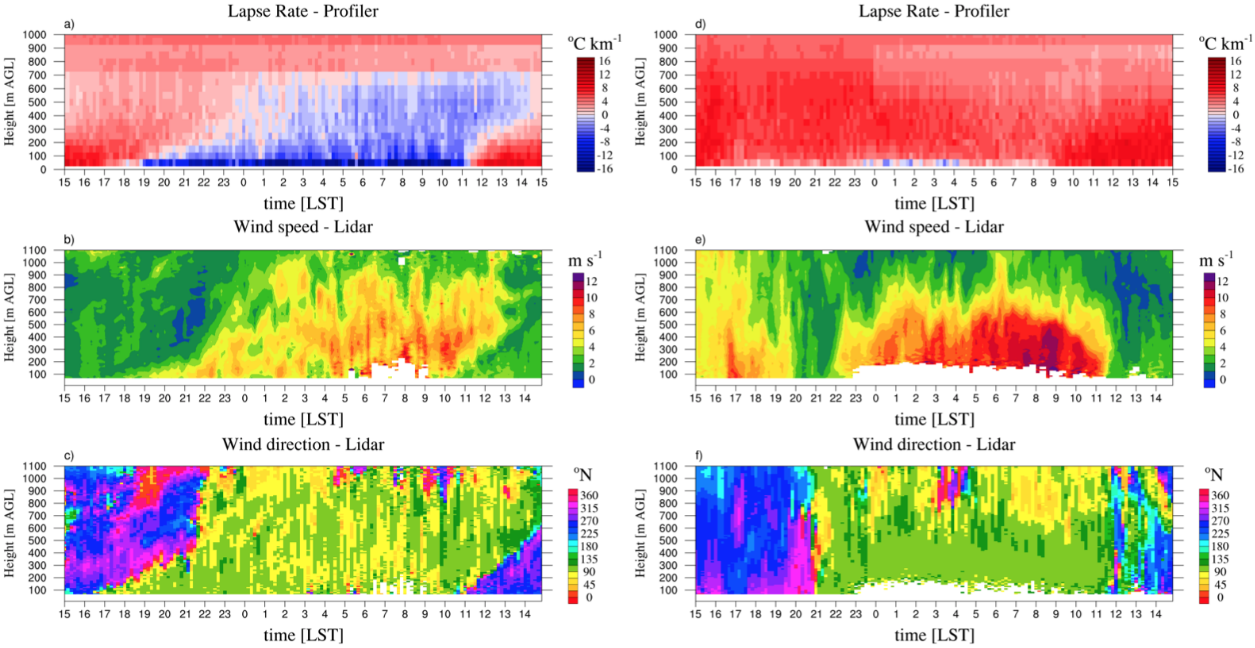

Figure 3.5: Time-height plots of the temperature lapse rate from thermal profiler measurements, and wind speed and direction from Lidar measurements. Panels a), b) and c) refer to 28-29 January and panels d), e) and f) to 13-14 February.

favoured the occurrence of a strong ground-based temperature inversion, as recorded by the thermal profiler (Figure 3.5a). The inversion layer grew few hours after sunset (local sunset around 16:00 LST), reaching a top height of 700 m AGL during the night, with a very strong stratification close to the surface. The ground-based temperature inversion persisted for some time after sunrise (local sunrise around 10:00 LST), and then started to be eroded from the lowest atmospheric layers. It is interesting to compare the development of the ground-based temperature inversion with the temporal evolution of wind speed and direction provided by the Lidar at the exit of the Isarco Valley. As shown in Figure 3.5b, the drainage flow started to develop when radiative cooling at the ground led to the formation of the thermally stable layer near the surface, and then the wind speed became continuously stronger in a deeper layer up to a height of 900 m AGL, following the evolution of the thermal structure into the basin. Peaks in wind speed were reached in the morning at 08:00 LST below 400 m AGL, with an intensity of $\sim 10\,\mathrm{m\,s^{-1}}$. Then the drainage flow rapidly died out, starting from the surface.
Figure 3.4 (right) shows that also the 13-14 February 2017 case (Episode 2) was characterized by high pressure conditions over northern Italy, but in this case weak southeasterly synoptic winds transported moisture from the Mediterrannean towards the Alps, as recorded by the increase in absolute humidity measured by many GWSs covering different heights (Falocchi et al., 2020, Figure 6c). As a consequence, stratocumulus clouds developed inside the valley at ~ 1200 m AGL during the night, hindering radiative cooling and the consequent formation of a ground-based temperature inversion in the basin, as can be seen in Figure 3.5d. It is interesting to compare the evolution of the drainage flow exiting the Isarco Valley in the two case studies. In Episode 2 measurements from

the Lidar show a concurrent increase of the wind speed at different heights around 22:00 LST, up to 600 m AGL, in contrast with the more gradual thickening of the drainage flow in Episode 1. Moreover, the wind intensity increased more rapidly throughout the night in Episode 2, reaching a peak of $12\,\mathrm{m\,s^{-1}}$ at 09:00 LST. The drainage flow rapidly died out some hours after sunrise, around 11:00 LST, and, as in the initial phase, this change in wind speed occurred rather uniformly at different heights.

3.3 Model set up

The WRF model version 4.3.1 (Skamarock et al., 2008) was used to perform the simulations presented in this work. Each simulation lasts 42 hours and starts the day before the night of interest (28 January 00 UTC and 13 February 00 UTC, respectively). The first 14 hours are considered as spin up time and are not taken into account in the following analysis. For each simulation, three two-way nested grids are used with 196^2, 196^2, 166^2 horizontal cells with grid spacing of 4.5 km, 0.9 km and 0.3 km, while 61 levels are used in the vertical direction, with 24 levels below 1000 m AGL and the first model level at 14 m AGL. The inner domain covers the area of interest, as shown in Figure 3.1 (right).

In the present work four different simulations for each episode are tested. A different PBL scheme is used in each simulation, while leaving all the other settings constant. The microphysics scheme adopted is WSM6 (Hong and Lim, 2006), while the RRTM scheme (Mlawer et al., 1997) is used for long-wave radiation and the Dudhia (1989) scheme for short-wave radiation, including the effects associated with slope inclination and topographic shading. The land surface model (LSM) adopted is Noah-MP (Niu et al., 2011) and no cumulus parameterization is used in all the domains. The microphysics scheme was selected to better reproduce the stratocumulus clouds in the valley, which were observed in Episode 2. The land surface parameterization, instead, is one of the most advanced LSM and, in this work, it has been properly modified to better reproduce soil temperature. An unrealistic deep frozen soil layer was in fact observed in the inner domain when using the default version of Noah-MP, lasting several hours even during daytime. This feature was attributed to super-cooled liquid water formation and thus this process was turned off.

The four PBL schemes tested are 1) the Yonsei State University (YSU, Hong and Lim, 2006), 2) the Mellor-Yamada-Janjic (MYJ, Janjic, 2002), 3) the Bougeault-Lacarrére (BouLac, Bougeault and Lacarrére, 1989) and 4) a k-ϵ-based closure recently proposed in Zonato et al., 2022 (KEPS-TPE). A detailed review of the different PBL schemes included in the WRF model can be found in Cohen et al. (2015).

These schemes are coupled to specific surface-layer schemes, in order to calculate surface-atmosphere exchange. The YSU, BouLac and KEPS-TPE are coupled to the MM5 scheme (Grell et al., 1994), while MYJ to the MYJ Eta surface layer scheme (Janjic, 1994). Both surface schemes are based on similarity theory, but the latter includes a parameterization of the viscous sublayer. The YSU PBL scheme is a first-order closure with a counter-gradient term accounting for nonlocal contribution to turbulent fluxes in convective conditions. MYJ and BouLac schemes are both 1.5-order closures with a prognostic equation for the TKE. The first one is based on Mellor (1982) (level 2.5), while the second one on Therry and Lacarrére (1983). The BouLac scheme was specifically designed to improve turbulent exchanges of heat and momentum in mountainous areas, where turbulence is affected by orography-induced gravity waves. The KEPS-TPE PBL scheme is a k-ϵ-based closure, including prognostic equations for the TKE, its dissipation rate and for the temperature variance. The heat flux parameterization includes a counter-gradient term proportional to the temperature variance, in order to account for the self-control mechanism of stratified turbulence, as suggested by Zilitinkevich et al. (2007).

Meteorological data from the ERA5 reanalysis released by the European Center for Medium-Range Weather Forecasts (ECMWF) are used to initialize the model and provide lateral boundary conditions every 6 hours, with a horizontal resolution of ~30 km on 137 vertical atmospheric levels and at the surface. Several preliminary simulations were performed in order to improve the initial surface conditions. In fact, it is now well-known that the increase of the spatial resolution of the model without incorporating improved surface data does not automatically imply an improvement of the model performance (Chow et al., 2006). In particular, attention was paid to soil moisture and snow cover. These fields, which are generally available on the coarser grids of global models, have a strong impact on the surface energy budget, influencing the development of thermally-driven circulations and the near-surface stratification (Ookouchi et al., 1984; Banta and Gannon, 1995; Massey et al., 2016; Tomasi et al., 2017; Jiménez et al., 2019). At the beginning of the present work, initial conditions from ERA5 led to an overestimation of snow cover for both case studies, with snow cover even inside the Adige Valley, which was not present. On the basis of photographs taken during the field campaign, in later runs the snow cover was limited to heights above 2000 m AGL. Concerning soil moisture, unfortunately no in situ observations were available in the area, to correct model initialization. Therefore, observations from satellite SMAP (https://worldview.earthdata.nasa.gov), with a horizontal resolution of 9 km were adopted to improve initial conditions. For Episode 1, the comparison between SMAP soil moisture values and model initialization suggested to halve soil moisture values provided by ERA5. A similar overestimation of soil moisture values from reanalysis data was found in Giovannini et al. (2014) in the Adige Valley. For Episode 2, instead, no adjustment was needed.

In order to obtain accurate simulations at sub-kilometer scale over highly complex terrain, it is also important to use high-resolution topography and land use data sets. Default WRF datasets for these variables have a spatial resolution of 30 arc-s (~1 km), which is too coarse for our purposes. Therefore, topography data were obtained from the Viewfinder Panoramas website (http://www.viewfinderpanoramas.org) with a spatial resolution of 1 arc-s (~ 30 m) and slightly smoothed to prevent numerical instability at sharp edges. Similarly, the Corine Land Cover (CLC) dataset updated to 2012, provided by the European Environment Agency (http://www.eea.europa.eu), with a spatial resolution of 100 m, was employed as land use dataset after a proper reclassification of CLC classes into the 20 MODIS classes adopted by WRF, following Giovannini et al. (2014).

3.4 Results

3.4.1 28-29 January 2017: Episode 1

Figure 3.6 shows the time-height plots of temperature from the profiler and simulations for Episode 1. None of the PBL schemes is able to reproduce the depth of the CAP, reaching up to 1000 m AGL during nighttime. However, the depth of the CAP is closer to observations in the simulation with the KEPS-TPE PBL scheme. This may be attributed to the enhancement of turbulent diffusion for strongly stable conditions, related to the additional prognostic equation of temperature variance that influences the vertical heat flux (Zonato et al., 2022), preventing the TKE collapsing with increasing stratification. TKE is sustained by the conversion of turbulent potential energy (TPE), proportional to the temperature variance. It can also be noted that YSU, despite its simplicity, performs better than the more advanced MYJ and BouLac PBL schemes.

Figures 3.7 and 3.8 show the time-height plots of wind speed and direction at the Lidar location. All PBL schemes reproduce the onset of the valley wind exiting the Isarco Valley with a slight delay, even if KEPS-TPE shows the best agreement with observations also for these variables. All schemes, except MYJ, well reproduce the internal structure of the valley-exit wind, whose development is strictly connected with the growth of the ground-based temperature inversion. The easterly valley-exit wind starts at 21:00 LST, intensifies during the night, reaching the peak velocity around 8:00 LST. MYJ, instead, tends to overestimate the base of the drainage flow, reproduced at 200 m AGL.

The temporal evolution of the valley-exit flow follows that of a thermally-driven down-valley wind, as also suggested by simulation outputs in Figure 3.9. Figure 3.9b shows the vertically-averaged hourly temperature difference between the Bolzano basin (T_{out}) and the Isarco Valley (T_{in}), evaluated from the differences between the air columns, up to the crest height ($\sim$ 2500 m a.s.l.), at the two grid cells corresponding to the dots A,C in Figure 3.9a. It exhibits a clear diurnal cycle, reversing sign around 17:00 LST and 11:00 LST, i.e. after sunset and sunrise. This is consistent with the hourly differences of the vertically-averaged pressure, calculated between the same two air columns, shown in Figure 3.9c, where it can also be noted that MYJ simulates the weakest gradient during nighttime, in agreement with the weakest temperature gradient in Figure 3.9b. The corresponding vertically-averaged U component of the wind at the exit of the valley (dot B in Figure 3.9a) displays a diurnal cycle as well, with negative values for easterly winds (Figure 3.9d) and the lowest values reproduced by MYJ.

Figure 3.10 confirms the lack of a dynamical contribution to the down-valley flow in this episode. In fact, winds at 4000 m a.s.l. (as reproduced by YSU, but all simulations show analogous results) weaken during the night, displaying an intensity of about 5 m s^{-1}, blowing from South.

In order to better characterize the structure of the valley-exit wind and how the model reproduces it, three vertical profiles of hourly averaged wind speed are shown in Figure 3.11. At the beginning of the night the flow has a structure with multiple peaks which are then lost in the following hours, and in the morning large velocities are

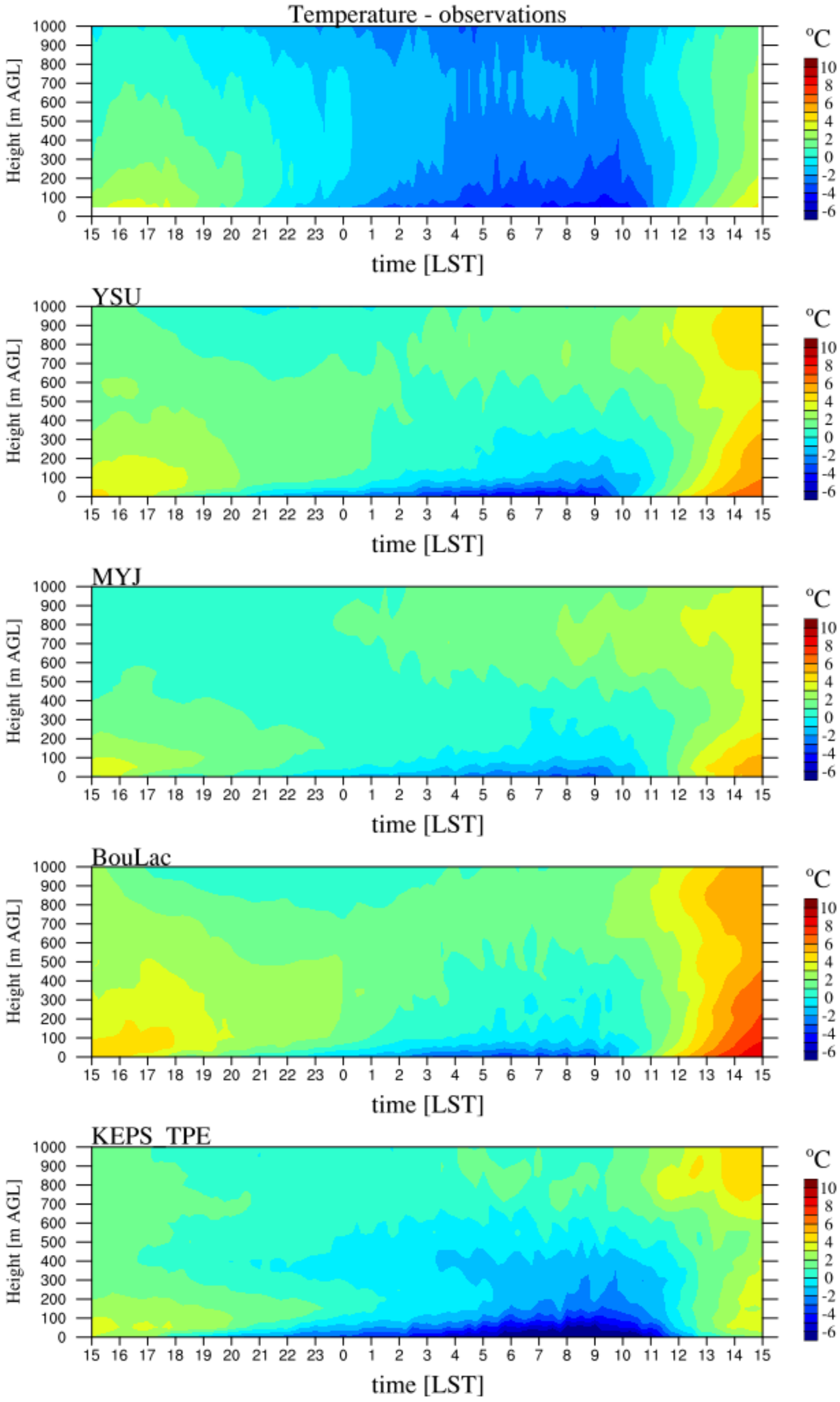

Figure 3.6: Time-height plots of temperature for Episode 1 at the site of the vertical profiler. Comparison between temperature from profiler measurements (upper panel) and results from the four simulations, at the grid cell closest to the vertical profiler site in the inner domain.

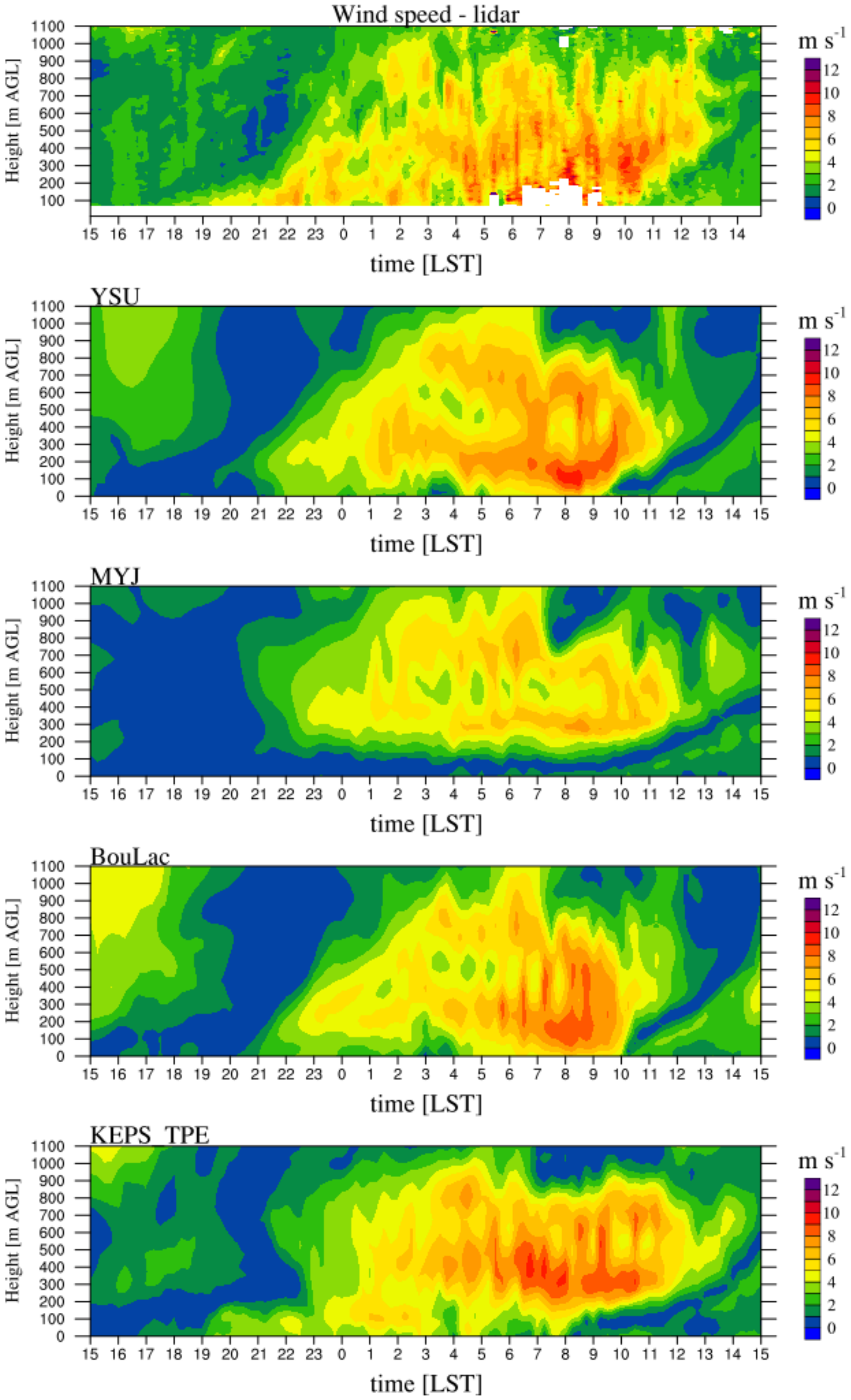

Figure 3.7: Time-height plots of wind speed for Episode 1 at the site of the Lidar. Comparison between wind speed from Lidar measurements (upper panel) and results from the four simulations, at the grid cell closest to the Lidar site in the inner domain.

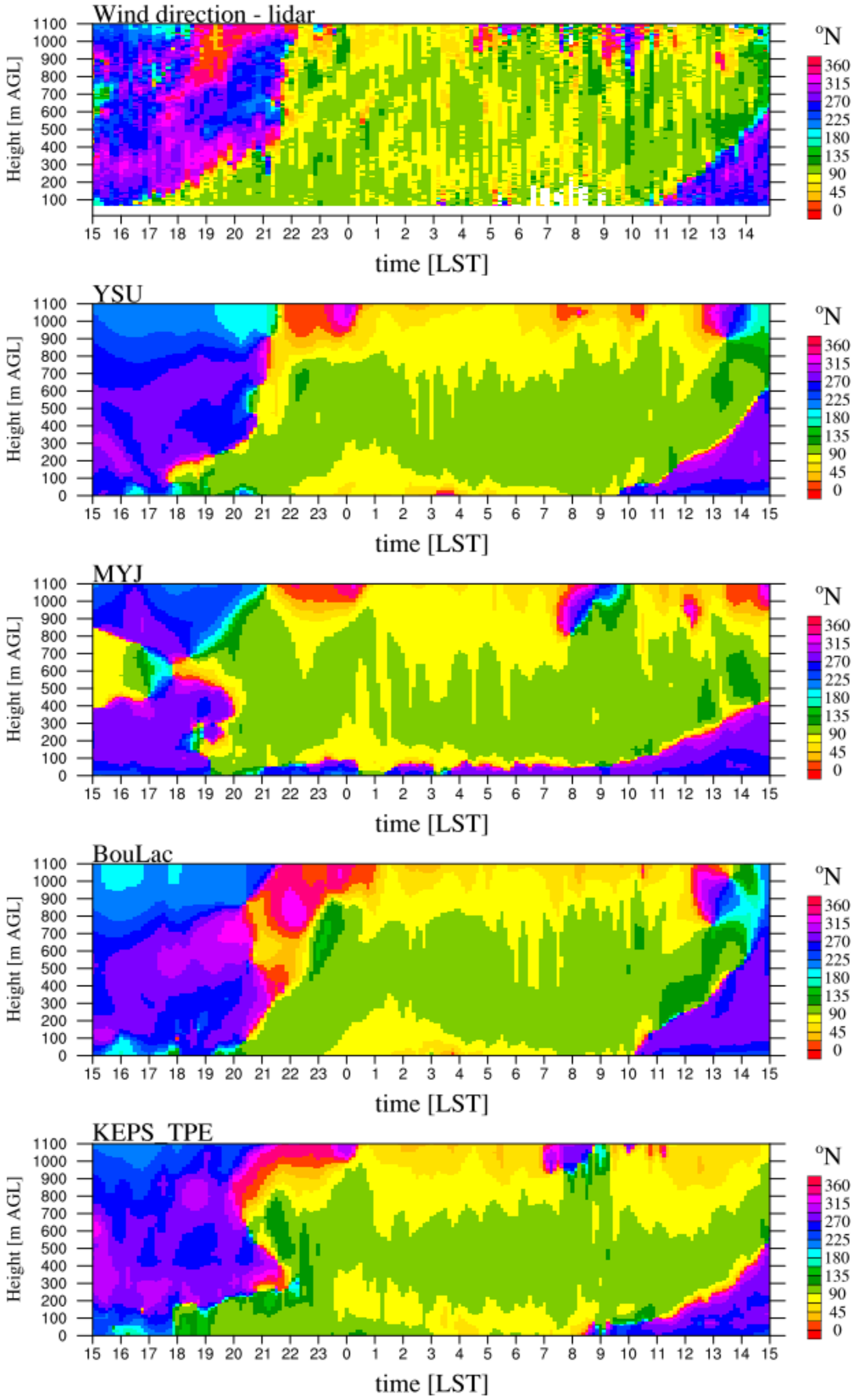

Figure 3.8: Time-height plots of wind direction for Episode 1 at the site of the Lidar. Comparison between wind direction from Lidar measurements (upper panel) and results from the four simulations, at the grid cell closest to the Lidar site in the inner domain.

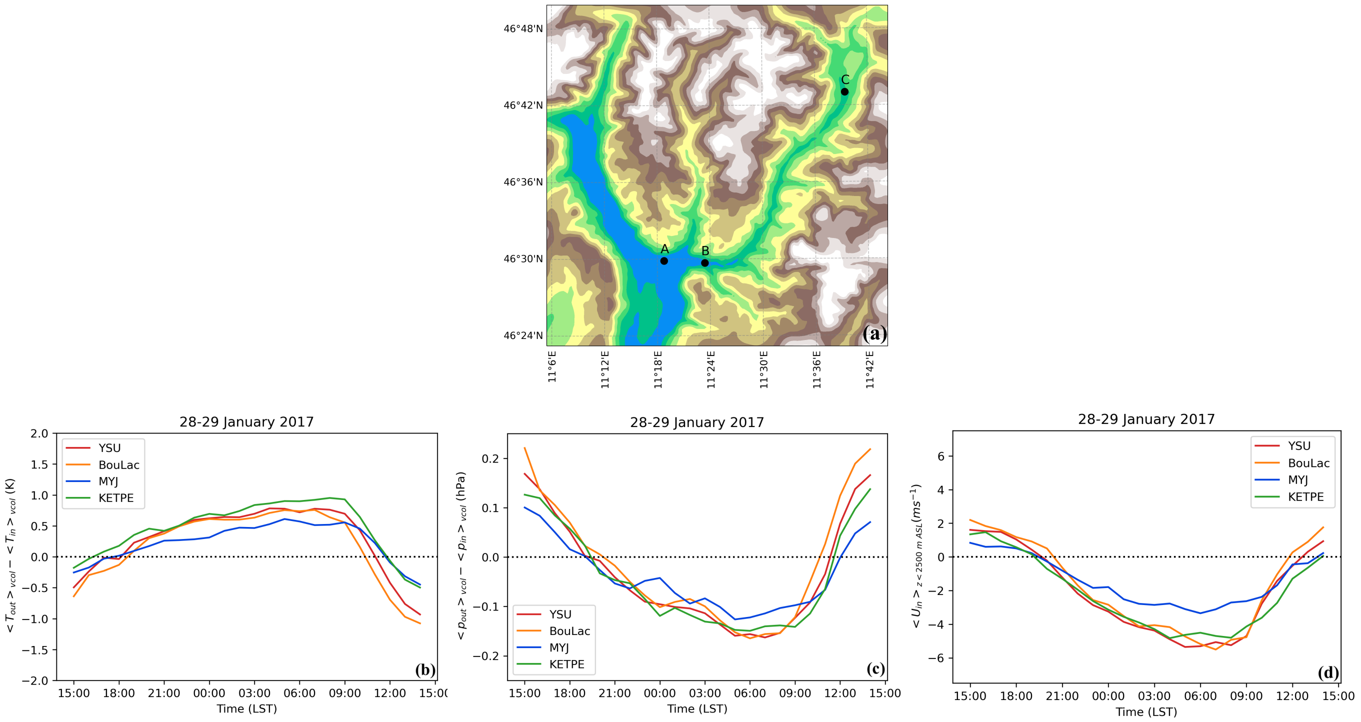

Figure 3.9: Time series for Episode 1 of the simulated vertically-averaged hourly temperature (b) and pressure (c) difference between the air columns, ranging from 600 m up to 2500 m a.s.l., at the grid cells corresponding to dots A and C in panel (a), representative of the Bolzano basin and the Isarco Valley. Panel d) shows the time series of the vertically-averaged U component of the wind at the exit of the Isarco Valley up to 2500 m a.s.l., evaluated at the grid cell corresponding to the dot B shown in panel (a).

observed also at the lowest atmospheric layers. All schemes reproduce two peaks once the flow starts to intensify (03:00 LST) and they are preserved until the morning, when the profile becomes more uniform. YSU captures very well the structure of the flow in the lowest atmospheric layers, slightly enhancing the vertical shear close to the surface. MYJ shows the largest underestimation of wind intensity, likely related to the weakest pressure gradient presented in Figure 3.9c.

Figure 3.12 shows the vertical component of the wind velocity, with blue and red colors corresponding to downward and upward velocity, respectively. During nighttime, the Lidar measured a strong upward velocity at the exit of the Isarco Valley, which seems related to the rise of the drainage flow over the CAP in the Bolzano basin. As also shown by GWS measurements in Figure 3.3c, no easterly wind was indeed observed at the ground in Bolzano during Episode 1. The wrong estimate in MYJ of the base of the valley-exit wind (as seen in Figure 3.7 and Figure 3.8) and of the vertical velocity are attributed to a ground-based temperature inversion more extended towards the Isarco Valley in this simulation (not shown), with the valley-exit wind rising above it a few cells further east with respect to the other schemes. The sensitivity to the grid cell selected for this analysis also explains the apparent lower performance of KEPS-TPE, although it better reproduced the thermal stratification in the basin. The YSU and BouLac schemes well reproduce an upward motion up to 600 m AGL and a downward

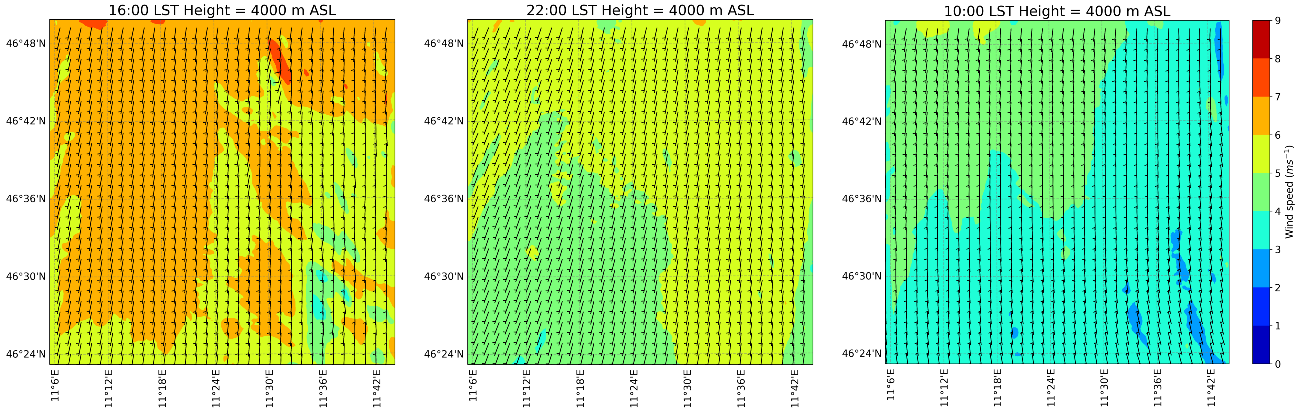

Figure 3.10: Wind speed and wind barbs at 4000 m a.s.l. from the YSU simulation at different hours.

motion above.

Figure 3.13 shows one of the mechanisms responsible, according to the simulations, for the rising motion of the down-valley flow once it reaches the basin. The upward vertical velocity component during nighttime at the exit of the Isarco Valley is driven by the difference in potential temperature (vertically averaged) between the two air masses merging in the basin. In fact, a lower vertical velocity (Figure 3.13c) corresponds to a lower temperature difference (Figure 3.13b), as seen for the simulation with MYJ. However, other mechanisms seem also to affect the intensity of the rising motion, as suggested by the BouLac simulation, which reproduces the largest difference in potential temperature, but not the largest vertical velocity.

Finally, it is worth pointing out that the vertical component of the wind velocity measured by the Lidar (Figure 3.12) shows oscillations from positive to negative values with periods of about 30-40 min. These oscillations are more intense in the early hours of the night, when the drainage flow starts blowing from the Isarco Valley. This feature is partly captured by YSU and BouLac at the beginning of the night.

Quantitative evaluation of model results

For a quantitative overview of the performance of the model with the different PBL schemes, we proceed by comparing results and observations in terms of mean error (ME) and root-mean-square error (RMSE).

The atmospheric conditions at the surface are validated against measurements from the GWSs. ME and RMSE are estimated from hourly averages in the period 28-01-2017 15:00 LST to 29-01-2017 18:00 LST, and are summarised in Table 3.1 and Table 3.2 for 2-m temperature and 10-m wind speed, respectively. The minimum value of ME and RMSE at each GWS is shown in bold. Considering 2-m temperature, it can be seen that the ME is generally positive for all the simulations, meaning on average model overestimation, with the exception of KEPS-TPE, which shows underestimations at most GWSs. Overall, the best performance is obtained with YSU, as can be seen also from RMSE values.

#	GWS	Height	ME				RMSE			
	T2	(m a.s.l)	YSU	MYJ	BouLac	KEPS-TPE	YSU	MYJ	BouLac	KEPS-TPE
1	BR	226	**0.1**	0.6	1.4	-2.4	**1.5**	2.4	2.0	3.4
2	BS	254	3.1	3.3	3.9	**0.9**	3.5	3.9	4.2	**2.4**
3	BZ	254	**-0.2**	0.8	1.1	-2.3	**1.2**	2.3	1.8	3.1
4	GZ	290	1.5	2.7	3.0	**-1.2**	**2.7**	4.1	3.9	3.3
5	MR	330	2.3	2.0	3.0	**1.0**	3.0	**2.7**	3.5	3.0
6	BC	490	2.3	2.4	3.0	**-0.8**	2.9	3.1	3.6	**1.5**
7	CL	495	**-0.1**	-0.8	0.8	-1.9	**0.9**	1.3	1.2	2.1
8	FS	840	**0.3**	0.4	1.1	-0.5	**0.9**	1.4	1.2	1.4
9	SR	970	1.8	2.0	2.3	-1.8	**2.0**	2.5	2.4	2.9
10	SG	970	2.7	2.6	3.2	**2.2**	3.1	3.1	3.4	**3.0**
11	NP	1470	-0.6	-0.9	**-0.4**	-1.1	1.5	1.7	**1.4**	1.6

Table 3.1: ME and RMSE for the 2-m temperature of the different simulations for Episode 1. Estimates are computed from hourly averages of GWS measurements and WRF outputs in the interval 28-01-2017 15:00 LST - 29-01-2017 18:00 LST.

#	GWS	Height	ME				RMSE			
	WS10	(m a.s.l)	YSU	MYJ	BouLac	KEPS-TPE	YSU	MYJ	BouLac	KEPS-TPE
1	BR	226	-0.5	**0.0***	-0.3	-0.3	0.7	0.8	0.7	0.7
2	BS	254	0.3	-0.1	0.4	**0.0***	0.7	**0.3**	0.7	0.4
3	BZ	254	-0.1	-0.1	**0.0***	-0.1	0.4	**0.3**	0.5	0.4
4	GZ	290	0.3	**0.1**	0.3	0.2	0.6	0.6	0.6	0.6
5	MR	330	0.1	0.1	**0.0***	0.2	0.5	0.6	0.5	**0.4**
6	BC	490	2.0	0.5	1.7	**0.3**	2.3	1.2	2.0	**0.8**
7	CL	495	0.2	-0.8	0.1	-0.1	0.7	1.3	0.7	0.9
8	FS	840	-0.1	**0.0***	0.1	-0.1	**0.3**	0.3	0.3	0.5
9	SR	970	-0.2	-0.4	**0.0***	0.9	**0.4**	0.5	0.5	1.7
10	SG	970	0.3	**0.0***	0.2	0.2	0.6	0.4	0.4	0.6
11	NP	1470	-0.2	-0.7	-0.2	-0.4	0.6	0.9	0.6	0.7

Table 3.2: ME and RMSE for the 10-m wind speed of the different simulations for Episode 1. Estimates are computed from hourly averages of GWS measurements and WRF outputs in the interval 28-01-2017 15:00 LST - 29-01-2017 18:00 LST. The symbol * means |ME| less than 0.05.

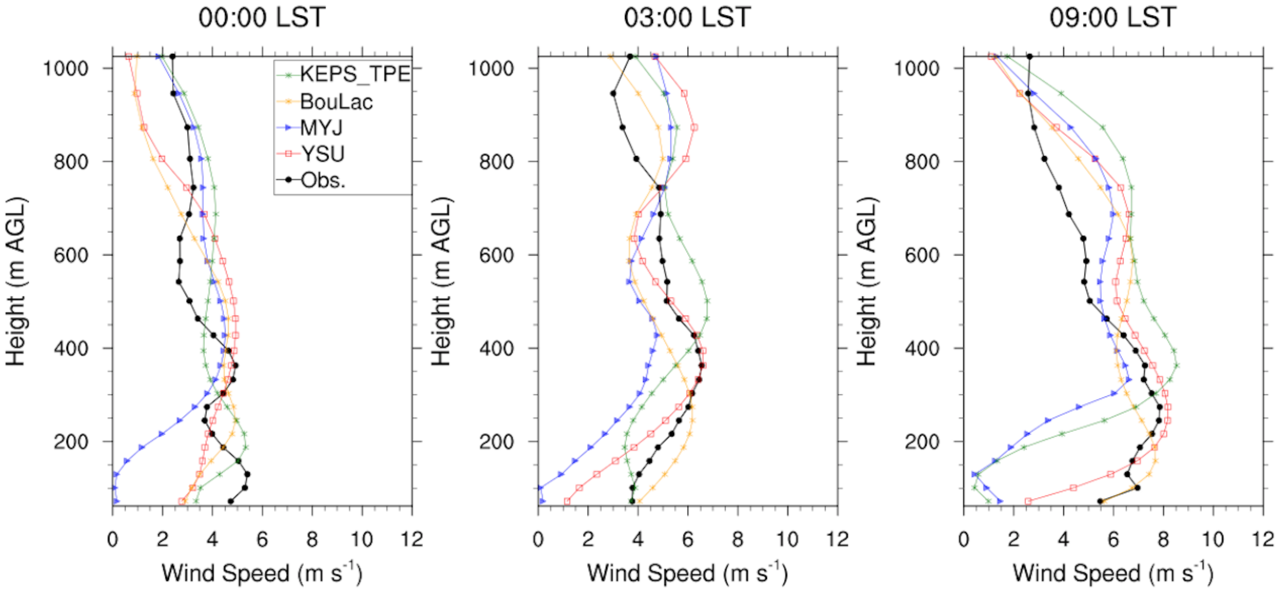

Figure 3.11: Vertical profiles of hourly averaged wind speed for Episode 1. Profiles from simulations are compared with observations at different hours of the night.

The ME of 10-m wind speed is quite small for all the simulations, mostly less than $1\,\mathrm{m\,s^{-1}}$ and without any significant difference related to the GWS location. The best model performance in representing the mean value of wind speed across the area is obtained with BouLac, even if this is not systematic, as at other GWSs MYJ performs better. The ME is generally positive for BouLac. Differently from the 2-m temperature, YSU is never the PBL scheme with the lowest value of ME. However, this scheme generally presents the lowest RMSE. This means that, while positive and negative hourly mean errors tend to compensate each others in the simulations with the other PBL schemes, the simulation with YSU has a more constant tendency to under- or overestimate the 10-m wind speed.

In order to better highlight the behaviour of the PBL schemes in reproducing 2-m temperature and 10-m wind speed, the time series of three GWSs, representative of the Isarco Valley (Barbiano Colma), the Bolzano basin (Bolzano) and the Adige Valley (Bronzolo), are shown in Figure 3.14. All PBL schemes overestimate the temperature during nighttime, with the exception of KEPS-TPE PBL, which is in good agreement with observations. On the other hand, during daytime, KEPS-TPE tends to significantly underestimate temperature, especially at Bolzano and Bronzolo, thus suggesting that the overall ME for this scheme, shown in Table 3.1, should be attributed to daytime conditions. During daytime the temperature is slightly underestimated also by MYJ and YSU at Bolzano and Bronzolo, where BouLac displays a very good agreement with observations. All schemes, except KEPS-TPE, tend to overestimate the near-surface temperature in the Isarco Valley even during daytime.

All PBL schemes, in agreement with observations, reproduce a weak and mostly constant wind speed at 10-m AGL at Bolzano and Bronzolo. During nighttime YSU and BouLac overestimate wind speed at Barbiano-Colma, which seems to be associated

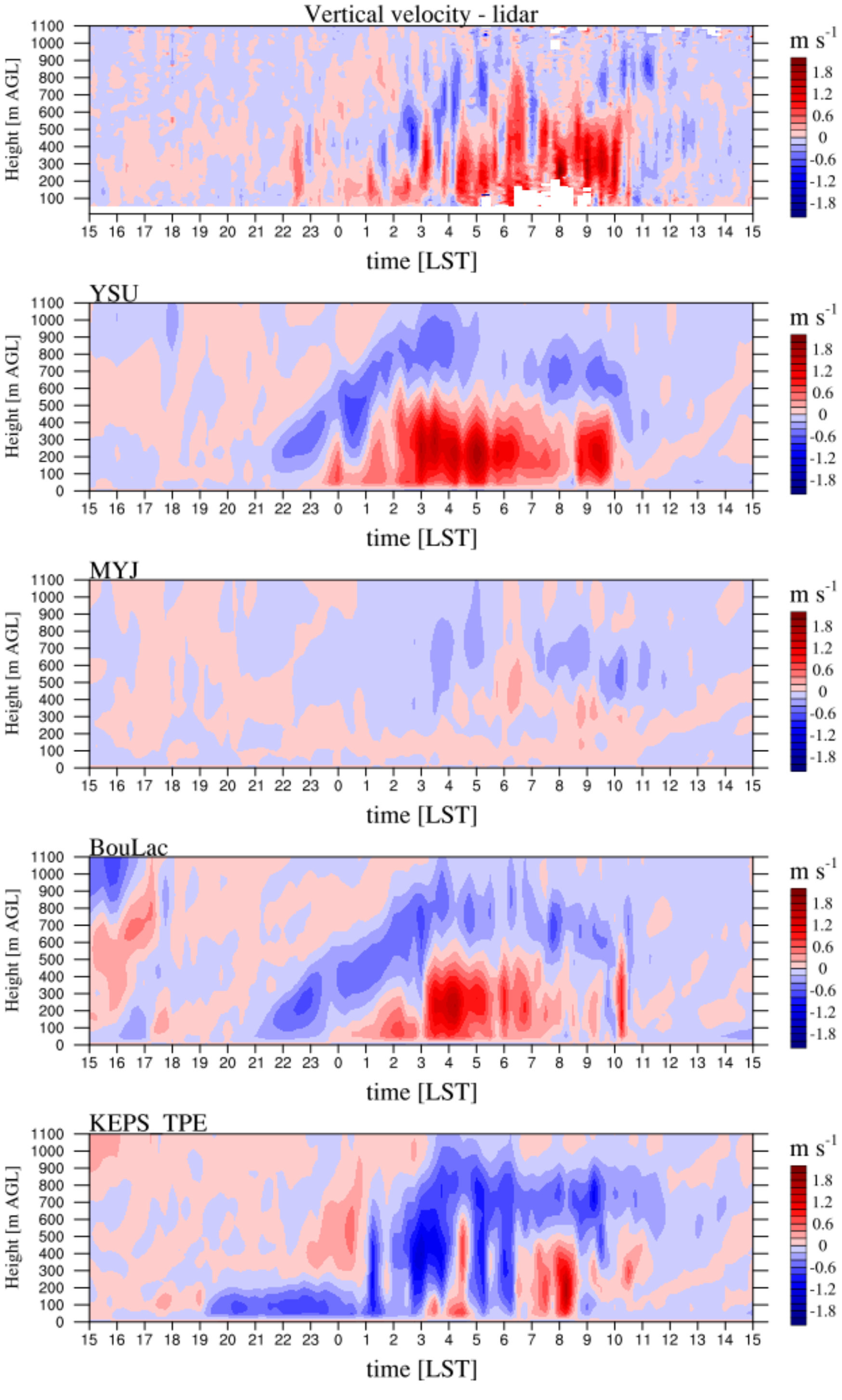

Figure 3.12: Time-height plots of the vertical component of wind velocity for Episode 1 at the site of the Lidar. Comparison between Lidar measurements (upper panel) and results from the four simulations, at the grid cell closest to the Lidar site in the inner domain.

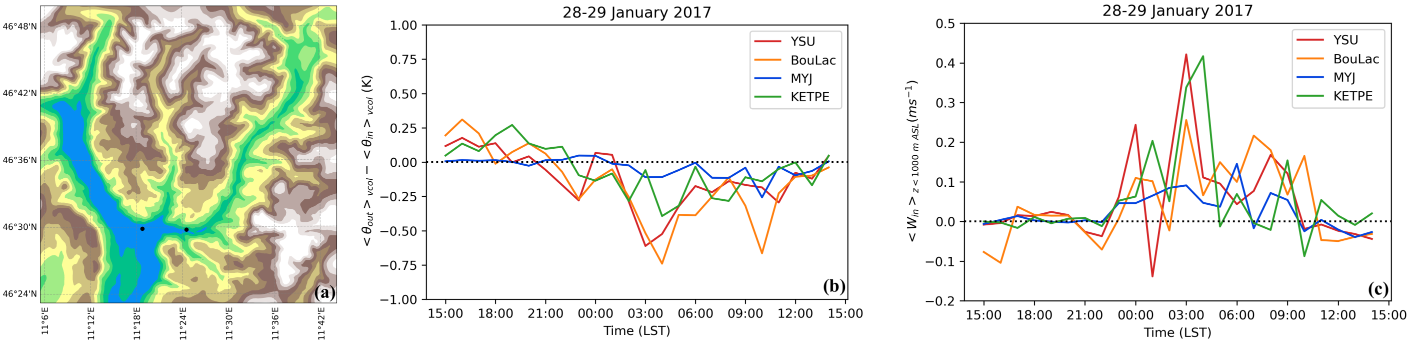

Figure 3.13: Time series for Episode 1 of the simulated vertically-averaged hourly potential temperature difference between the two air columns, ranging from 400 m up to 1000 m a.s.l., at the grid cells corresponding to the two points in panel (a), representative of the Bolzano basin and the exit of the Isarco Valley (b). Panel (c) shows the vertical component of the wind reproduced by the model at the valley exit, vertically-averaged over an air column ranging from 400 m up to 1000 m a.s.l. .

with the onset of the drainage flow in the Isarco Valley. These schemes thus reproduce a tendency of the drainage flow to reach the ground, which is instead not confirmed by observations. Model errors at Barbiano-Colma may be due to the complex topography of the valley, which is very narrow at this location. Local atmospheric conditions, such as a ground-based temperature inversion interacting with the drainage flow and leading to a vertical displacement of the flow, may not be correctly captured because of the horizontal resolution of the model.

A quantitative comparison in terms of ME and RMSE is also performed for the vertical profiles of temperature and wind speed, using the grid cell closest to the location of the temperature profiler and the Lidar, respectively. In this case, our focus is on the evaluation of the PBL schemes performance in reproducing the valley-exit wind and the concurrent temperature stratification in the Bolzano basin, and thus the analysis is restricted to the period 29-01-2017 00:00 LST to 29-01-2017 12:00 LST. Results are shown in Figure 3.15, and are based on hourly averages. Observations are linearly interpolated along the vertical from observation heights to model levels for this comparison.

All PBL schemes tend to overestimate the temperature along the vertical, with, except KEPS-TPE, an increase of ME and RMSE up to 200 m AGL, reaching an overestimation of about 3 °C, which then remains more or less constant above, with small differences between YSU, MYJ and BouLac. The KEPS-TPE scheme, instead, has a negative ME in the lowest atmospheric layers, consistent with the results from the GWS near-surface measurements shown in Table 3.1. Above 150 m AGL, KEPS-TPE presents the best agreement with observations among all PBL schemes, with a general increase of ME and RMSE above 700 m AGL, where the top of the ground-based inversion is located.

The model performance is also affected by the choice of the PBL scheme in reproducing the vertical profile of wind speed, with YSU exhibiting the best agreement with Lidar observations, with ME generally lower than 1 m s^{-1}. Below 400 m AGL, all PBL

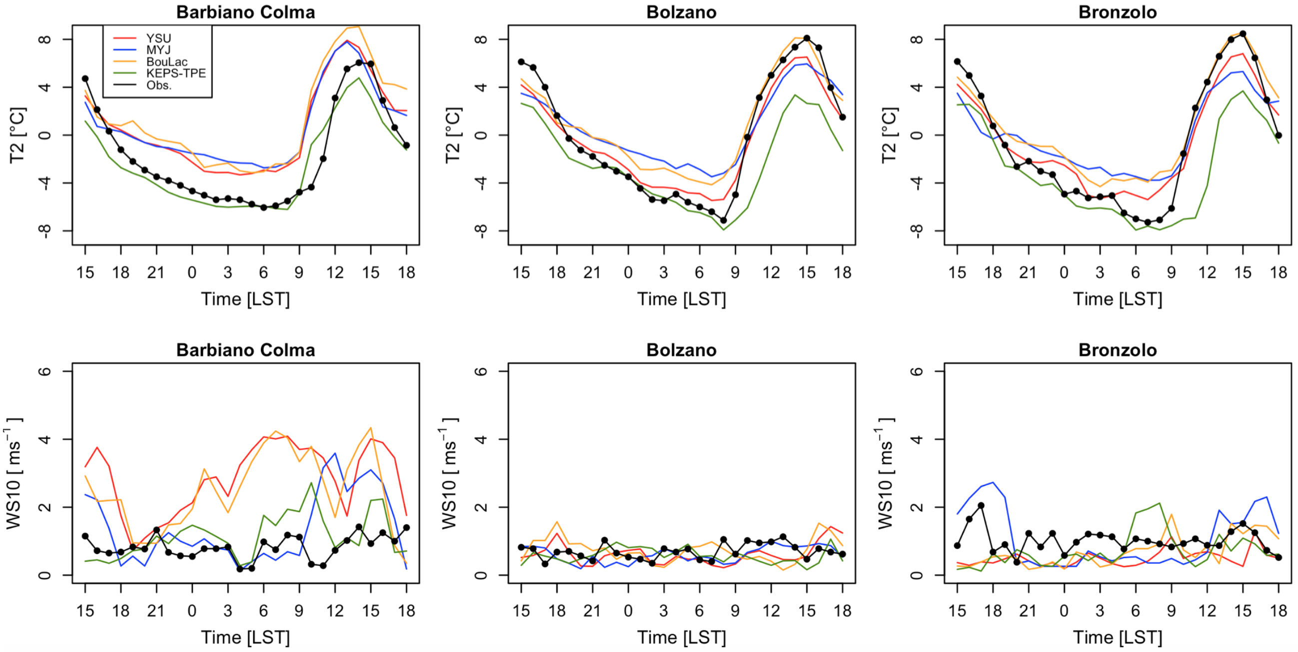

Figure 3.14: Hourly time series of 2-m temperature (upper panel) and 10-m wind speed (lower panel) at the GWSs of Barbiano-Colma, Bolzano and Bronzolo from observations (black line and dots) and model results for Episode 1.

schemes underestimate the wind intensity, with MYJ showing a strong negative bias, related to the overestimation of the base of the valley-exit wind and to a weaker horizontal pressure gradient, as already highlighted in Figure 3.7 and Figure 3.9c, respectively.

3.4.2 13-14 February 2017: Episode 2

Figure 3.16 shows the time-height plots of the temperature vertical profiles from the profiler and the simulations for Episode 2. During daytime all schemes show a good agreement with observations except the MYJ scheme, which underestimates temperature, in particular for the first day of the simulation. A comparison between the surface sensible heat flux from the different simulations did not show significant differences, thus excluding the different surface-layer scheme coupled with MYJ (Section 3.3) as a possible cause of this underestimation. During the night, all schemes reproduce quite well the vertical structure of the atmosphere, but they tend to underestimate the overall temperature of 2 °C - 3 °C, except the BouLac scheme. The latter is characterised by higher temperature during daytime, thus it reaches warmer temperatures in the morning, while reproducing a nocturnal cooling comparable to the other schemes. YSU and KEPS-TPE well reproduce the evolution of the valley-exit wind measured by the Lidar, as shown in Figure 3.17 and in Figure 3.18 for wind speed and direction, respectively. They show a strong easterly flow at the exit of the Isarco Valley, starting at about 2:00-3:00 LST (with a few hours of delay with respect to observations) and lasting until the morning, well reproducing the continuous intensification with a velocity peak after sunrise (occurring at approximately 08:30 LST). This is particularly true for KEPS-TPE, where

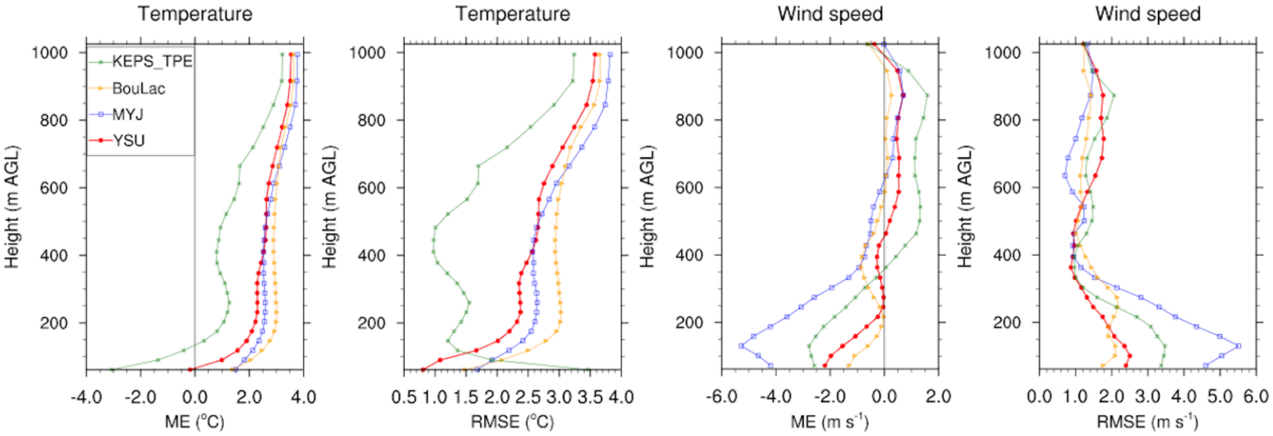

Figure 3.15: Average vertical profiles of ME and RMSE referring to the temperature measured by the profiler and the wind speed measured by the Lidar, evaluated from hourly averages from 29-01-2017 00:00 to 29-01-2017 12:00.

the flow reaches a velocity of ~12 m s^{-1} between 08:00 LST and 09:00 LST. However, a general underestimate of wind speed is observed throughout the night by all schemes, with the KEPS-TPE being the one closest to observations. In the early afternoon of the first day, all schemes agree on a north-westerly wind (Figure 3.18), probably related to southerly synoptic wind channeling into the Adige Valley (Whiteman and Doran, 1993) and presenting as an up-valley wind in the Isarco Valley. This channelling mechanism strengthens the up-valley wind, more intense in this case with respect to Episode 1. This effect is simulated quite strongly by BouLac, which is also the scheme exhibiting the largest delay in the onset of the valley-exit wind, suggesting that the strong up-valley flow impedes the development of the nocturnal local circulation.

Figure 3.19 shows the diurnal evolution of both vertically-averaged temperature and pressure differences between the Bolzano basin and the Isarco Valley. The PBL schemes reproduce the wind reversal during the evening transition with a few hours of difference, related to the strength of the channelled up-valley flow. The nocturnal temperature differences are similar to Episode 1, leading to a comparable down-valley wind speed at the exit of the Isarco Valley (Figure 3.19d). Larger gradients are simulated during daytime, in particular by the BouLac scheme, as well as a stronger up-valley flow, further enhanced by the upper-level winds. The latter likely contributes to the delay between pressure gradient and wind reversal during the evening transition, which is larger than for Episode 1. Results from YSU simulation in Figure 3.20 show that, despite the synoptic wind being even weaker than in Episode 1 (Figures 3.10), its south-west direction during the afternoon may have favoured the channeling of the flow in the Isarco Valley (similar results were found for all simulations).

As for Episode 1, in Figure 3.21 we compare three vertical profiles of hourly averaged wind speed to better characterize the structure of the flow. Below 600 m AGL, the profile measured by the Lidar is very uniform and is preserved throughout the night. As for Episode 1, all schemes tend to reproduce a two-peak structure once the flow intensifies, which this time is instead not observed. The underestimation of wind speed

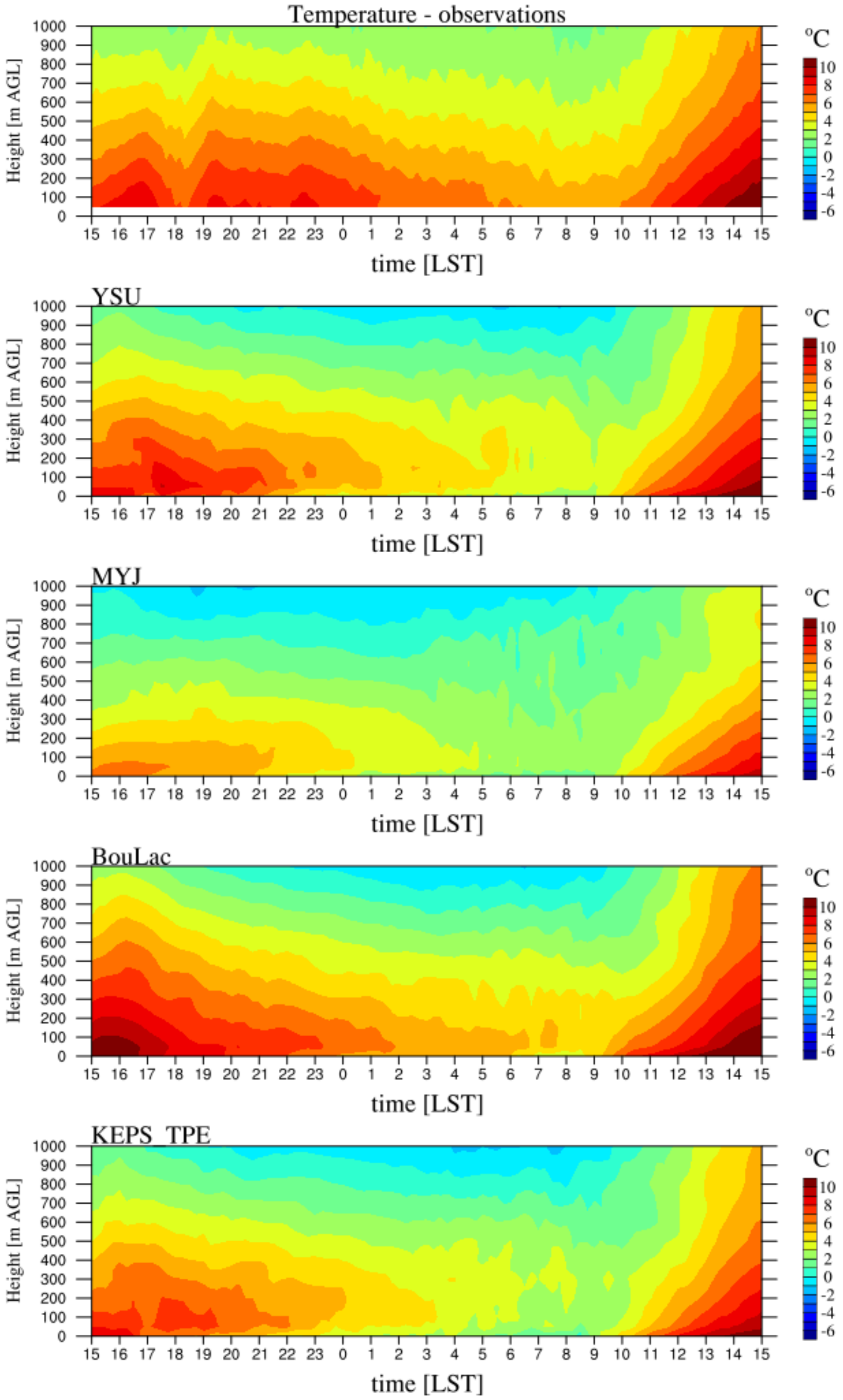

Figure 3.16: Time-height plots of temperature for Episode 2 at the site of the vertical profiler. Comparison between temperature profiler measurements (upper panel) and results from the four simulations, at the grid cell closest to the vertical profiler site in the inner domain.

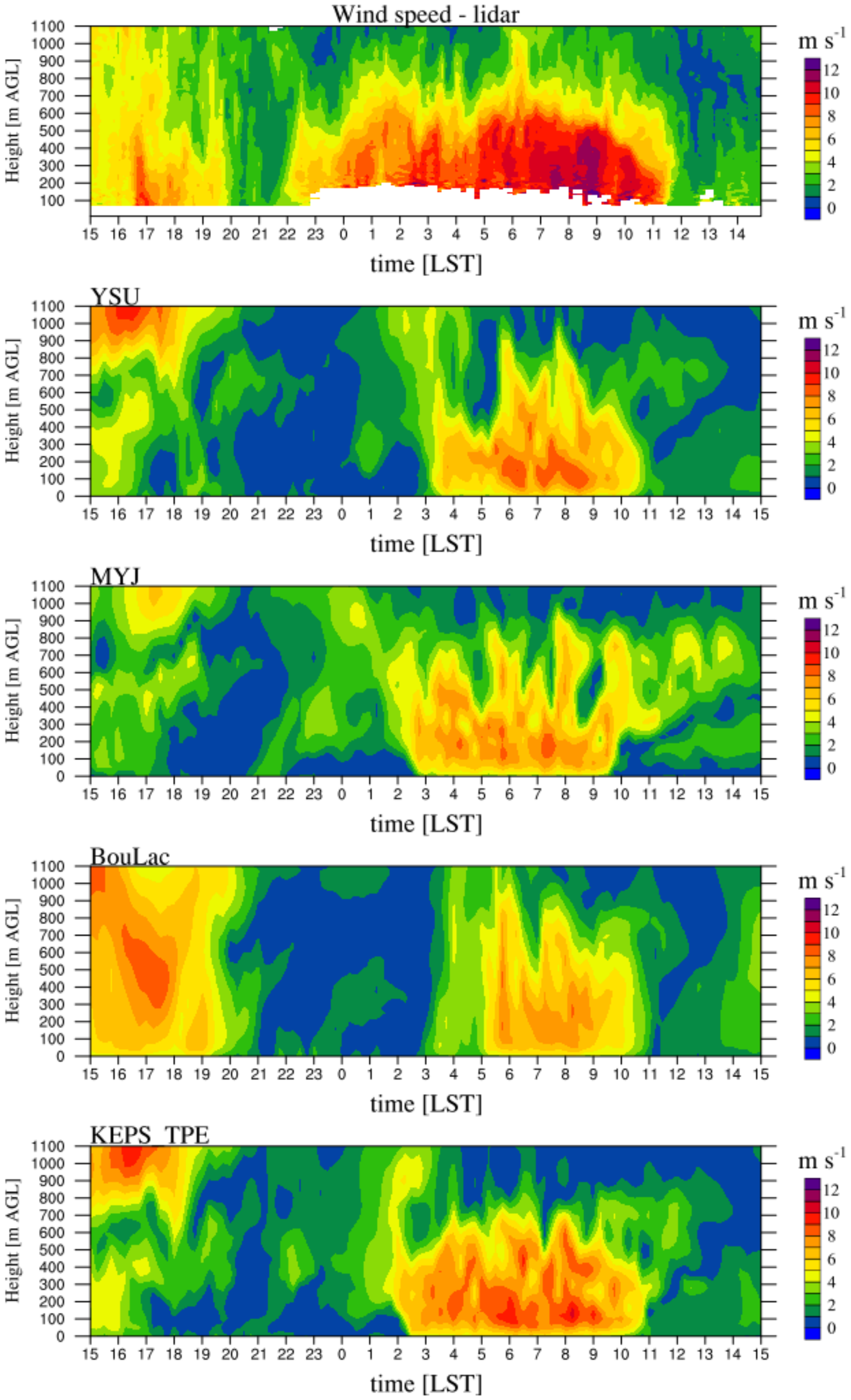

Figure 3.17: Time-height plots of wind speed for Episode 2 at the site of the Lidar. Comparison between wind speed from Lidar measurements (upper panel) and results from the four simulations, at the grid cell closest to the Lidar site in the inner domain.

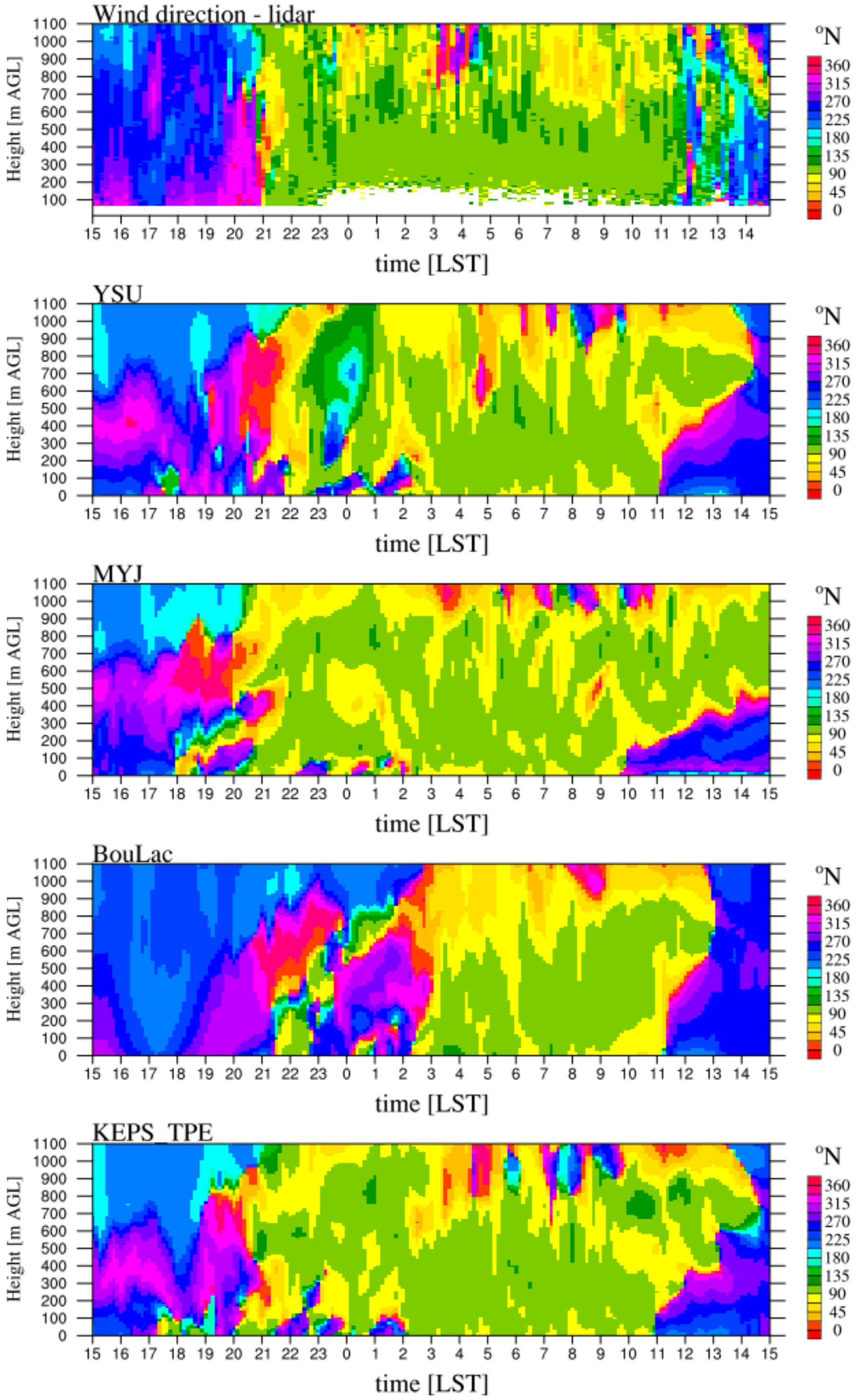

Figure 3.18: Time-height plots of wind direction for Episode 2 at the site of the Lidar. Comparison between wind direction from Lidar measurements (upper panel) and results from the four simulations, at the grid cell closest to the Lidar site in the inner domain.

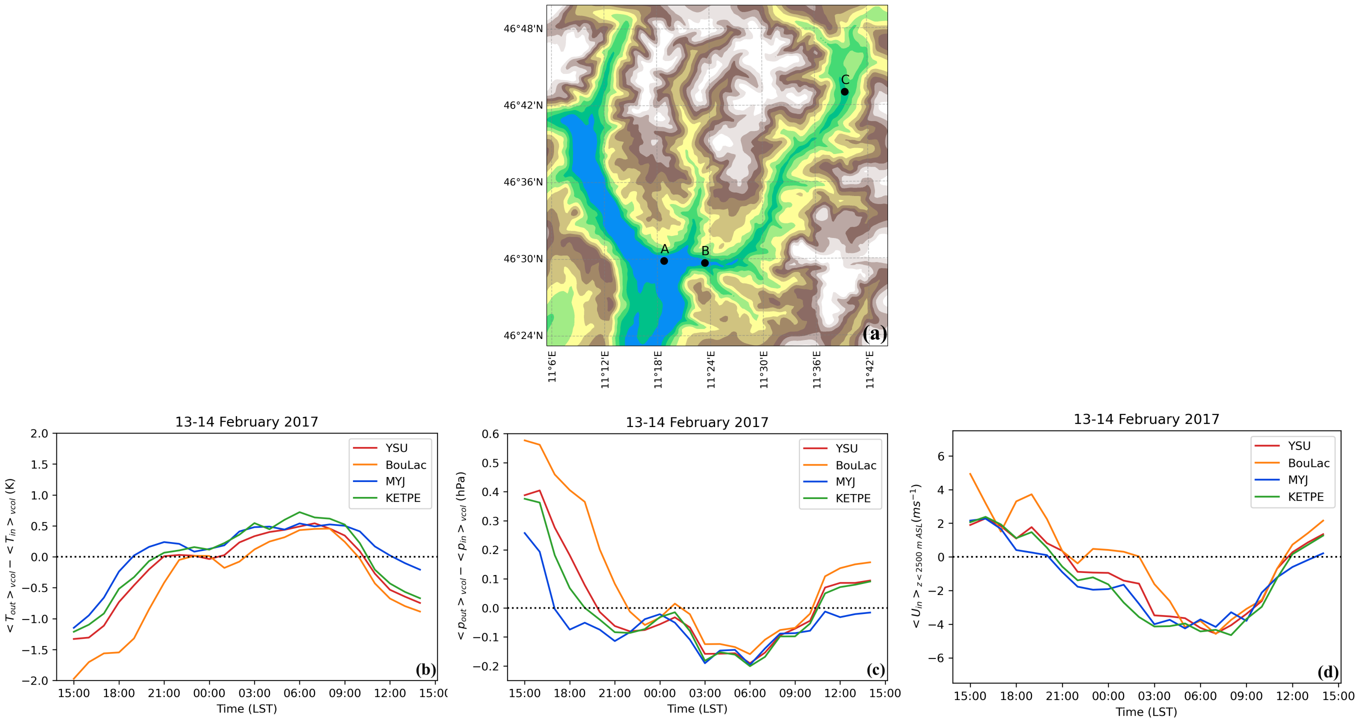

Figure 3.19: Time series for Episode 2 of the simulated vertically-averaged hourly temperature (b) and pressure (c) difference between the air columns, ranging from 600 m up to 2500 m a.s.l., at the grid cells corresponding to dots A and C in panel (a), representative of the Bolzano basin and the Isarco Valley. Panel d) shows the time series of the vertically-averaged U component of the wind at the exit of the Isarco Valley up to 2500 m a.s.l., evaluated at the grid cell corresponding to the dot B shown in panel (a).

at the exit of the Isarco Valley may be explained by a weaker temperature gradient in the simulations compared to observations, independently of the PBL scheme. Figure 3.16 showed a colder atmosphere in the Bolzano basin than observed, which reduces the temperature difference between the basin and the air inside the Isarco Valley. The presence of stratocumulus clouds over the basin, which are not exactly reproduced by the model, might be responsible for this temperature underestimation.

Figure 3.22 shows that the model, independently of the PBL scheme, well captures the interaction between the valley-exit wind and the lowest atmospheric layers in the Bolzano basin, which is opposite compared to Episode 1. In fact, all schemes reproduce a downward flow at the exit of the Isarco Valley when the drainage flow is blowing (although with a different onset for each PBL scheme), contrary to the upward motion of the previous case. As shown in Figure 3.23, displaying the vertical component of the wind velocity, vertically averaged from 400 m up to 1000 m a.s.l., a downward motion between 02:00 LST and 09:00 LST at the exit of the Isarco Valley corresponds to a drainage flow characterised by potentially colder air than the air in the basin. Since it can also happen that negative vertical velocities are present when the potential temperature in the Isarco Valley is higher than in the basin, it is likely that the sloping topography at the valley exit also plays a role.

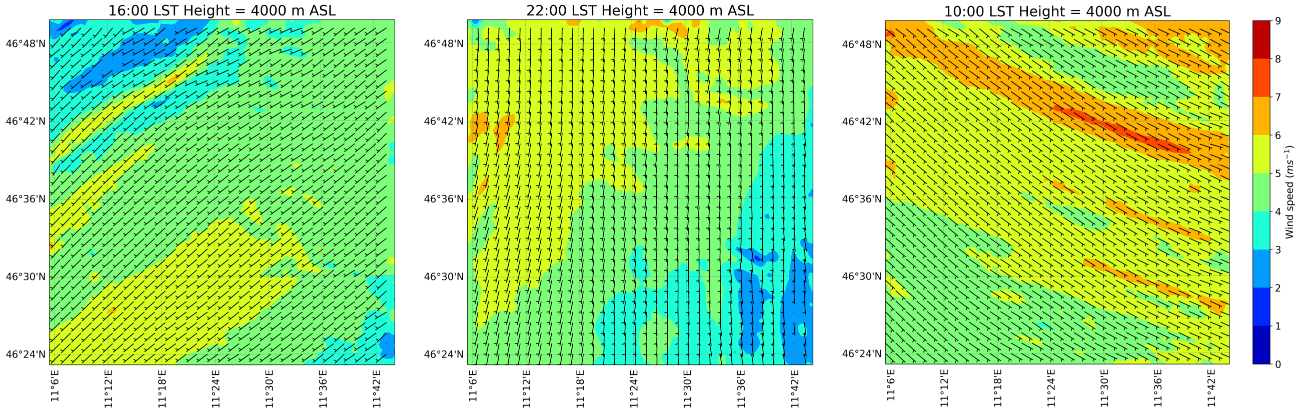

Figure 3.20: Wind speed and wind barbs at 4000 m a.s.l. from the YSU simulation at different hours.

Quantitative evaluation of model results

As for Episode 1, we proceed by comparing the ME and RMSE on an hourly basis, in order to have a quantitative evaluation of the model performance with the different PBL schemes. Results for the 11 GWSs are summarized in Table 3.3 and in Table 3.4 for 2-m temperature and 10-m wind speed, respectively.

In this case, a general underestimation of temperature is observed, and the best performing PBL scheme is BouLac, showing the lowest ME and RMSE at all GWSs except BS. ME is generally of the order of 1 °C for all the schemes, except for MYJ, characterized by an underestimation of about 2 °C. All the schemes strongly underestimate the temperature at Bolzano (BZ) GWS, where the largest underestimations are found. Bolzano is the largest urban site in the focus area (Pappaccogli et al., 2018) and this underestimation of temperature might be partly related to the phenomenon of the urban heat island (Giovannini et al., 2011), not well captured by the WRF model when an urban surface scheme is not used, as in this work. Analogous considerations can be drawn by comparing the RMSE values.

The ME of wind speed is quite small (generally less than 1 m s^{-1}), with little sensitivity to the choice of the PBL scheme. However, the BouLac scheme is, again, the one showing most often the lowest ME value. Considering the RMSE, MYJ shows the best performance, even if the variability between the different simulations is generally low also in this case.

Figure 3.24 shows the hourly times series of 2-m temperature and 10-m wind speed at the GWSs already selected for Episode 1. A systematic underestimation of temperature is observed for all PBL schemes, both during nighttime and daytime, with BouLac being always the one closest to observations. The largest bias occurs at Bolzano during nighttime, when the urban heat island should be stronger, thus corroborating the hypothesis that results at this site might be influenced by an incorrect representation of the effects of the city. In contrast to the other case study (Figure 3.14), a constant wind speed of 3 m s^{-1} is observed at Barbiano Colma during the night. This feature is properly reproduced by the model, and the choice of the PBL scheme mostly influences the time of the

#	GWS	Height	ME				RMSE			
	T2	(m a.s.l)	YSU	MYJ	BouLac	KEPS-TPE	YSU	MYJ	BouLac	KEPS-TPE
1	BR	226	-2.4	-3.8	**-1.1**	-3.0	2.6	3.8	**1.3**	3.2
2	BS	254	0.4	-1.3	1.4	**-0.3**	**1.1**	2.0	1.6	1.2
3	BZ	254	-2.7	-4.0	**-1.2**	-3.1	3.0	4.2	**1.4**	3.5
4	GZ	290	-1.9	-2.6	**-0.4**	-2.4	2.2	2.8	**1.3**	2.7
5	MR	330	-1.5	-2.7	**-0.8**	-2.0	1.9	3.0	**1.3**	2.3
6	BC	490	-1.0	-3.0	**-0.1**	-1.6	1.6	3.4	**1.1**	2.1
7	CL	495	-1.5	-3.1	**-0.9**	-2.0	1.8	3.3	**1.1**	2.2
8	FS	840	-0.9	-2.2	**-0.2**	-1.4	1.1	2.3	**0.6**	1.5
9	SR	970	-1.2	-2.2	**-0.7**	-1.4	1.8	2.5	**1.5**	2.0
10	SG	970	-1.0	-2.0	**-0.6**	-1.2	1.4	2.2	**1.2**	1.6
11	NP	1470	-0.5	-2.0	**0.3**	-0.8	1.7	2.3	**1.6**	2.0

Table 3.3: ME and RMSE for the 2-m temperature of the different simulations for Episode 2. Estimates are computed from hourly averages of GWS measurements and WRF outputs in the interval 13-02-2017 15:00 LST - 14-02-2017 18:00 LST.

#	GWS	Height	ME				RMSE			
	WS10	(m a.s.l)	YSU	MYJ	BouLac	KEPS-TPE	YSU	MYJ	BouLac	KEPS-TPE
1	BR	226	-0.7	-0.7	**0.4**	-0.9	1.5	1.7	**1.0**	1.7
2	BS	254	**-0.1**	-0.6	0.6	-0.2	1.3	1.2	1.3	**1.0**
3	BZ	254	-1.0	-1.6	**-0.8**	-1.0	2.1	2.3	2.0	**1.8**
4	GZ	290	0.4	0.4	0.4	**0.3**	0.7	0.7	0.9	0.7
5	MR	330	0.5	0.4	**0.3**	0.4	1.3	**0.7**	1.2	1.2
6	BC	490	1.0	**0.2**	1.2	1.1	1.9	**1.0**	2.3	1.6
7	CL	495	-0.6	-0.6	**-0.1**	-0.4	1.2	1.2	**1.0**	1.2
8	FS	840	**0.0***	-0.2	0.1	0.1	0.6	**0.5**	0.8	0.7
9	SR	970	-0.1	-0.5	0.1	-0.3	**0.9**	1.0	1.1	1.1
10	SG	970	0.4	**0.1**	0.5	0.4	0.7	**0.4**	0.8	0.7
11	NP	1470	0.2	0.1	0.2	0.1	0.8	0.8	1.0	0.8

Table 3.4: ME and RMSE for the 10-m wind speed of the different simulations for Episode 2. Estimates are computed from hourly averages of GWS measurements and WRF outputs in the interval 13-02-2017 15:00 LST - 14-02-2017 18:00 LST. The symbol * means |ME| or RMSE less than 0.05.

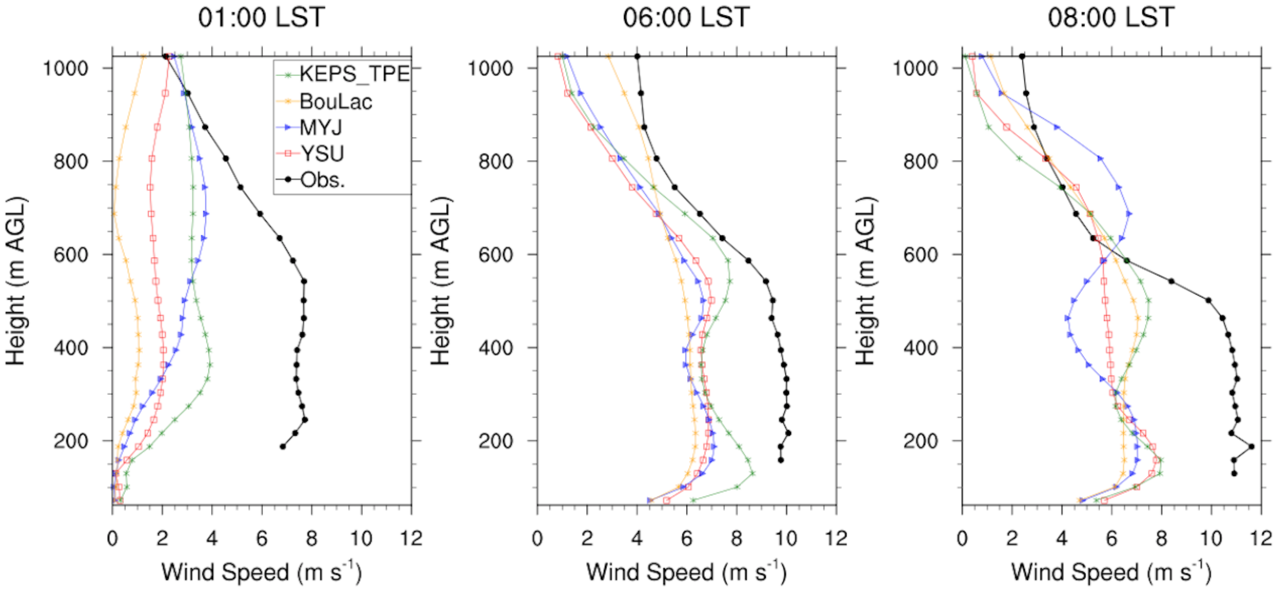

Figure 3.21: Vertical profiles of hourly averaged wind speed for Episode 2. Profiles from simulations are compared with observations at different hours of the night.

onset and the end of this drainage flow. An intense wind at the ground is also observed at Bolzano at the same time, which was not present in Episode 1, when a ground-based temperature inversion was well-developed in the basin. This feature is captured by YSU and KEPS-TPE, but with a shorter duration compared to observations. At Bronzolo wind speed is very weak during nighttime, thus suggesting that the wind observed at Bolzano is strongly related to the drainage flow of the Isarco Valley. At Bronzolo a peak in wind speed is, instead, observed during the afternoon, related to the strong up-valley flow of the Adige Valley, and correctly reproduced by the BouLac scheme. This corroborates the hypothesis of the occurrence of a channeling mechanism strengthening the up-valley flow in the Adige Valley. However, the comparison at Barbiano Colma shows that all schemes, except MYJ, tend to overestimate this effect on wind speed in the Isarco Valley. This explains the delay, compared to Lidar observations, in the onset of the valley-exit wind, observed in the simulations (Figure 3.17). Figure 3.25 shows a quantitative evaluation, in terms of ME and RMSE, of the performance of the different PBL schemes, referring to the vertical profile of temperature and wind speed measured by the profiler and the Lidar respectively, as done for Episode 1. A general underestimation of temperature is observed for all the simulations, coherently with the comparisons at the GWSs. BouLac results exhibit a very good agreement with observations up to 400 m AGL. In contrast, the wind speed predicted by the model using this scheme shows the largest negative bias, and the best agreement is obtained with KEPS-TPE. Results show low sensitivity to the PBL scheme regarding the vertical profile of ME and RMSE. In fact, all simulations tend to underestimate the wind speed, with a similar behaviour in the lower layers in all the PBL schemes. Comparing Figure 3.25 with Figure 3.21, this behaviour is related to the simulated vertical profiles displaying multiple peaks also in this case, instead of the uniform profile below 500 m AGL shown by the observations.

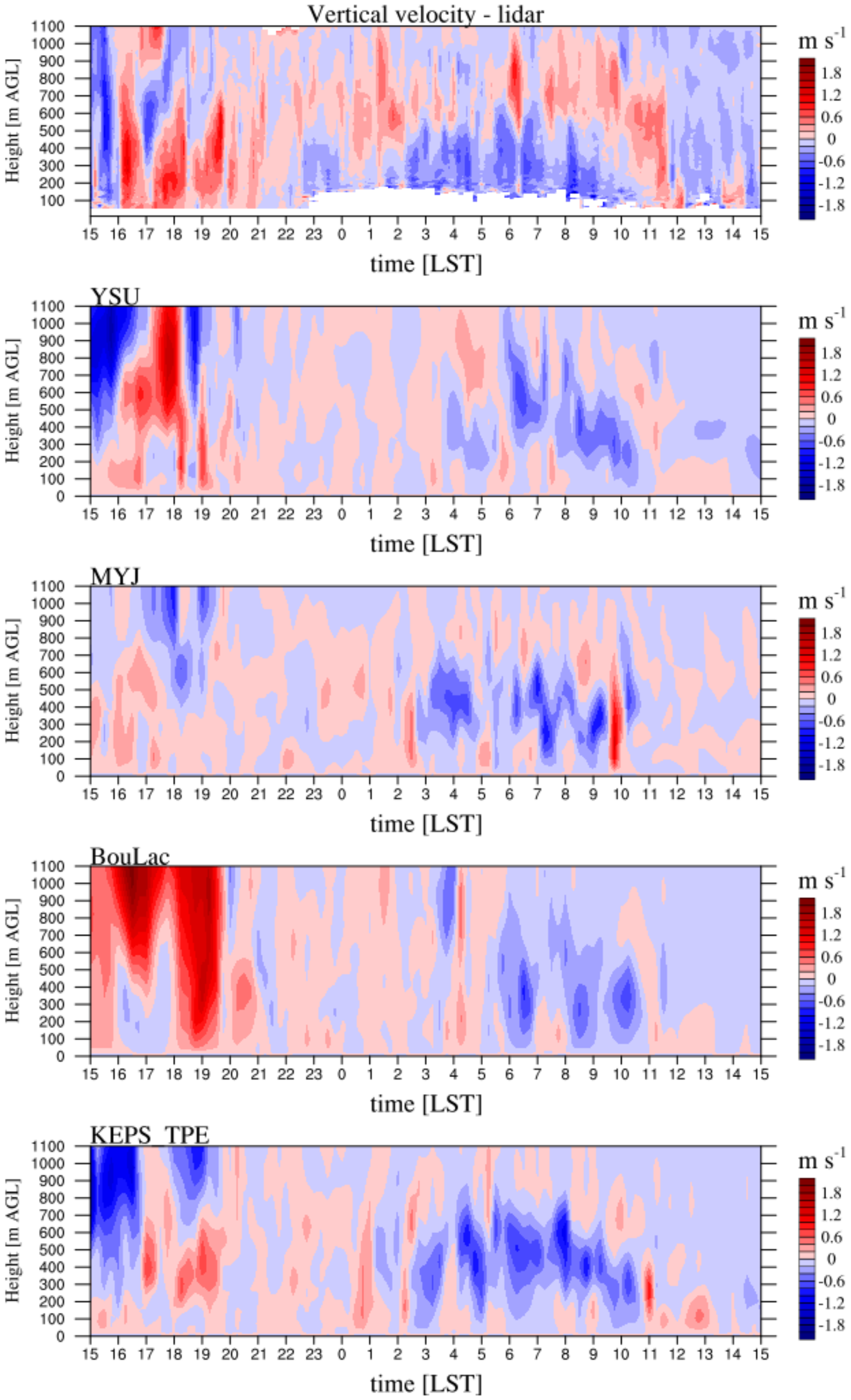

Vertical velocity - lidar

YSU

MYJ

BouLac

KEPS_TPE

Figure 3.22: Time-height plots of the vertical component of wind speed for Episode 2 at the site of the Lidar. Comparison between Lidar measurements and results from the four simulations, at the grid cell closest to the Lidar site in the inner domain.

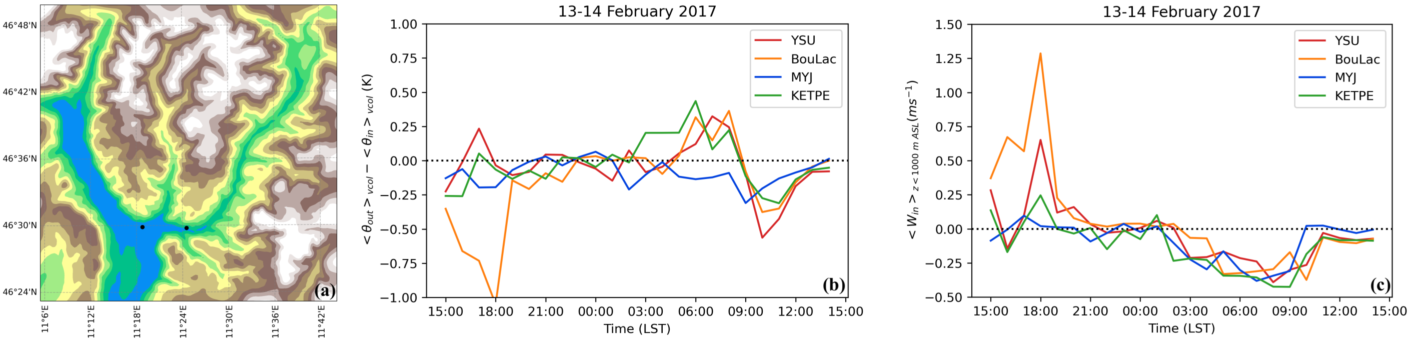

Figure 3.23: Time series for Episode 2 of the simulated vertically-averaged hourly potential temperature difference between the two air columns, ranging from 400 m up to 1000 m a.s.l., at the grid cells corresponding to the two points in panel (a), representative of the Bolzano basin and the exit of the Isarco Valley (b). Panel (c) shows vertical component of the wind reproduced by the model at the valley exit, vertically-averaged over an air column ranging from 400 m up to 1000 m a.s.l...

3.4.3 Spatial characteristics of the valley-exit wind and interaction with the CAP

After evaluating the performance of the four PBL schemes in the two case studies, we proceed by selecting one simulation for each case, in order to investigate in more detail the spatial characteristics of the flow exiting the Isarco Valley and its interaction with the air inside the Bolzano basin. While the overall model validation has shown that no PBL scheme is superior to the others, and they are all able to reproduce the main differences in the nocturnal circulation between the two case studies, it was found that MYJ underestimates the nocturnal thermally-driven forcing (Figure 3.9) in Episode 1 and the BouLac scheme strengthens the afternoon channeling mechanism in Episode 2 (Figure 3.19). Thus, they were not considered for the following analysis. We selected the YSU scheme for Episode 1 and the KEPS-TPE scheme for Episode 2. Both schemes were chosen because they were in good agreement with the Lidar observations, both for the horizontal (Figure 3.11,3.15 for Episode 1 and Figure 3.17,3.25 for Episode 2) and the vertical components of the wind velocity (Figure 3.12 for Episode 1 and Figure 3.22 for Episode 2). However, a different choice of the PBL scheme for the analysis presented in this section would not significantly change the conclusions, since the main features of the valley exit wind are rather well captured by all the simulations, and it would be redundant to show the following results for each PBL scheme. The present section aims at understanding the main physical mechanism in the evolution of the flow exiting the Isarco Valley into the Bolzano basin and highlighting the main differences between the two case studies, according to the stratification in the Bolzano basin. Thus, numerical simulations are here used as a tool for investigating these processes.

However, there are some advantages in using the schemes selected. An advantage of using the YSU scheme is its simplicity, as it can be easily modified for future investigations, for example implementing a stability varying Prandtl number, as done in Dimitrova et al. (2014), following the parameterization of Monti et al. (2002). Indeed,

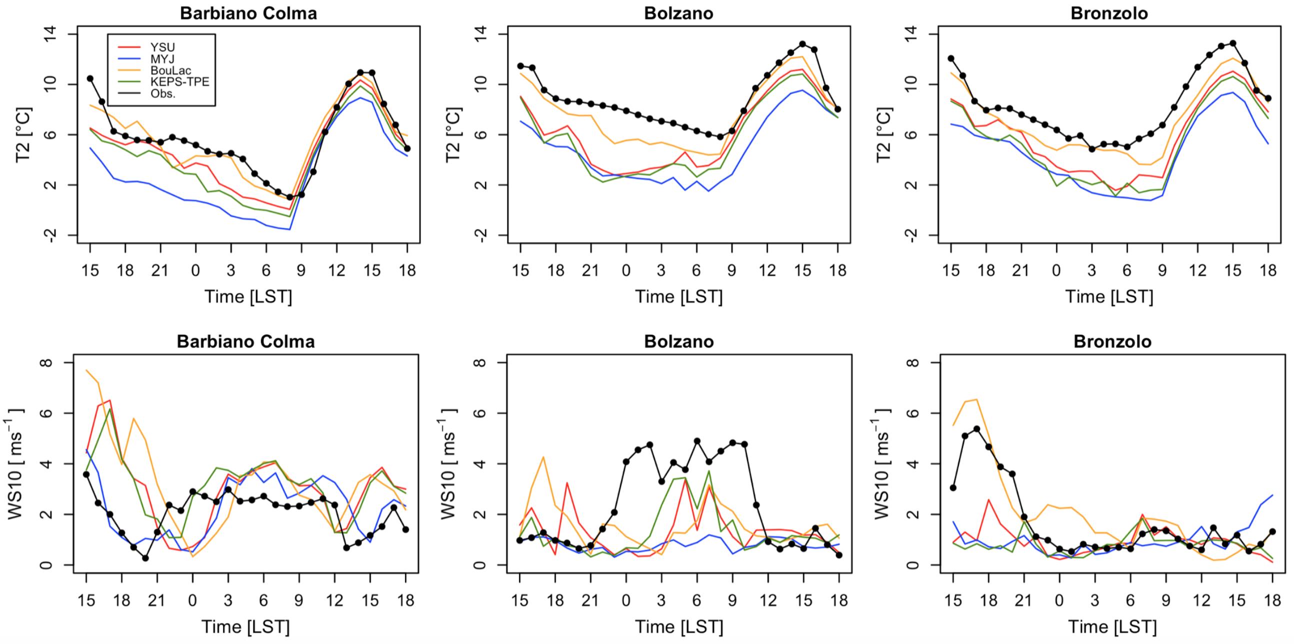

Figure 3.24: Hourly time series of 2-m temperature (upper panel) and 10-m wind speed (lower panel) at the GWSs of Barbiano Colma, Bolzano and Bronzolo from observations (black line and dots) and model results for Episode 2.

the default YSU scheme assumes identical profile functions for momentum and heat for stable conditions (except for the background offset in the implementation of eddy diffusivity). However, as described in Chapter 1, the efficiency of momentum transfer can be much larger than that of heat transfer in very stable conditions, due to internal wave contribution. Since observations seem to suggest that the latter occurs in the presence of the valley-exit flow, it would be interesting to compare results from simulations implementing default and modified versions of the YSU scheme.

In Episode 2, all schemes used cannot capture the maximum speed of the exit-flow, and its well-mixed structure. The latter evidence suggests that the modelled momentum eddy coefficients may be lower than in reality. Although this conclusion cannot be verified with the available observations, due to the lack of turbulence measurements, the KEPS-TPE is the only scheme including an additional mechanism for the increase of TKE in stable conditions (a prognostic equation for temperature variance, thus conversion of TPE to TKE through heat fluxes), which may imply a larger eddy viscosity (proportional to the TKE squared). This specific characteristic of the KEPS-TPE scheme also supported its choice for the following analysis of Episode 2. It is worth noting that standard k-ϵ models are widely used in engineering applications for neutrally stratified flows, for which they were primarily designed, and their extension to stratified flows may be quite tricky. However, the scheme used in this work was designed and positively tested also for stable conditions (Zonato et al., 2022). In fact, in addition to the temperature variance prognostic equation, it also includes a stability-dependent Prandtl number, based on the gradient Richardson number relation suggested by Zilitinkevich et al. (2008). Thus, it seems a valid option for further investigations of Episode 2. That

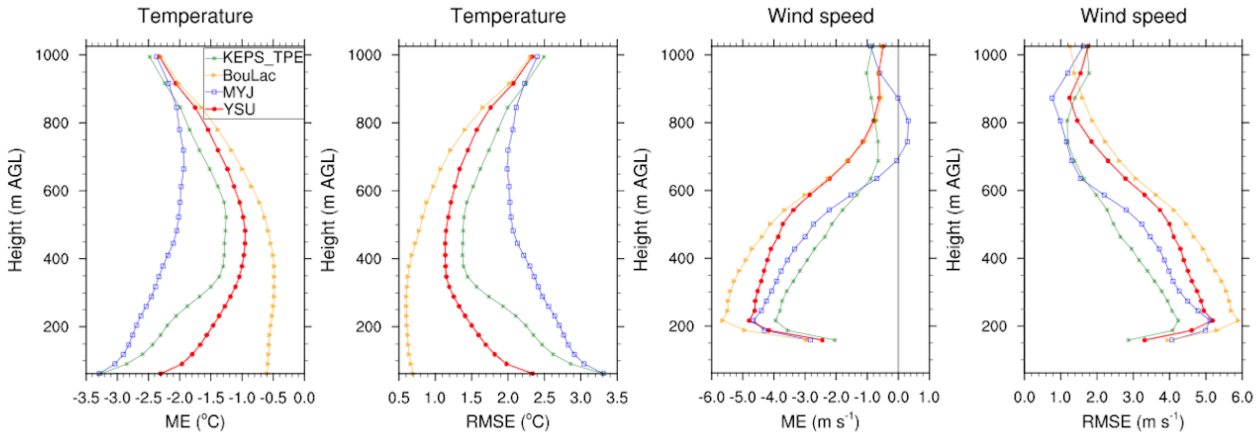

Figure 3.25: Average vertical profiles of ME and RMSE referring to the temperature measured by the profiler and the wind speed measured by the Lidar, evaluated from hourly averages from 14-02-2017 00:00 to 14-02-2017 12:00.

being said, the scheme assumes a constant proportionality between the mixing and dissipation length scales ($l_\epsilon = c_\mu^{-1} l_K = 0.09^{-1} l_K$), whereas a relation based on the mean strain rate may be more appropriate for large mean shears (Shih et al., 1995), as those associated with low-level jets. Also, dissipation lengths in stable conditions might be larger than mixing lengths due to the kinetic energy of wavy motion with little transfer to the smaller dissipative scales (Cuxart et al., 2006), and a constant proportionality between the two may not be advisable.

For Episode 1, Figure 3.26 shows horizontal cross-sections of the wind field at different hours of the night, at ∼700 m a.s.l. (top row) and 10 m AGL (bottom row). At ∼ 700 m a.s.l. the down-valley flow is clearly visible both in the Adige Valley and in the Isarco Valley (Figure 3.26a), with the latter characterized by larger wind speed in the lower part of the valley. During the night, the valley-exit flow intensifies and it is worth noting that, once in the basin, it veers southward before spreading horizontally in the Adige Valley (Figure 3.26b,c). On the other hand, light winds are observed at the ground, except in the last part of the Isarco Valley. Just below the valley exit, the 10-m wind speed abruptly decreases (Figures 3.26e,f), suggesting again a rising motion of the drainage flow once it merges with the potentially colder air in the basin. In order to better evaluate the spatial evolution of the flow along the Isarco Valley and in the Bolzano basin, Figure 3.27 shows vertical cross sections, along the black line in Figure 3.27a, of wind speed, parallel to the section (3.27b,e), potential temperature (3.27c,f) and vertical velocity (3.27d,g). In the first hours of the night, the down-valley flow (corresponding to negative values in Figure 3.27b) is weak and shallow, and uniformly developed. Throughout the night, its depth increases, and stronger velocities are simulated at the exit region of the valley (Figure 3.27e), with the development of an elevated flow over the basin and a descent of the down-valley flow around 1200 m a.s.l.. The cross-sections of potential temperature (Figure 3.27c,f) show that a CAP already formed at the beginning of the night, and that the Isarco Valley cools uniformly. In the morning, a strong CAP is present, with

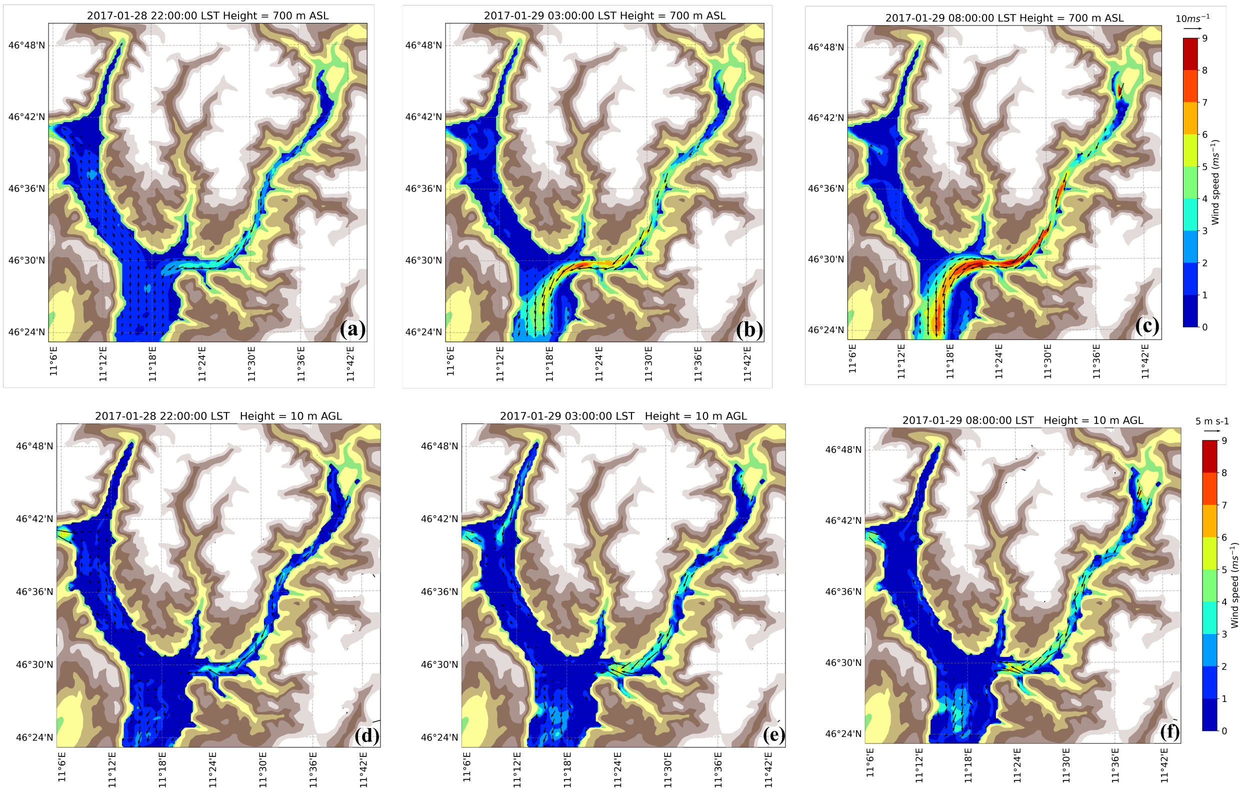

Figure 3.26: Horizontal cross-sections of hourly wind speed at 700 m a.s.l (a,b,c) and at 10 m AGL (d,e,f) for Episode 1, as reproduced by the YSU simulation at different hours.

a sharp change in potential temperature at the exit of the valley, where the wind speed showed a sharp weakening close to the ground (Figure 3.27e). In this area, at the same time, upward velocities are reproduced by the model over an atmospheric layer whose depth increases approaching the exit. Along the Isarco Valley, instead, upward and downward motions are mostly related to topographic features, which in turn influence the distribution of potential temperature, as at a distance of around 20 km from the exit (Figures 3.27f,g).

The same analysis is performed for Episode 2, as reproduced by the KEPS-TPE scheme, to highlight differences between the two case studies. The behaviour of the horizontal wind field at ~700 m a.s.l., shown in Figures 3.28a,b,c, is similar to Episode 1 (Figure 3.26) and it is worth noting that the down-valley flow of the Isarco Valley accelerates in the last part of the valley (Figures 3.28b,c), at the same point where the flow accelerates in Episode 1. A slower flow is simulated by the model, as well as a larger horizontal spread in the Adige Valley. At the ground, wind speeds similar to Episode 1 are reproduced by the model at the valley exit, but the exit wind propagates further in the basin, and then veers southward. This spatial picture of the flow is consistent with observations from the GWS at Bolzano, which measured near-surface winds of about 4 m s^{-1} for Episode 2 (Figure 3.24), but calm winds for Episode 1 (Figure 3.14). To further explain this feature, vertical-cross sections analogous to Figure 3.27 are shown in Figure 3.29. The initiation of the down-valley flow in the Isarco Valley occurs later than

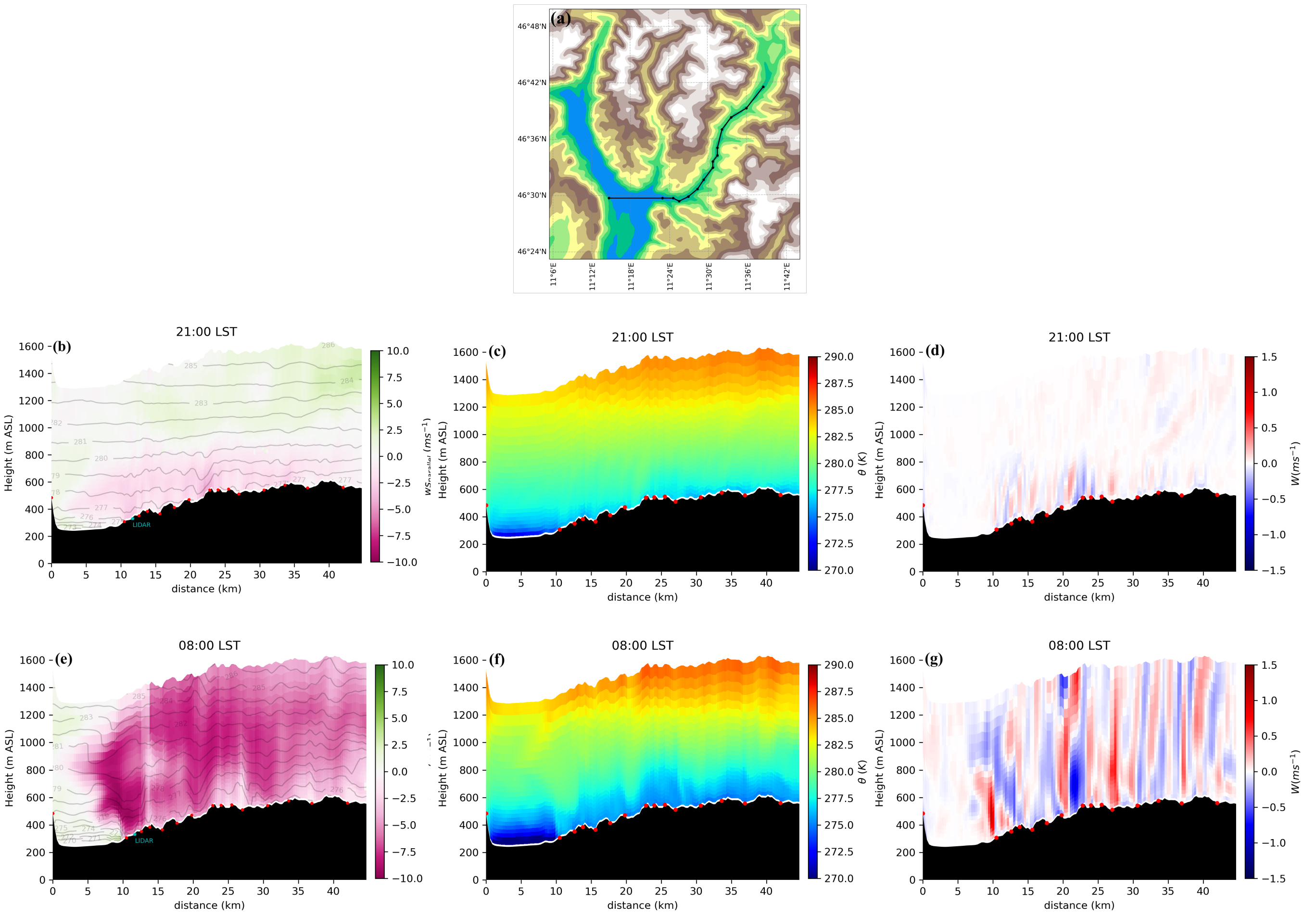

Figure 3.27: Vertical cross-sections from the YSU simulation at different hours along the Isarco Valley, following the black line in panel (a), for Episode 1. Panel (b) and (e) show the wind speed parallel to the cross-section plane (with negative values for down-valley flows), together with the potential temperature lines in grey. Panel (c) and (f) show the potential temperature and panel (d) and (g) show the vertical component of wind velocity. The terrain height is shown in black with the red points as delimiters between the different cross-sections.

in Episode 1, and the atmosphere is less stratified, as shown by wider-spaced isotherms in Figures 3.29a,d. Early in the morning, the down-valley flow has reached heights similar to Episode 1. The valley atmosphere has cooled less at the ground than in Episode 1 (Figure 3.29e) and isotherms are steep at the exit region, characterised by a downward motion, which brings potentially warmer air in the basin, as shown in Figure 3.29e,f, which is partially enhanced by the topography sloping towards the basin. Compared to vertical velocities of Figure 3.27f, in fact, a stronger vertical motion is produced by the model in Episode 2.

Both analyses show how the fields of potential temperature and wind speed are tightly related, and how the difference in potential temperature between the flow exiting the Isarco Valley and the atmosphere inside the basin plays a dominant role in driving

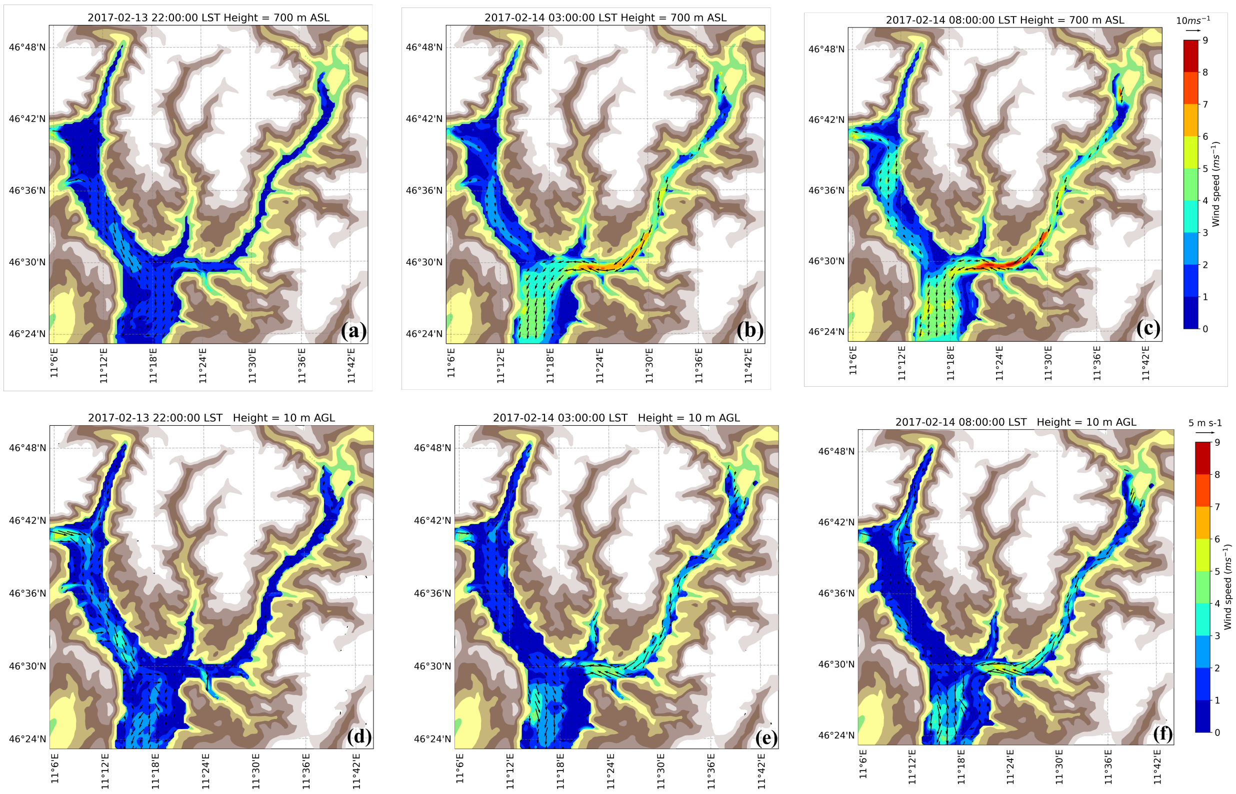

Figure 3.28: Horizontal cross-sections of hourly wind speed at 700 m a.s.l (a,b,c) and at 10 m AGL (d,e,f) for Episode 2, as reproduced by the KEPS-TPE simulation at different hours.

their interaction, influencing the vertical component of the wind field. The drainage flow is associated with higher potential temperature than the air inside the basin in Episode 1, while the opposite occurs in Episode 2, even if the temperature difference is much weaker in this case. This leads the drainage flow in Episode 1 to rise as it reaches the basin, suggesting that a strong CAP over the area may act as a downstream blocking for the flow. A similar behaviour was observed in the Colorado's Gore Valley, where an elevated jet was found where a topographic constriction at lower altitude caused pooling of air in the lowest atmospheric layers (Whiteman, 1990). This mechanism may have substantial influence on pollutant dispersion in the area during wintertime. In fact, even if the exit-flow is not able to penetrate the surface-based inversion layer and contribute to its erosion, as observed for other thermally-driven circulations in basins (Pinto et al., 2006), turbulence production by shear-instability at the interface between the two layers can lead to elevated mixing layers, promoting ventilation of pollutants from the cold pool through detrainment. Moreover, the cross-section in Figure 3.27g suggests that the oscillations in the values of the vertical velocity measured at the Lidar location (Figure 3.12) extend towards the basin, beyond the location where the flow rises over the cold pool. It is known that katabatic flows with a hydraulic jump (Yu and Cai, 2006) are sometimes followed by the excitation of trapped gravity waves downstream (Vignon et al., 2020), which propagate energy upwards away from the katabatic flow

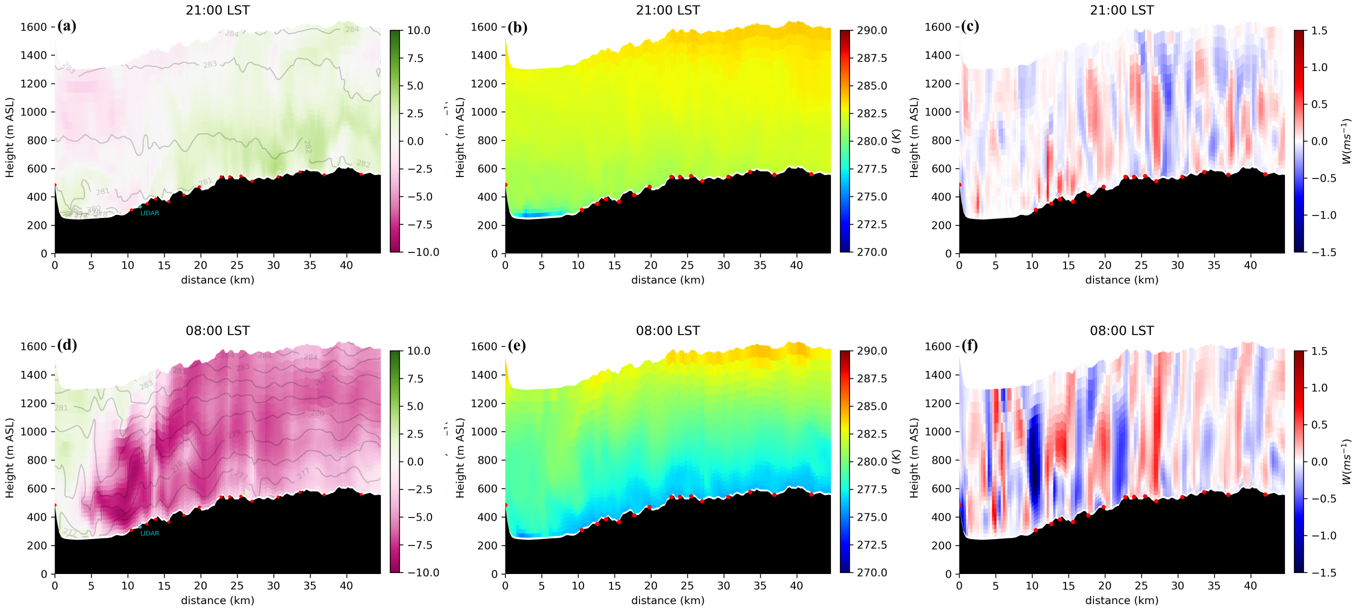

Figure 3.29: Vertical cross-sections from the KEPS-TPE simulation at different hours along the Isarco Valley, following the black line in Figure 3.27a, for Episode 2. Panel (a) and (d) show the wind speed parallel to the cross-section plane (with negative values for down-valley flows), together with the potential temperature lines in grey. Panel (b) and (e) show the potential temperature and panel (c) and (f) show the vertical component of wind velocity. The terrain height is shown in black with the red dots as delimiters between the different cross-sections.

jump (Renfrew, 2004). Even if there is no evidence of a hydraulic jump for Episode 1, it might be possible that these oscillations, and the one measured in time by the Lidar, are related to gravity waves driven by the forced ascent of the exit flow. However, this feature needs more investigations to be validated.

In order to highlight the spatial characteristics of the flow once it expands onto the basin, and when it attains the largest velocities (close to sunrise), Figure 3.30 shows the cross sections of the wind speed parallel to the section plane at 07:00 LST and 07:30 LST for Episode 1 and Episode 2, respectively. In the latter, the Lidar detected wind peaks up to $14\,\mathrm{m\,s^{-1}}$, while they were about $10\,\mathrm{m\,s^{-1}}$ in Episode 1. Figure 3.30 suggests that, when a strong ground-based temperature inversion does not develop in the basin, the air exiting the Isarco Valley sinks. This may lead to the conversion of potential energy into kinetic energy of the flow, thus explaining the larger wind speed observed in this case. Similar current collapses are associated with jets with a fan-shaped structure when viewed from above, as observed by Pamperin and Stilke (1985), Whiteman (1990), Jiménez et al. (2019) and predicted by specific 2D shallow-fluid models (Winstead and Young, 2000). On the contrary, according to this explanation, in Episode 1 part of the kinetic energy needs to be converted into potential energy, to lead the flow rising the cold pool, with a decrease in velocity.

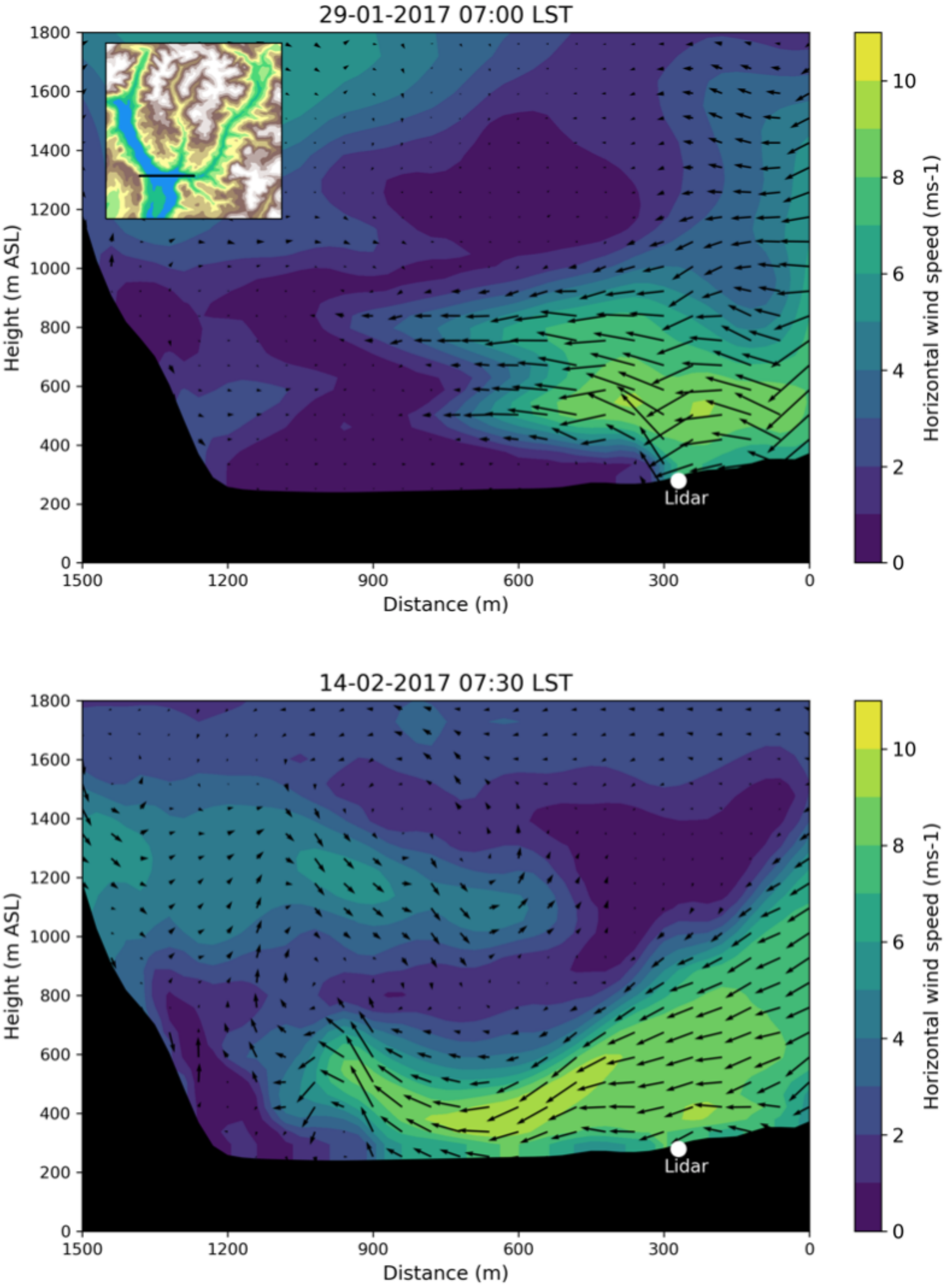

Figure 3.30: Cross sections of wind speed parallel to the section plane for the two case studies along the line shown in the insert map. The top panel refers to Episode 1 and it is extracted from the simulation with the YSU PBL scheme, while the bottom panel refers to Episode 2 and it is extracted from the simulation with the KEPS-TPE PBL scheme.

3.5 Conclusions

High-resolution numerical simulations ($\Delta \sim 300\,\mathrm{m}$) with the WRF model were performed to reproduce a valley-exit wind occurring in an area of the Adige Valley with a basin-like shape. It was observed that the thermal stratification in the basin strongly influences the flow once it reaches the area. In particular, two different wintertime case studies, with and without a strong ground-based temperature inversion, were investigated. The performance of four PBL schemes (YSU, MYJ, BouLac, KEPS-TPE) in reproducing the observed phenomena was evaluated, paying attention to their ability to represent the stable thermal stratification in the basin and the dynamical structure of the valley-exit wind, as well as their mutual interaction. Model results were compared to observational data from a wintertime field campaign in the Adige Valley. In particular, measurements from a thermal profiler and a Doppler wind Lidar were used, as well as 2-m temperature and 10-m wind speed provided by several GWSs on the valley floor and on the sidewalls.

Results indicate that the model is able to capture the main characteristics of this local circulation for both case studies, independently of the PBL scheme. Moreover, model results complement observations by providing a spatial overview of the flow and its spreading in the basin.

When a deep ground-based temperature inversion develops during nighttime, the thermal stratification is best captured by a PBL parameterization including, among others, a prognostic equation for temperature variance (KEPS-TPE, Zonato et al., 2022). On the other hand, it is found that the wind field is less sensitive to the choice of the PBL scheme, although a better performance is obtained with YSU. This scheme well captures the vertical profile of the flow in the lowest layers and its interaction with the atmosphere in the basin. In this case, an upward motion is observed at the Lidar location, followed by oscillations in the vertical component of wind velocity. This suggests that the valley-exit wind rises as it merges with the cold air inside the basin, which is supported by cross sections of wind field and potential temperature from numerical simulations.

When the thermal stratification in the basin is weaker during nighttime, all schemes reproduce quite well the vertical structure of the lower atmospheric layers. However, they tend to underestimate the overall temperature by 2-4 °C. This does not strongly affect the performance of the PBL schemes in capturing the evolution of the valley-exit wind, although a general underestimation of wind speed is observed. The best agreement with observations is obtained with KEPS-TPE. All schemes produce a delay in the onset of the valley-exit wind, which was attributed to a strong up-valley wind in the afternoon and lasting until evening. While observations suggested a channeling mechanism induced by the synoptic flow, the model tends to strengthen the effect on the local circulation. In this case, during the night, a downward motion at the Lidar location and strong 10-m wind speed at the GWSs along the path of the valley-exit wind are observed. This suggests that the flow stays close to the ground, which is supported by cross sections of wind speed from numerical simulations.

This work provides a better picture of a peculiar phenomenon of the local circulation in the Adige Valley in the Bolzano basin. However, similar flows at the exit of a narrow valley onto a wider adjacent area (Zängl, 2004; Jiménez et al., 2019), as well as drainage flow interaction with cold air inside a main valley (Neff and King, 1987, 1989; Pinto et al., 2006; Muoz et al., 2020), are observed in different locations worldwide. Thus, results from this work may be useful to interpret similar circulations at other locations.

Further investigations could aim at better understanding the impact of the exit-flow on turbulent vertical mixing over the area, for example by comparing cases with and without the arrival of an exit-flow in the basin, which would require a new ad-hoc field campaign including turbulence measurements. A recent study, in fact, suggests that the occurrence of a nocturnal LLJ influences the anisotropic characteristics of turbulence in the SBL (Lampert et al., 2016), by enhancing the damping of the vertical wind variance with respect to horizontal wind variances (on scales of a few hundred meters), usually observed after sunset close to the ground (Canut et al., 2016). The nocturnal LLJ is found to act as a source for turbulence in the horizontal direction, and when fully developed it drives the anisotropy ratio between horizontal and vertical variances to exceed 1. Two turbulent layers have been found in simulated nocturnal LLJs (Conangla and Cuxart, 2006; Haikin and Castelli, 2022), separated at the level of the wind maximum, with the upper layer characterized by stronger wind shear and weaker stratification, suggesting a dependence of the anisotropy ratio with height. It would be interesting to perform similar anisotropy analyses, but following the technique described in Chapter 2 based on the invariants of the Reynolds stress tensor, in order to investigate if these flows may also drive turbulence towards a particular limiting state of anisotropy, as observed for waves (Section 2.4.5). Recent numerical (Brun, 2017) and experimental (Charrondiére et al., 2020) studies adopted this technique for katabatic flows over steep slopes and they have found a decrease of turbulence anisotropy with height. Larger values of anisotropy were observed below the jet nose, with a tendency towards two-component turbulence, while isotropic turbulence was only reached as a trend in the outer-layer shear region, above the jet maximum (Brun, 2017). An increase of turbulence anisotropy with decreasing slope angle has been found by means of direct numerical simulations in the SBL, as a direct effect of stratification on vertical variance below the jet maximum (Giometto et al., 2017). Most surface flux parameterizations used in mesoscale models do not properly represent the turbulent heat fluxes in drainage-flow conditions also because of the nonlocal nature of turbulence generation (Pinto et al., 2006). These flows can propagate over large distances and have no relation with the local mean flow (Lang and Waite, 2019). If anisotropy properties of the Reynolds stress tensor, while computed locally, encode non-local influences on turbulence (as suggested by Stiperski and Calaf (2022)), classification of limiting states of anisotropy would be a way to improve parameterizations in such situations.

Finally, such a field campaign could give insights also on the oscillations which seem generated by the interaction of the valley-exit wind with the atmosphere in the basin. Several investigators have reported Kelvin-Helmholtz instability and waves within and atop accelerating flows in SBLs (Neff, 1988; Pinto et al., 2006; Viana et al., 2010; Wei et al., 2022). Waves might affect the turbulent mixing in the area, which is generally very low during wintertime, both through low-frequency modulation of turbulence, as shown in Chapter 2, or through turbulence generation by breaking waves. The intermittent nature of SBL turbulence is a challenge for current parameterizations (Vercauteren and

Klein, 2015; Boyko and Vercauteren, 2021; Calaf et al., 2022), however improvements are obtained when including the contribution of waves (Zilitinkevich et al., 2007, 2009; Kleeorin et al., 2019).

Finally, additional investigations might also include simulations with the adoption of an urban surface scheme to better represent the thermal stratification in the basin, which is heavily urbanized, even if we expect that this aspect may locally control the penetration of the valley-exit wind in the urban area, but not the overall interaction between the valley-exit wind and the air in the basin. Both studies would provide a comprehensive understanding of the phenomenon, and could be used to improve air-quality forecasts during wintertime in this urban basin.

Chapter 4

Conclusions and perspectives

The work reported in this thesis investigated stably stratified atmospheric boundary layer flows, with a main focus on turbulence and submeso motions, such as drainage flows and internal gravity waves. SBL flows pose many challenges both from a practical point of view, such as a proper interpretation of field measurements and a proper representation in numerical models, and from a theoretical point of view. Indeed, fundamental features of the SBL still remain not well understood (Mahrt, 2014). The hybrid nature of the problem led this work to have a hybrid structure as well.

An extensive literature review, in part presented in Chapter 1 and in part in the Introduction of Chapter 2, has shown how classical concepts in turbulence theory for the atmospheric boundary layer are not well suited for the SBL. The overlap of scales between turbulent and non-turbulent motions, and their mutual interaction, is not accounted for in commonly used PBL parameterizations, and should be explicitly resolved by numerical models. In particular, closure schemes assume the mean flow perturbations to arise due to PBL turbulence only, while the SBL is characterised by many non-turbulent motions, which can be ephemeral in time and thus are not well represented by traditional averaging procedures. A recent review about the impact of transient unresolved motions in NWP models has proposed a triple decomposition of flow variables, that allows for submeso motions to be considered in the equations of the mean state (Calaf et al., 2022).

In Chapter 2, the analysis of SnoHATS data has shown the influence of internal gravity waves on stably stratified turbulence, and how the Reynolds averaging technique to define turbulent quantities may include non-turbulent contribution, leading to incorrect conclusions about turbulence in the SBL. The anisotropy analysis of the Reynolds stress tensor was found to be quite sensitive to the presence of propagating wavelike structures in the airflow, characterised by a one-component signature. The ratio between the period of a possible wave passing through the sensor and the time-average used to compute Reynolds stresses played a crucial role. Waves with periods smaller than the time-average were found to contribute in driving the Reynolds stress tensor towards the one-component limit. Since wave motions are nonlocal, results corroborated previous findings that the Reynolds stress tensor, even if calculated locally, may encode the information about nonlocal processes (Stiperski et al., 2021), missing in classic similarity scalings and often invoked to explain their breakdown. Thus, including scaling parameters which take into account anisotropy is a promising approach to improve near-surface similarity scaling used in numerical modeling of weather and climate (Stiperski and Calaf, 2022). However, this might be also a way to improve parameterizations of turbulence in the SBL. In the current framework of turbulence closure it is unclear whether the mixing length can be extended to include some of the wave effects. So far, very little has been done to define a mixing length in turbulence closure that includes both turbulence and wave motions in the SBL (Sun et al., 2015a). For future studies, it would thus be interesting to investigate if and how new parameters, taking into account anisotropy, may be included in the definition of mixing lengths. More generally, multiple length scales, derived from the full anisotropy tensor, might also provide directions on how to differentiate horizontal and vertical eddy coefficients with an approach directly linking one to the other.

The SnoHATS data analysis also showed that over areas where katabatic flows are likely to occur, an increase of the Brunt-Väisälä frequency with wind speed is observed. This regime is characterized by a large occurrence of one-component states. In future studies, it would be interesting to further investigate this feature, to get a deeper understanding of this counter-intuitive increase of atmospheric stability with wind speed. In particular, it would be interesting to explore the link with internal gravity waves, which can be generated by the outbreak of drainage flows, as it has been explored in other studies (Chemel et al., 2009; Viana et al., 2010).

In Chapter 1, it has also been discussed how the occurrence of drainage flows, besides contributing to the generation of waves, which in turn may affect turbulence in the SBL, directly favours the departure of turbulence features from those reported over flat terrain regions. For example, strong horizontal gradients in wind speed are associated with nocturnal valley-exit jets (Serafin et al., 2018), which may enhance horizontal turbulent mixing by shear production (Weigel and Rotach, 2004; Goger et al., 2019), and contribute to turbulence anisotropy (Lampert et al., 2016). The dynamics of the SBL over complex terrain becomes more complicated, and its description would benefit from research attempts trying to relate the anisotropy to terrain features (Stiperski et al., 2019; Stiperski and Calaf, 2022), in order to identify turbulence properties that are common to any complex terrain site. Also, an extension of PBL parameterizations from 1D to 3D schemes was discussed in Chapter 1 as a direction to improve the performance of NWP models over complex terrain. In fact, in addition to vertical mixing, they would account for horizontal mixing by including the horizontal gradients of mean quantities in the equations for turbulence closure, thus better reproducing turbulence over complex terrain, such as that generated by flows with strong horizontal gradients in wind speed (e.g. valley-exit jet). In this framework, the last part of the thesis focused on numerical simulations and standard PBL parameterizations, assessing the ability of the WRF model to reproduce a drainage flow in the Alpine region, with characteristics similar to a nocturnal valley-exit jet. In particular, the analysis presented in Chapter 3 has shown how stratified atmospheric conditions over mountainous terrain, combined with thermally-driven circulations under weak synoptic forcing, may lead to complex local circulations. Specific features of these circulations in an Alpine basin, by comparing cases with and without the formation of a cold pool in the basin, were investigated. High-resolution mesoscale simulations were able to reproduce the main characteristics of the interaction between a valley-exit wind and the air inside the basin, independently of the PBL scheme. The model showed a down-valley flow reaching maximum wind speed near the exit region, and well captured the larger velocity, especially in the lowest atmospheric layers, observed if a cold pool was not present. In this case, the flow blew close to the ground, otherwise, an elevated valley-exit flow developed, rising near the valley exit region where the two air masses merged. A general underestimation of wind speed in the lowest atmospheric layers was observed, which in some cases was attributed to a lower horizontal pressure gradient between the valley and the basin reproduced by the model. Further investigations, with the support of turbulence measurements, may help understanding if some turbulence characteristics are misrepresented by the PBL scheme, while being important to better reproduce the intensity of the flow. The influence of low-level jets on turbulence generation and anisotropy has been discussed in general, but it would be an interesting analysis to develop for having a comprehensive view of the flow and a better understanding of the results. All PBL schemes produced a shallower cold pool, however a partial improvement was observed with a PBL scheme (KEPS-TPE) including an additional prognostic equation for temperature variance, thus accounting for conversion of TPE into TKE in stably stratified conditions. This result brings up the question of how more advanced classes of turbulence models, which have proven themselves in engineering applications, perform when applied to the atmosphere. For example, there are models which consider (simplified) transport equations for all components of the Reynolds stress tensor, as well as for the turbulent heat fluxes, to derive algebraic equations for them. They seem a priori to suit well for stably stratified flows, as they account for the coupling between the Reynolds stresses and the heat fluxes through the buoyancy terms. However, besides the issue of proper modelling the new unknown correlation terms (most notably the pressure-redistribution terms), there is a need to evaluate if these models go beyond the computational limitations of climate and NWP models, and if so, to quantify the benefits with respect to simpler models. Moreover, including more Reynolds-averaged equations without a deep understanding of their interaction, does not always guarantee a better agreement with observations. This is the case of algebraic models which still predict in stable condition a finite critical Richardson number beyond which turbulence ceases to exist (Lazeroms et al., 2016), which is not validated by observations, as extensively discussed in Chapter 1. Cheng et al. (2020) were able to overcome this problem only trough an accurate investigation of the equations, by identifying the cause of a finite critical Ri in the momentum flux terms in the heat flux equations and working to avoid that. Finally, in some cases, specific physics need to be added ad-hoc in the Reynolds-averaged equations to improve the results, such as the internal waves contribution to the vertical momentum transport in stable conditions. In particular, the latter aspect would be of interest for possible improvements of the KEPS-TPE scheme used in Chapter 3 in reproducing the nocturnal flow in the basin. An oscillating behaviour was observed in the vertical velocity, which was partially captured by the model. If wave-like structures are generated, these might affect the turbulent mixing inside the basin and further investigations of this phenomenon may give insights on how to include these effects in PBL parameterizations.

Bibliography

Acevedo, O. C., Costa, F. D., Maroneze, R., Carvalho, A. D., Puhales, F. S., and Oliveira, P. E. (2021). External controls on the transition between stable boundary-layer turbulence regimes. Quarterly Journal of the Royal Meteorological Society, 147:2335–2351.

Ali, N., Hamilton, N., Cortina, G., Calaf, M., and Cal, R. B. (2018). Anisotropy stress invariants of thermally stratified wind turbine array boundary layers using large eddy simulations. Journal of Renewable and Sustainable Energy, 10.

Alisse, J.-R. and Sidi, C. (2000). Experimental probability density functions of small-scale fluctuations in the stably stratified atmosphere. Journal of Fluid Mechanics, 402:137â162.

Aluie, H., Hecht, M., and Vallis, G. K. (2018). Mapping the energy cascade in the North Atlantic Ocean: The coarse-graining approach. Journal of Physical Oceanography, 48:225–244.

Arduini, G., Staquet, C., and Chemel, C. (2016). Interactions Between the Nighttime Valley-Wind System and a Developing Cold-Air Pool. Boundary-Layer Meteorology, 161:49–72.

Atta, C. V. (1991). Local isotropy of the Smallest Scales of Turbulent Scalar and Velocity Fields. Proceedings: Mathematical and Physical Sciences, 434:139–147.

Baas, P., van de Wiel, B. J., van Meijgaard, E., Vignon, E., Genthon, C., van der Linden, S. J., and de Roode, S. R. (2019). Transitions in the wintertime near-surface temperature inversion at Dome C, Antarctica. Quarterly Journal of the Royal Meteorological Society, 145:930–946.

Banerjee, S., Krahl, R., Durst, F., and Zenger, C. (2007). Presentation of anisotropy properties of turbulence, invariants versus eigenvalue approaches. Journal of Turbulence, 8:1–27.

Banta, R. M., Darby, L. S., Fast, J. D., Pinto, J. O., David, C., Shaw, W. J., and Orr, B. W. (2004). Nocturnal Low-Level Jet in a Mountain Basin Complex. Part I: Evolution and Effects on Local Flows. Journal of Applied Meteorology, 43:1348–1365.

Banta, R. M. and Gannon, P. T. (1995). Influence of soil moisture on simulations of katabatic flow. Theoretical and Applied Climatology, 52:85–94.

Banta, R. M., Mahrt, L., Vickers, D., Sun, J., Balsley, B. B., Pichugina, Y. L., and Williams, E. J. (2007). The very stable boundary layer on nights with weak low-level jets. Journal of the Atmospheric Sciences, 64:3068–3090.

Banta, R. M., Olivier, L. D., Gudiksen, P. H., and Lange, R. (1996). Implications of Small-Scale Flow Features to Modeling Dispersion over Complex Terrain. Journal of Applied Meteorology and Climatology, 35:330 – 342.

Banta, R. M., Pichugina, Y. L., and Newsom, R. K. (2003). Relationship between low-level jet properties and turbulence kinetic energy in the nocturnal stable boundary layer. Journal of the Atmospheric Sciences, 60:2549–2555.

Basu, S., Holtslag, A. A., Caporaso, L., Riccio, A., and Steeneveld, G. J. (2014). Observational Support for the Stability Dependence of the Bulk Richardson Number Across the Stable Boundary Layer. Boundary-Layer Meteorology, 150:515–523.

Batchelor, G. K. (1953). The conditions for dynamical similarity of motions of a frictionless perfect-gas atmosphere. Quarterly Journal of the Royal Meteorological Society, 79:224–235.

Berner, J., Achatz, U., Batté, L., Bengtsson, L., Cámara, A. D. L., Christensen, H. M., Colangeli, M., Coleman, D. R., Crommelin, D., Dolaptchiev, S. I., Franzke, C. L., Friederichs, P., Imkeller, P., Järvinen, H., Juricke, S., Kitsios, V., Lott, F., Lucarini, V., Mahajaajaajan, S., Palmer, T. N., Penland, C., Sakradzijaja, M., Storch, J. S. V., Weisheimer, A., Weniger, M., Williams, P. D., and Yano, J. I. (2017). Stochastic parameterization toward a new view of weather and climate models. Bulletin of the American Meteorological Society, 98:565–587.

Billant, P. and Chomaz, J. M. (2000). Experimental evidence for a new instability of a vertical columnar vortex pair in a strongly stratified fluid. Journal of Fluid Mechanics, 418:167–188.

Bisignano, A., Carotenuto, F., Zaldei, A., and Giovannini, L. (2022). Field calibration of a low-cost sensors network to assess traffic-related air pollution along the Brenner highway. Atmospheric Environment, 275:119008.

Boffetta, G. and Ecke, R. E. (2011). Two-dimensional turbulence. Annual Review of Fluid Mechanics, 44:427–451.

Bolgiano, R. (1959). Turbulent Spectra in a Stably Stratified Atmosphere. Journal of Geophysical Research, 64:2226–2229.

Bou-Zeid, E., Higgins, C., Huwald, H., Meneveau, C., and Parlange, M. B. (2010). Field study of the dynamics and modelling of subgrid-scale turbulence in a stable atmospheric surface layer over a glacier. Journal of Fluid Mechanics, 665:480–515.

Bougeault, P. and Lacarrére, P. (1989). Parameterization of Orography-Induced Turbulence in a MesobetaâScale Model. Monthly Weather Review, 117:1872 – 1890.

Boussinesq, J. V. (1877). Essai sur la théorie des eaux courantes.Mémoires présentés par divers savants á l'Académie des Sciences XXIII.

Boyko, V. and Vercauteren, N. (2021). Multiscale Shear Forcing of Turbulence in the Nocturnal Boundary Layer: A Statistical Analysis. Boundary-Layer Meteorology, 179:43–72.

Brun, C. (2017). Large-Eddy Simulation of a katabatic jet along a convexly curved slope: 2. Evidence of Görtler vortices. Journal of Geophysical Research, 122:5190–5210.

Brun, C., Friedrich, R., and Silva, C. B. D. (2006). A non-linear SGS model based on the spatial velocity increment : Application to LES of fully developed pipe flow and round turbulent jet. Theoretical and Computational Fluid Dynamics, 20:1–21.

Calaf, M., Vercauteren, N., Katul, G. G., Giometto, M. G., Morrison, T. J., Margairaz, F., Boyko, V., and Pardyjak, E. R. (2022). Boundary-Layer Processes Hindering Contemporary Numerical Weather Prediction Models. Boundary-Layer Meteorology.

Callies, J., Ferrari, R., and Bühler, O. (2014). Transition from geostrophic turbulence to inertia-gravity waves in the atmospheric energy spectrum. Proceedings of the National Academy of Sciences of the United States of America, 111:17033–17038.

Canut, G., Couvreux, F., Lothon, M., Legain, D., Piguet, B., Lampert, A., and Moulin, E. (2016). Turbulence measurements with a tethered balloon. Atmospheric Measurement Techniques Discussions.

Canuto, V. M., Cheng, Y., Howard, A. M., and Esau, I. N. (2008). Stably stratified flows: A model with no Ri(cr). Journal of the Atmospheric Sciences, 65:2437–2447.

Carper, M. A. and Porté-Agel, F. (2004). The role of coherent structures in subfilter-scale dissipation of turbulence measured in the atmospheric surface layer. Journal of Turbulence, 5.

Cava, D., Giostra, U., and Katul, G. (2015). Characteristics of gravity waves over an Antarctic Ice sheet during an Austral Summer. Atmosphere, 6:1271–1289.

Cava, D., Giostra, U., Siqueira, M., and Katul, G. (2004). Organised motion and radiative perturbations in the nocturnal canopy sublayer above an even-aged pine forest. Boundary-Layer Meteorology, 112:129–157.

Cava, D., Mortarini, L., Giostra, U., Acevedo, O., and Katul, G. (2019). Submeso motions and intermittent turbulence across a nocturnal low-level jet: A self-organized criticality analogy. Boundary-Layer Meteorology.

Charrondière, C., Brun, C., Cohard, J., Sicart, J., Obligado, M., Biron, R., and Coulaud, C. Guyard, H. (2022). Katabatic Winds over Steep Slopes: Overview of a Field Experiment Designed to Investigate Slope-Normal Velocity and Near-Surface turbulence. Boundary-Layer Meteorology, 182:29–54.

Charrondiére, C., Brun, C., Sicart, J. E., Cohard, J. M., Biron, R., and Blein, S. (2020). Buoyancy effects in the Turbulence Kinetic Energy Budget and Reynolds Stress Budget for a Katabatic Jet over a Steep Alpine Slope. Boundary-Layer Meteorology, 177:97–122.

Chemel, C., Staquet, C., and Y, L. (2009). Generation of internal gravity waves by a katabatic wind in an idealized alpine valley. Meteorology and Atmospheric Physics, 103:187–194.

Chen, C. J. (2013). Lectures on Turbulent Flows. Description of Turbulence and Flow Transition (video: min 7:23).

Cheng, Y., Canuto, V. M., Howard, A. M., Ackerman, A. S., Kelley, M., Fridlind, A. M., Schmidt, G. A., Yao, M. S., Genio, A. D., and Elsaesser, G. S. (2020). A Second-Order Closure Turbulence Model: New Heat Flux Equations and No Critical Richardson Number. Journal of the Atmospheric Sciences, 77:2943–2959.

Cheng, Y., Sayde, C., Li, Q., Basara, J., Selker, J., Tanner, E., and Gentine, P. (2017). Failure of Taylor's hypothesis in the atmospheric surface layer and its correction for eddy-covariance measurements. Geophysical Research Letters, 44:4287–4295.

Chow, K. F., Weigel, A. P., Street, R. L., Rotach, M. W., and Xue, M. (2006). High-Resolution Large-Eddy Simulations of Flow in a Steep Alpine Valley. Part I: Methodology, Verification, and Sensitivity Experiments. Journal of Applied Meteorology and Climatology.

Chowdhuri, S., Kumar, S., and Banerjee, T. (2020). Revisiting the role of intermittent heat transport towards Reynolds stress anisotropy in convective turbulence. Journal of Fluid Mechanics.

Chrust, M. F., Whiteman, C. D., and Hoch, S. W. (2013). Observations of thermally driven wind jets at the exit of Weber Canyon, Utah. Journal of Applied Meteorology and Climatology, 52:1187–1200.

Cohen, A. E., Cavallo, S. M., Coniglio, M. C., and Brooks, H. E. (2015). A review of planetary boundary layer parameterization schemes and their sensitivity in simulating southeastern U.S. cold season severe weather environments. Weather and Forecasting, 30:591–612.

Conangla, L. and Cuxart, J. (2006). On the Turbulence in the Upper Part of the Low-Level Jet: An Experimental and Numerical study. Boundary-Layer Meteorology, 118:379–400.

Cushman-Roisin, B. and Beckers, J.-M. (2009). Introduction to Geophysical Fluid Dynamics: Physical and Numerical Aspects.

Cuxart, J. (2008). Nocturnal basin low-level jets: An integrated study. Acta Geophysica, 56:100–113.

Cuxart, J., Holtslag, A. A., Beare, R. J., Bazile, E., Beljaars, A., Cheng, A., Conangla, L., Ek, M., Freedman, F., Hamdi, R., Kerstein, A., Kitagawa, H., Lenderink, G., Lewellen, D., Mailhot, J., Mauritsen, T., Perov, V., Schayes, G., Steeneveld, G. J., Svensson, G., Taylor, P., Weng, W., Wunsch, S., and Xu, K. M. (2006). Single-column model intercomparison for a stably stratified atmospheric boundary layer. Boundary-Layer Meteorology, 118:273–303.

Cuxart, J. R., Jiménez, M. A., and Martínez, D. (2007). Nocturnal meso-beta basin and katabatic flows on a midlatitude island. Monthly Weather Review, 135:918–932.

De Wekker, S. F. J. and Whiteman, C. D. (2006). On the Time Scale of Nocturnal Boundary Layer Cooling in Valleys and Basins and over Plains. Journal of Applied Meteorology and Climatology, 45:813 – 820.

Dimitrova, R., Fernando, H., Silver, Z., Leo, L., Hocut, C., Zsedrovits, T., and Di Sabatino, S. (2014). Modification of the Yonsei University boundary layer scheme in the WRF model for stable conditions.

Domaradzki, J. A., Liu, W., and Brachet, M. E. (1993). An analysis of subgrid-scale interactions in numerically isotropic turbulence. Physics of Fluids.

Drobinski, P., Bastin, S., Dusek, J., Zängl, G., and Flamant, P. H. (2006). Flow splitting at the bifurcation between two valleys: Idealized simulations in comparison with Mesoscale Alpine Programme observations. Meteorology and Atmospheric Physics, 92:285–306.

Dubrulle, B. (2019). Beyond Kolmogorov cascades. Journal of Fluid Mechanics, 867.

Dudhia, J. (1989). Numerical study of convection observed during the Winter Monsoon Experiment using a mesoscale two-dimensional model. Journal of the Atmospheric Sciences, 46:3077–3107.

Ďurán, I. B., Geleyn, J. F., Vána, F., Schmidli, J., and Brožková, R. (2018). A turbulence scheme with two prognostic turbulence energies. Journal of the Atmospheric Sciences, 75:3381–3402.

Durden, D. J., Nappo, C. J., Leclerc, M. Y., Duarte, H. F., Zhang, G., Parker, M. J., and Kurzeja, R. J. (2013). On the impact of wave-like disturbances on turbulent fluxes and turbulence statistics in nighttime conditions: A case study. Biogeosciences, 10:8433–8443.

Einaudi, F. and Finnigan, J. J. (1993). Wave-Turbulence Dynamics in the Stably Stratified Boundary Layer. Journal of Atmospheric Sciences, 50:1841 – 1864.

Emory, M., Larsson, J., and Iaccarino, G. (2013). Modeling of structural uncertainties in Reynolds-averaged Navier-Stokes closures. Physics of Fluids, 25.

Eyink, G. L. and Sreenivasan, K. R. (2006). Onsager and the theory of hydrodynamic turbulence. Reviews of Modern Physics, 78:87–135.

Falocchi, M., Giovannini, L., de Franceschi, M., and Zardi, D. (2019). A method to determine the characteristic time-scales of quasi-isotropic surface-layer turbulence over complex terrain: A case-study in the Adige Valley (Italian Alps). Quarterly Journal of the Royal Meteorological Society, 145:495–512.

Falocchi, M., Tirler, W., Giovannini, L., Tomasi, E., Antonacci, G., and Zardi, D. (2020). A dataset of tracer concentrations and meteorological observations from the Bolzano tracer experiment (BTEX) to characterize pollutant dispersion processes in an alpine valley. Earth System Science Data, 12:277–291.

Fast, J. D., Zhong, S., and Whiteman, D. C. (1996). Boundary Layer Evolution within a Canyonland Basin. Part II: Numerical Simulations of Nocturnal Flows and Heat Budgets. Journal of Applied Meteorology, 35:2162–2178.

Finnigan, J. J., Einaudi, F., and Fua, D. (1984). The interaction between an Internal Gravity Wave and Turbulence in the Stably-Stratified Nocturnal Boundary Layer. Journal of Atmospheric Sciences, 41:2409 – 2436.

Foken, T. (2008). Micrometeorology. Springer, Berlin, Heidelberg.

Forrer, J. and Rotach, M. W. (1997). On the turbulence structure in the stable boundary layer over the Greenland ice sheet. Boundary-Layer Meteorology, 85:111–136.

Frisch, U. (1995). Turbulence: The Legacy of A.N. Kolmogorov.

Galperin, B., Kantha, L. H., Hassid, S., and Rosati, A. (1988). A Quasi-equilibrium Turbulent Energy Model for Geophysical Flows. Journal of Atmospheric Sciences, 45:55 – 62.

Galperin, B., Sukoriansky, S., and Anderson, P. S. (2007). On the critical Richardson number in stably stratified turbulence. Atmospheric Science Letters, 8:65–69.

Giometto, M. G., Katul, G. G., Fang, J., and Parlange, M. B. (2017). Direct numerical simulation of turbulent slope flows up to Grashof number $gr = 2.1 \times 10^{11}$. Journal of Fluid Mechanics, 829:589â620.

Giovannini, L., Antonacci, G., Zardi, D., Laiti, L., and Panziera, L. (2014). Sensitivity of simulated wind speed to spatial resolution over complex terrain. Energy Procedia, 59:323–329.

Giovannini, L., Ferrero, E., Karl, T., Rotach, M. W., Staquet, C., Castelli, S. T., and Zardi, D. (2020). Atmospheric Pollutant Dispersion over Complex Terrain: Challenges and Needs for Improving Air Quality Measurements and Modeling. Atmosphere, 11.

Giovannini, L., Laiti, L., Serafin, S., and Zardi, D. (2017). The thermally driven diurnal wind system of the Adige valley in the Italian Alps. Quarterly Journal of the Royal Meteorological Society, 143:2389–2402.

Giovannini, L., Zardi, D., and de Franceschi, M. (2011). Analysis of the urban thermal fingerprint of the city of Trento in the Alps. Journal of Applied Meteorology and Climatology, 50:1145–1162.

Godeferd, F. S. and Staquet, C. (2003). Statistical modelling and direct numerical simulations of decaying stably stratified turbulence. Part 2. Large-scale and small-scale anisotropy. Journal of Fluid Mechanics, 486:115–159.

Goger, B., Rotach, M. W., Gohm, A., Fuhrer, O., Stiperski, I., and Holtslag, A. A. (2018). The Impact of Three-Dimensional Effects on the Simulation of Turbulence Kinetic Energy in a Major Alpine Valley. Boundary-Layer Meteorology, 168:1–27.

Goger, B., Rotach, M. W., Gohm, A., Stiperski, I., Fuhrer, O., and Morsier, G. D. (2019). A new horizontal length scale for a three-dimensional turbulence parameterization in mesoscale atmospheric modeling over highly complex terrain. Journal of Applied Meteorology and Climatology, 58:2087–2102.

Grachev, A. A., Andreas, E. L., Fairall, C. W., Guest, P. S., and Persson, P. O. G. (2013). The Critical Richardson Number and Limits of Applicability of Local Similarity Theory in the Stable Boundary Layer. Boundary-Layer Meteorology, 147:51–82.

Grell, G. A., Dudhia, J., and Stauffer, D. (1994). A description of the fifth-generation Penn State/NCAR mesoscale model (MM5).

Haikin, N. and Castelli, S. T. (2022). On the Effect of a Low-level Jet on Atmospheric Pollutant Dispersion: A Case Study over a Coastal Complex Domain, Employing High-Resolution Modelling. Boundary-Layer Meteorology, 182:471–495.

Harikrishnan, A., Ansorge, C., Klein, R., and Vercauteren, N. (2021). Geometry and organization of coherent structures in stably stratified atmospheric boundary layers.

Hellström, R. Ã., FernÃ¡ndez, A., Mark, B. G., Covert, J. M., Rapre, A. C., and Gomez, R. J. (2017). Incorporating Autonomous Sensors and Climate Modeling to Gain Insight into Seasonal Hydrometeorological Processes within a Tropical Glacierized Valley. Annals of the American Association of Geographers, 107:260–273.

Higgins, C. W., Meneveau, C., and Parlange, M. B. (2007). The Effect of Filter Dimension on the Subgrid-Scale Stress, Heat Flux, and Tensor Alignments in the Atmospheric Surface Layer. Journal of Atmospheric and Oceanic Technology, 24:360 – 375.

Hong, S.-Y. and Lim, J.-O. J. (2006). The WRF Single-Moment 6-Class Microphysics Scheme (WSM6). Asia-pacific Journal of Atmospheric Sciences, 42:129–151.

Honnert, R. and Masson, V. (2014). What is the smallest physically acceptable scale for 1D turbulence schemes? Frontiers in Earth Science, 2.

Horst, T. W., Kleissl, J., Lenschow, D., Meneveau, C., Moeng, C.-H., Parlange, M., Sullivan, P., and Weil, J. (2004). HATS: Field Observations to Obtain Spatially Filtered Turbulence Fields from Crosswind Arrays of Sonic Anemometers in the Atmospheric Surface Layer. Journal of the Atmospheric Sciences, 61.

Howell, J. F. and Mahrt, L. (1977). MULTIRESOLUTION FLUX DECOMPOSITION. Boundary-Layer Meteorology, 83:117–137.

Huang, N. E., Shen, Z., Long, S. R., Wu, M. C., Shih, H. H., Zheng, Q., Yen, N.-C., Tung, C. C., and Liu, H. H. (1998). The empirical mode decomposition and the Hilbert spectrum for nonlinear and non-stationary time series analysis. Proceedings of the Royal Society of London. Series A: Mathematical, Physical and Engineering Sciences, 454(1971):903–995.

Janjic, Z. (2002). Nonsingular Implementation of the MellorâYamada Level 2.5 Scheme in the NCEP Meso Model. NCEP Office Note, 436.

Janjic, Z. I. (1994). The Step-Mountain Eta Coordinate Model: Further Developments of the Convection, Viscous Sublayer, and Turbulence Closure Schemes. Monthly Weather Review, 122:927–945.

Jeričević, A. and Grisogono, B. (2006). The critical bulk Richardson number in urban areas: verification and application in a numerical weather prediction model. Tellus A, pages 19–27.

Jiménez, M. A., Cuxart, J., and Martínez-Villagrasa, D. (2019). Influence of a valley exit jet on the nocturnal atmospheric boundary layer at the foothills of the Pyrenees. Quarterly Journal of the Royal Meteorological Society, 145:356–375.

Jofre, L., Domino, S. P., and Iaccarino, G. (2018). A framework for Characterizing Structural Uncertainty in Large-Eddy Simulation Closures. Flow, Turbulence and Combustion, 100:341–363.

Juliano, T. W., Kosović, B., Jiménez, P. A., Eghdami, M., Haupt, S. E., and Martilli, A. (2021). "gray Zone" Simulations using a Three-Dimensional Planetary Boundary Layer Parameterization in the Weather Research and Forecasting model. Monthly Weather Review.

Kang, Y., Belušić, D., and Smith-Miles, K. (2014). Detecting and classifying events in noisy time series. Journal of the Atmospheric Sciences, 71:1090–1104.

Kang, Y., Belušić, D., and Smith-Miles, K. (2015). Classes of structures in the stable atmospheric boundary layer. Quarterly Journal of the Royal Meteorological Society, 141:2057–2069.

Kassinos, S. C., Reynolds, W. C., and Rogers, M. M. (2001). One-point turbulence structure tensors. Journal of Fluid Mechanics, 428:213–248.

Katul, G. G., Parlange, M. B., Albertson, J. D., and Chu, C. R. (1995). Local isotropy and anisotropy in the sheared and heated atmospheric surface layer. Boundary-Layer Meteorology, 72:123–148.

Kit, E., Barami, E., and Fernando, H. J. S. (2021). Structure functions in nocturnal atmospheric boundary layer turbulence. Physical Review Fluids, 6.

Kleeorin, N., Rogachevskii, I., Soustova, I. A., Troitskaya, Y. I., Ermakova, O. S., and Zilitinkevich, S. (2019). Internal gravity waves in the energy and flux budget turbulence-closure theory for shear-free stably stratified flows. Physical Review E, 99.

Klipp, C. (2010). MULTIRESOLUTION REYNOLDS STRESS ANALYSIS OF URBAN CANYON TURBULENCE. In American Meteorological Society 16th Conference on Air Pollution Meteorology.

Kolmogorov, A. N. (1941a). Dissipation of Energy in Locally Isotropic Turbulence. Doklady Akademii Nauk SSSR, 32:16–18.

Kolmogorov, A. N. (1941b). The Local Structure of Turbulence in Incompressible Viscous Fluid for Very Large Reynolds Numbers. Doklady Akademii Nauk SSSR, 30:301–304.

Kolmogorov, A. N. (1941c). On the degeneration of isotropic turbulence in an incompressible viscous fluid. Doklady Akademii Nauk SSSR, 31:319–323.

Kolmogorov, A. N. (1962). A refinement of previous hypotheses concerning the local structure of turbulence in a viscous incompressible fluid at high Reynolds number. Journal of Fluid Mechanics, 13:82–85.

Kosović, B. (1997). Subgrid-scale modelling for the large-eddy simulation of high-Reynolds-number boundary layers. Journal of Fluid Mechanics, 336:151–182.

Kosović, B., Munoz, P. J., Juliano, T. W., Martilli, A., Eghdami, M., Barros, A. P., and Haupt, S. E. (2020). Three-Dimensional Planetary Boundary Layer Parameterization for High-Resolution Mesoscale Simulations. Journal of Physics: Conference Series, 1452.

Krogstad, P.-Å. and Torbergsen, L. E. (2000). Invariant Analysis of Turbulent Pipe Flow. Flow, Turbulence and Combustion, 64:161–181.

Kurbatskii, A. F. and Kurbatskaya, L. I. (2012). On the eddy mixing and energetics of turbulence in a stable atmospheric boundary layer. Izvestiya - Atmospheric and Ocean Physics, 48:595–602.

Kutsher, J., Haikin, N., Sharon, A., and Heifetz, E. (2012). On the Formation of an Elevated Nocturnal Inversion Layer in the Presence of a Low-Level Jet: A Case Study. Boundary-Layer Meteorology, 144:441–449.

Lampert, A., Pätzold, F., Jiménez, M. A., Lobitz, L., Martin, S., Lohmann, G., Canut, G., Legain, D., Bange, J., Martínez-Villagrasa, D., and Cuxart, J. (2016). A study of local turbulence and anisotropy during the afternoon and evening transition with an unmanned aerial system and mesoscale simulation. Atmospheric Chemistry and Physics, 16:8009–8021.

Lang, C. J. and Waite, M. L. (2019). Scale-dependent anisotropy in forced stratified turbulence. Physical Review Fluids, 4.

Lang, F., Belušić, D., and Siems, S. (2018). Observations of Wind-Direction Variability in the Nocturnal Boundary Layer. Boundary-Layer Meteorology, 166:51–68.

Lazeroms, W. M. J., Svensson, G., Bazile, E., Brethouwer, G., Wallin, S., and Johansson, A. V. (2016). Study of Transitions in the Atmospheric Boundary Layer Using Explicit Algebraic Turbulence Models. Boundary-Layer Meteorology, 161:19–47.

Lehner, M. and Rotach, M. W. (2018). Current Challenges in Understanding and Predicting Transport and Exchange in the Atmosphere over Mountainous Terrain. Atmosphere, 9(7).

Lin, Y.-L., Reeves, H. D., Chen, S.-Y., and Chiao, S. (2005). Formation Mechanisms for Convection over the Ligurian Sea during MAP IOP-8. Monthly Weather Review, 133:2227–2245.

Longo, S., Clavero, M., Chiapponi, L., and Losada, M. A. (2017). Invariants of turbulence Reynolds stress and of dissipation tensors in regular breaking waves. Water (Switzerland), 9.

Lovejoy, S. and Schertzer, D. (2013). The Weather and Climate: Emergent Laws and Multifractal Cascades. Cambridge Press Univeristy.

Lovejoy, S., Schertzer, D., Silas, P., Tessier, Y., and Lavallée, D. (1993). The unified scaling model of atmospheric dynamics and systematic analysis of scale invariance in cloud radiances. Geophysicae, 11:119–127.

Lumley, L. J. (1987). Computational Modeling of Turbulent Flows. Advances in applied mechanics, 18:123–176.

Mahrt, L. (2010). Variability and maintenance of turbulence in the very stable boundary layer. Boundary-Layer Meteorology, 135:1–18.

Mahrt, L. (2014). Stably stratified atmospheric boundary layers. Annual Review of Fluid Mechanics, 46:23–45.

Mahrt, L. and Acevedo, O. (2022). Types of Vertical Structure of the Nocturnal Boundary Layer. Boundary-Layer Meteorology.

Mahrt, L., Belušić, D., and Acevedo, O. (2021). Small-Scale Spatial Variation of the Nocturnal Wind Field. Boundary-Layer Meteorology, 180:225–245.

Mahrt, L., Pfister, L., and Thomas, C. K. (2020). Small-Scale Variability in the Nocturnal Boundary Layer. Boundary-Layer Meteorology, 174:81–98.

Mahrt, L., Sun, J., Blumen, W., Delany, T., and Oncley, S. (1998). Nocturnal boundary-layer regimes. Boundary-Layer Meteorology, 88:255–278.

Mahrt, L., Sun, J., and Stauffer, D. (2015). Dependence of Turbulent Velocities on Wind Speed and Stratification. Boundary-Layer Meteorology, 155:55–71.

Majda, A. J. and Shefter, M. G. (1998). Elementary stratified flows with instability at large Richardson number. Journal of Fluid Mechanics, 376:319–350.

Manneville, P. (2010). Instabilities, Chaos and Turbulence.

Markowski, P. and Richardson, Y. (2010). Mesoscale Meteorology in Midlatitudes.

Maroneze, R., Acevedo, O. C., Costa, F. D., Puhales, F. S., Demarco, G., and Mortarini, L. (2019a). The nocturnal boundary layer transition from weakly to very stable. Part II: Numerical simulation with a second-order model. Quarterly Journal of the Royal Meteorological Society, 145:3593–3608.

Maroneze, R., Acevedo, O. C., Costa, F. D., and Sun, J. (2019b). Simulating the Regime Transition of the Stable Boundary Layer Using Different Simplified Models. Boundary-Layer Meteorology, 170:305–321.

Massey, J. D., Steenburgh, W. J., Knievel, J. C., and Cheng, W. Y. (2016). Regional soil moisture biases and their influence on WRF model temperature forecasts over the intermountain west. Weather and Forecasting, 31:197–216.

Mellor, G. L. (1982). Development of a Turbulence Closure Model for Geophysical Fluid Problems. Reviews of Geophysics and Space Physics, 20:851–875.

Meybeck, M., Green, P., and Vörösmarty, C. (2001). A New Typology for Mountains and Other Relief Classes: An Application to Global Continental Water Resources and Population Distribution. Mountain Research and Development, 21:34–45.

Mishra, A. A., Mukhopadhaya, J., Alonso, J., and Iaccarino, G. (2020). Design exploration and optimization under uncertainty. Physics of Fluids, 32.

Mlawer, E. J., Taubman, S. J., Brown, P. D., Iacono, M. J., and Clough, S. A. (1997). Radiative transfer for inhomogeneous atmospheres: RRTM, a validated correlated-k model for the longwave. Journal of Geophysical Research Atmospheres, 102:16663–16682.

Monti, P., Fernando, H. J. S., Princevac, M., Chan, W. C., Kowalewski, T. A., and Pardyjak, E. R. (2002). Observations of Flow and Turbulence in the Nocturnal Boundary Layer over a Slope. Journal of the Atmospheric Sciences, 59.

Mortarini, L., Cava, D., Giostra, U., Acevedo, O., Martins, L. G. N., de Oliveira, P. E. S., and Anfossi, D. (2018). Observations of submeso motions and intermittent turbulent mixing across a low level jet with a 132-m tower. Quarterly Journal of the Royal Meteorological Society, 144:172–183.

Muñoz, R. C., Armi, L., Rutllant, J. A., Falvey, M., Whiteman, C. D., Garreaud, R., Arriagada, A., Flores, F., and Donoso, N. (2020). Raco Wind at the Exit of the Maipo Canyon in Central Chile: Climatology, Special Observations, and Possible Mechanisms. Journal of Applied Meteorology and Climatology, 59:725–749.

Nappo, J. C. (2002). An introduction to atmospheric gravity waves, volume 85. International geophysics series.

Navarra, A. (2019). Global dynamics (Lectures).

Neff, W. D. (1988). Observations of complex terrain flows using acoustic sounders: Echo interpretation. Boundary-Layer Meteorology, 42:207–228.

Neff, W. D. and King, C. W. (1987). Observations of complex-terrain flows using acoustic sounders: Experiments, topography, and winds. Boundary-Layer Meteorology, 40:363–392.

Neff, W. D. and King, C. W. (1989). The Accumulation and Pooling of Drainage Flows in a Large Basin. Journal of Applied Meteorology, 28:518–529.

Neiman, P. J., Gottas, D. J., and White, A. B. (2019). A two-cool-season wind profiler-based analysis of westward-directed gap flow through the Columbia river gorge. Monthly Weather Review, 147:4653–4680.

Nieuwstandt, F. T. M. (1985). A model for the stationary, stable boundary layer. In Hunt, J. C. R., editor, Turbulence and diffusion in stable environments, pages 149–179. Oxford University Press.

Nikolic, J., Zhong, S., Pei, L., Bian, X., Heilman, W. E., and Charney, J. J. (2019). Sensitivity of Low-Level Jets to Land-Use and Land-Cover Change over the Continental U.S. Atmosphere, 10:174.

Niu, G. Y., Yang, Z. L., Mitchell, K. E., Chen, F., Ek, M. B., Barlage, M., Kumar, A., Manning, K., Niyogi, D., Rosero, E., Tewari, M., and Xia, Y. (2011). The community noah land surface model with multiparameterization options (noah-MP): 1. model description and evaluation with local-scale measurements. Journal of Geophysical Research Atmospheres, 116.

Oboukhov, A. M. (1962). Some specific features of atmospheric turbulence. Journal of Fluid Mechanics, 13.

Oettl, D., Goulart, A., Degrazia, G., and Anfossi, D. (2005). A new hypothesis on meandering atmospheric flows in low wind speed conditions. Atmospheric Environment, 39:1739–1748.

Ohya, Y. and Uchida, T. (2003). Turbulence structure of stable boundary layers with a near-linear temperature profile. Boundary-Layer Meteorology, 108:19–38.

Onsager, L. (1949). Statistical hydrodynamics. pages 279–287. Il Nuovo Cimento.

Ookouchi, Y., Segal, M., Kessler, R. C., and Pielke, R. A. (1984). Evaluation of Soil Moisture Effects on the Generation and Modification of Mesoscale Circulations. Monthly Weather Review, 112:2281 – 2292.

O'Steen, L. B. (2000). Numerical Simulation of Nocturnal Drainage Flows in Idealized Valley-Tributary Systems. Journal of Applied Meteorology, 39:1845–1860.

Pamperin, H. and Stilke, G. (1985). Nächtliche grenzschicht und llj im alpenvorland nahe dem inntalausgang (Nocturnal boundary layer and low-level jet near the Inn Valley exit). Meteorologische Rundschau, 38:145–156.

Pappaccogli, G., Giovannini, L., Cappelletti, F., and Zardi, D. (2018). Challenges in the application of a WRF/Urban-TRNSYS model chain for estimating the cooling demand of buildings: A case study in Bolzano (Italy). Science and Technology for the Built Environment, 24:529–544.

Pedlosky, J. (1987). Geophysical Fluid Dynamics. Springer New York, 2 edition.

Petenko, I., Casasanta, G., Bucci, S., Kallistratova, M., Sozzi, R., and Argentini, S. (2020). Turbulence, low-level jets, and waves in the tyrrhenian coastal zone as shown by sodar. Atmosphere, 11.

Pfister, L., Lapo, K., Mahrt, L., and Thomas, C. K. (2021). Thermal Submesoscale Motions in the Nocturnal Stable Boundary Layer. Part 1: Detection and Mean Statistics. Boundary-Layer Meteorology, 180:187–202.

Piccirillo, P. and Atta, C. W. V. (1997). The evolution of a uniformly sheared thermally stratified turbulent flow. Journal of Fluid Mechanics, 334:61–86.

Pinto, J. O., Parsons, D. B., Brown, W. O. J., Cohn, S., Chamberlain, N., and Morley, B. (2006). Coevolution of Down-Valley Flow and the Nocturnal Boundary Layer in Complex Terrain. Journal of Applied Meteorology and Climatology, 45:1429–1449.

Pope, S. B. (2000). Turbulent Flows. Cambridge University Press.

Porté-Agel, F., Parlange, M. B., Meneveau, C., and Eichinger, W. E. (2001). A Priori Field Study of the Subgrid-Scale Heat Fluxes and Dissipation in the Atmospheric Surface Layer. Journal of the Atmospheric Sciences, 58.

Prandtl, L. (1942). Führer durch die Strömungslehre. Vieweg und Sohn: Braunschweig, Germany.

Princevac, M., Hunt, J. C. R., and Fernando, H. J. S. (2008). Quasi-Steady Katabatic Winds on Slopes in Wide Valleys: Hydraulic Theory and Observations. Journal of the Atmospheric Sciences, 65(2):627 – 643.

Quimbayo-Duarte, J., Staquet, C., Chemel, C., and Arduini, G. (2019). Dispersion of Tracers in the Stable Atmosphere of a Valley Opening onto a Plain. Boundary-Layer Meteorology, 172:291–315.

Rees, J. M., Denholm-Price, J. C. W., King, J. C., and Anderson, P. S. (2000). A Climatological Study of Internal Gravity Waves in the Atmospheric Boundary Layer Overlying the Brunt Ice Shelf, Antarctica. Journal of the Atmospheric Sciences.

Rees, J. M., Staszewski, W. J., and Winkler, J. R. (2001). Case study of a wave event in the stable atmospheric boundary layer overlying an Antarctic Ice Shelf using the orthogonal wavelet transform. Dynamics of Atmospheres and Oceans, 34:245–261.

Reeves, D. H. and Lin, Y.-L. (2006). Effect of Stable Layer Formation over the Po Valley on the Development of Convection during MAP IOP-8. Journal of the atmospheric sciences, 63:2567–2584.

Renfrew, I. A. (2004). The dynamics of idealized katabatic flow over a moderate slope and ice shelf. Quarterly Journal of the Royal Meteorological Society, 130:1023–1045.

Reynolds, O. (1895). On the dynamical theory of incompressible viscous fluids and the determination of the criterion. Philosophical Transactions of the Royal Society of London. A, 186:123–164.

Richardson, H., Basu, S., and Holtslag, A. A. (2013). Improving Stable Boundary-Layer Height Estimation Using a Stability-Dependent Critical Bulk Richardson Number. Boundary-Layer Meteorology, 148:93–109.

Rotach, M. W., Gohm, A., Lang, M. N., Leukauf, D., Stiperski, I., and Wagner, J. S. (2015). On the vertical exchange of heat, mass, and momentum over complex, mountainous terrain. Frontiers in Earth Sciences, 3:1–14.

Rucker, M., Banta, R. M., and Steyn, D. G. (2008). Along-valley structure of daytime thermally driven flows in the flows in the Wipp valley. Journal of Applied Meteorology and Climatology, 47:733–751.

Sabatier, T., Paci, A., Lac, C., Canut, G., Largeron, Y., and Masson, V. (2020). Semi-idealized simulations of wintertime flows and pollutant transport in an Alpine valley: Origins of local circulations (Part I). Quarterly Journal of the Royal Meteorological Society, 146:807–826.

Sagaut, P. and Cambon, C. (2018). Homogeneous Turbulence Dynamics. Springer International Publishing AG.

Sasaki, K., Sawada, M., Ishii, S., Kanno, H., Mizutani, K., Aoki, T., Itabe, T., Matsushima, D., Sha, W., Noda, A. T., Ujiie, M., Matsuura, Y., and Iwasaki, T. (2010). The temporal evolution and spatial structure of the local easterly wind 'Kiyokawa-dashi' in Japan Part II: Numerical simulations. Journal of the Meteorological Society of Japan, 88:161–181.

Schertzer, D. and Lovejoy, S. (1985). The Dimension and Intermittency of Atmospheric Dynamics.

Schmidli, J., Poulos, G. S., Daniels, M. H., and Chow, F. K. (2009). External influences on nocturnal thermally driven flows in a deep valley. Journal of Applied Meteorology and Climatology, 48:3–23.

Schmitt, F. G. (2007). About Boussinesq's turbulent viscosity hypothesis: historical remarks and a direct evaluation of its validity. Comptes Rendus - Mecanique, 335:617–627.

Schmitt, F. G., Huang, Y., Zhiming, L., Liu, Y., and Fernandez, N. (2009). Analysis of velocity fluctuations and their intermittency properties in the surf zone using empirical mode decomposition. Journal of Marine Systems, 77:473–481.

Serafin, S., Adler, B., Cuxart, J., Wekker, S. F. D., Gohm, A., Grisogono, B., Kalthoff, N., Kirshbaum, D. J., Rotach, M. W., Schmidli, J., Stiperski, I., Željko Večenaj, and Zardi, D. (2018). Exchange processes in the atmospheric boundary layer over mountainous terrain.

Shih, T.-H., Liou, W. W., Shabbir, A., Yang, Z., and Zhu, J. (1995). A new k-ϵ eddy viscosity model for high Reynolds number turbulent flows. Computers & Fluids, 24(3):227–238.

Shin, H. H. and Hong, S. Y. (2011). Intercomparison of Planetary Boundary-Layer Parametrizations in the WRF model for a Single Day from CASES-99. Boundary-Layer Meteorology, 139:261–281.

Singh, S. K., Raushan, P. K., Kumar, P., and Debnath, K. (2021). Anisotropy of Reynolds stress tensor in combined wave-current flow. Journal of Offshore Mechanics and Arctic Engineering, 143.

Skamarock, C. W., Klemp, B. J., Dudhia, J., Gill, O. D., Barker, D., Duda, G. M., yu Huang, X., Wang, W., and Powers, G. J. (2008). A Description of the Advanced Research WRF version 3 (no. ncar/tn-475+str.

Smyth, W. D. and Moum, J. N. (2000). Anisotropy of turbulence in stably stratified mixing layers. Physics of Fluids, 12:1343–1362.

Spengler, T., Schween, J. H., Ablinger, M., Zängl, G., and Egger, J. (2009). Thermally driven flows at an asymmetric valley exit: Observations and model studies at the Lech Valley exit. Monthly Weather Review, 137:3437–3455.

Sroka, S. and Guimond, S. R. (2021). Organized kinetic energy backscatter in the hurricane boundary layer from radar measurements. Journal of Fluid Mechanics, 924.

Staquet, C. and Sommeria, J. (2002). Internal gravity waves: From instabilities to turbulence. Annual Review of Fluid Mechanics, 34:559–593.

Stensrud, D. J. (1996). Importance of Low-Level Jets to Climate: A Review. Journal of Climate, 9:1698 – 1711.

Stewart, R. W. (1969). Turbulence and waves in a stratified atmosphere. Radio Science, 4:1269–1278.

Steyn, D. G., De Wekker, S. F. J., Kossmann, M., and Martilli, A. (2013). Boundary layers and air quality in mountainous terrain. In Chow, F. K., De Wekker, S. F., and Snyder, B. J., editors, Mountain Weather Research and Forecasting: Recent Progress and Current Challenges, pages 261–289. Springer The Netherlands, Dordrecht.

Stiperski, I. and Calaf, M. (2018). Dependence of near-surface similarity scaling on the anisotropy of atmospheric turbulence. Quarterly Journal of the Royal Meteorological Society, 144:641–657.

Stiperski, I. and Calaf, M. (2022). Generalizing Monin-Obukhov similarity theory (1954) for complex atmospheric turbulence.

Stiperski, I., Calaf, M., and Rotach, M. W. (2019). Scaling, Anisotropy, and Complexity in Near-Surface Atmospheric Turbulence. Journal of Geophysical Research: Atmospheres, 124:1428–1448.

Stiperski, I., Chamecki, M., and Calaf, M. (2021). Anisotropy of Unstably Stratified Near-Surface Turbulence. Boundary-Layer Meteorology.

Stull, R. B. (1988). An introduction to boundary layer meteorology. Kluwer Academic Publishers.

Sukoriansky, S. and Galperin, B. (2012). An analytical theory of the buoyancy-Kolmogorov subrange transition in turbulent flows with stable stratification. Phil. Trans. R. Soc. A., 371.

Sun, J., Lenschow, D. H., Burns, S. P., Banta, R. M., Newsom, R. K., Coulter, R., Frasier, S., Ince, T., Nappo, C., Balsley, B. B., Jensen, M., Mahrt, L., Miller, D., and Skelly, B. (2004). Atmospheric disturbances that generate intermittent turbulence in nocturnal boundary layers. Boundary-Layer Meteorology, 110:255–279.

Sun, J., Lenschow, D. H., LeMone, M. A., and Mahrt, L. (2016). The Role of Large-Coherent-Eddy Transport in the Atmospheric Surface Layer Based on CASES-99 Observations. Boundary-Layer Meteorology, 160:83–111.

Sun, J., Mahrt, L., Banta, R. M., and Pichugina, Y. L. (2012). Turbulence regimes and turbulence intermittency in the stable boundary layer: During CASES-99. Journal of the Atmospheric Sciences, 69:338–351.

Sun, J., Mahrt, L., Nappo, C., and Lenschow, D. H. (2015a). Wind and temperature oscillations generated by wave-turbulence interactions in the stably stratified boundary layer. Journal of the Atmospheric Sciences, 72:1484–1503.

Sun, J., Nappo, C. J., Mahrt, L., Belušic, D., Grisogono, B., Stauffer, D. R., Pulido, M., Staquet, C., Jiang, Q., Pouquet, A., Yagüe, C., Galperin, B., Smith, R. B., Finnigan, J. J., Mayor, S. D., Svensson, G., Grachev, A. A., and Neff, W. D. (2015b). Review of wave-turbulence interactions in the stable atmospheric boundary layer. Reviews of Geophysics, 53:956–993.

Svensson, N., Arnqvist, J., Bergström, H., Rutgersson, A., and Sahlée, E. (2019). Measurements and Modelling of Offshore Wind Profiles in a Semi-Enclosed Sea. Atmosphere, 10.

Taylor, G. I. (1938). Production and dissipation of vorticity in a turbulent fluid. Proceedings of the Royal Society A, 164:15–23.

Therry, G. and Lacarrére, P. (1983). Improving the Eddy Kinetic Energy model for planetary boundary layer description. Boundary-Layer Meteorology, 25:63–88.

Tomasi, E., Giovannini, L., Falocchi, M., Antonacci, G., Jiménez, P. A., Kosović, B., Alessandrini, S., Zardi, D., Monache, L. D., and Ferrero, E. (2019). Turbulence parameterizations for dispersion in sub–kilometer horizontally non-homogeneous flows. Atmospheric Research, 228:122–136.

Tomasi, E., Giovannini, L., Zardi, D., and de Franceschi, M. (2017). Optimization of Noah and Noah_MP WRF land surface schemes in snow–melting conditions over complex terrain. Monthly Weather Review, 145:4727–4745.

Trini, S. C., Ferrero, E., and Anfossi, D. (2001). Turbulence closures in neutral boundary layers over complex terrain. Boundary-Layer Meteorology.

Tuononen, M., OâConnor, E. J., Sinclair, V. A., and Vakkari, V. (2017). Low-Level Jets over Utö, Finland, Based on Doppler Lidar Observations. Journal of Applied Meteorology and Climatology, 56:2577 – 2594.

Vallis, G. K. (2005). Atmospheric and Oceanic Fluid Dynamics. Cambridge University Press.

Vassilicos, J. C. (2015). Dissipation in turbulent flows. Annual Review of Fluid Mechanics, 47:95–114.

Vercauteren, N., Boyko, V., Faranda, D., and Stiperski, I. (2019a). Scale interactions and anisotropy in stable boundary layers. Quarterly Journal of the Royal Meteorological Society, 145:1799–1813.

Vercauteren, N., Boyko, V., Kaiser, A., and Belušić, D. (2019b). Statistical investigations of flow structures in different regimes of the stable boundary layer. Boundary-Layer Meteorology, 173:143–164.

Vercauteren, N. and Klein, R. (2015). A clustering method to characterize intermittent bursts of turbulence and interaction with submesomotions in the stable boundary layer. Journal of the Atmospheric Sciences, 72:1504–1517.

Vercauteren, N., Mahrt, L., and Klein, R. (2016). Investigation of interactions between scales of motion in the stable boundary layer. Quarterly Journal of the Royal Meteorological Society, 142:2424–2433.

Večenaj, Z. and De Wekker, S. F. (2015). Determination of non-stationarity in the surface layer during the T-REX experiment. Quarterly Journal of the Royal Meteorological Society, 141:1560–1571.

Viana, S., Terradellas, E., and Yagüe, C. (2010). Analysis of Gravity Waves Generated at the Top of a Drainage Flow. Journal of the Atmospheric Sciences, 67(12):3949–3966.

Vickers, D. and Mahrt, L. (2003). The Cospectral Gap and Turbulent Flux Calculations. Journal of Atmospheric and Oceanic Technology.

Vickers, D. and Mahrt, L. (2006). A SOLUTION FOR FLUX CONTAMINATION BY MESOSCALE MOTIONS WITH VERY WEAK TURBULENCE. Boundary-Layer Meteorology, 118:431–447.

Vignon, E., Picard, G., Duran-Alarcon, C., Alexander, S. P., Gallee, H., and Berne, A. (2020). Gravity wave excitation during the coastal transition of an extreme katabatic flow in Antarctica. Journal of the Atmospheric Sciences, 77:1295–1312.

Vignon, E., van de Wiel, B. J., van Hooijdonk, I. G., Genthon, C., van der Linden, S. J., van Hooft, J. A., Baas, P., Maurel, W., Traullé, O., and Casasanta, G. (2017). Stable boundary-layer regimes at Dome C, Antarctica: observation and analysis. Quarterly Journal of the Royal Meteorological Society, 143:1241–1253.

Voronovich, V. and Kiely, G. (2007). On the gap in the spectra of surface-layer atmospheric turbulence. Boundary-Layer Meteorology, 122:67–83.

Watanabe, T. and Nagata, K. (2021). Large-scale characteristics of a stably stratified turbulent shear layer. Journal of Fluid Mechanics, 927.

Watanabe, T., Riley, J. J., Nagata, K., Matsuda, K., and Onishi, R. (2019). Hairpin vortices and highly elongated flow structures in a stably stratified shear layer. Journal of Fluid Mechanics, 878:37–61.

Wei, W., Schmitt, F., Huang, Y., and Zhang, H. (2016). The Analyses of Turbulence Characteristics in the Atmospheric Surface Layer Using Arbitrary-Order Hilbert Spectra. Boundary-Layer Meteorology, 159:391–406.

Wei, Z., Zhang, H., Wei, W., Zhang, X., Cai, X., Song, Y., and Zhu, T. (2022). Mechanism of the effect of vertically propagating internal gravity waves on turbulence barrier and pollutant diffusion during heavy haze episodes. Science of The Total Environment, 845:157349.

Weigel, A. P. and Rotach, M. W. (2004). Flow structure and turbulence characteristics of the daytime atmosphere in a steep and narrow Alpine valley. Quarterly Journal of the Royal Meteorological Society, 130:2605–2627.

Whiteman, C. D. (1990). Observations of thermally developed wind systems in mountainous terrain. In *Atmospheric Processes over Complex Terrain.* pages 5–42.

Whiteman, C. D. (2000). Mountain Meteorology. Oxford University Press.

Whiteman, C. D. and Doran, J. C. (1993). The relationship between overlying synoptic–scale flows and winds within a valley. 32.

Whiteman, C. D., Zhong, S., Shaw, W. J., Hubbe, J. M., Bian, X., and Mittelstadt, J. (2001). Cold Pools in the Columbia Basin. Weather and Forecasting, 16:432–447.

Wingstedt, E. M., Fossum, H. E., Reif, B. A., and Werne, J. (2015). Anisotropy and shear-layer edge dynamics of statistically unsteady, stratified turbulence. Physics of Fluids, 27.

Winstead, N. S. and Young, G. S. (2000). An analysis of exit-flow drainage jets over the Chesapeake Bay. Journal of Applied Meteorology, 39:1269–1281.

Wyngaard, J. C. (2004). Toward Numerical Modeling in the ”Terra Incognita”. Journal of the Atmopsheric Sciences, 61:1816–1826.

Yu, Y. and Cai, X. M. (2006). Structure and dynamics of katabatic flow jumps: Idealised simulations. Boundary-Layer Meteorology, 118:527–555.

Zaitseva, D. V., Kallistratova, M. A., Lyulyukin, V. S., Kouznetsov, R. D., and Kuznetsov, D. D. (2018). The effect of Internal Gravity Waves on Fluctuations in Meteorological Parameters of the Atmospheric Boundary Layer. Izvestiya, Atmospheric and Oceanic Physics, 54:173–181.

Zängl, G. (2004). A reexamination of the valley wind system in the Alpine Inn Valley with numerical simulations. Meteorology and Atmospheric Physics, 87:241–256.

Zardi, D., Falocchi, M., Giovannini, L., Tirler, W., Tomasi, E., Antonacci, G., Ferrero, E., Alessandrini, S., Jimenez, P. A., Kosović, B., and Monache, L. D. (2021). The Bolzano Tracer Experiment (BTEX). Bulletin of the American Meteorological Society, 102(5):E966 – E989.

Zardi, D. and Whiteman, C. (2013). Diurnal Mountain Wind Systems. Mountain Weather Research and Forecasting, pages 35–119.

Zeri, M. and Sá, L. D. (2011). Horizontal and Vertical Turbulent Fluxes Forced by a Gravity Wave Event in the Nocturnal Atmospheric Surface Layer Over the Amazon Forest. Boundary-Layer Meteorology, 138:413–431.

Zilitinkevich, S. and Baklanov, A. (2002). Calculation of the height of the stable boundary layer in practical applications. Boundary-Layer Meteorology.

Zilitinkevich, S., Druzhinin, O., Glazunov, A., Kadantsev, E., Mortikov, E., Repina, I., and Troitskaya, Y. (2019). Dissipation rate of turbulent kinetic energy in stably stratified sheared flows. Atmospheric Chemistry and Physics, 19:2489–2496.

Zilitinkevich, S. S., Elperin, T., Kleeorin, N., L'Vov, V., and Rogachevskii, I. (2009). Energy- and flux-budget turbulence closure model for stably stratified flows. Part II: The role of internal gravity waves. Boundary-Layer Meteorology, 133:139–164.

Zilitinkevich, S. S., Elperin, T., Kleeorin, N., and Rogachevskii, I. (2007). Energy–and flux–budget (EFB) turbulence closure model for stably stratified flows. Part I: steady–state, homogeneous regimes. Boundary-Layer Meteorology, 125:167–191.

Zilitinkevich, S. S., Elperin, T., Kleeorin, N., Rogachevskii, I., Esau, I., Mauritsen, T., and Miles, M. V. (2008). Turbulence energetics in stably stratified geophysical flows: Strong and weak mixing regimes. Quarterly Journal of the Royal Meteorological Society, 134:793–799.

Zonato, A., Martilli, A., Jimenez, P. A., Dudhia, J., Zardi, D., and Giovannini, L. (2022). A new K–ϵ turbulence parameterization for mesoscale meteorological models. Monthly Weather Review.

Appendix A

Multiresolution decomposition (MRD) analysis

In Chapter 2, it has been noted that the choice of the correct timescale to define turbulent fluctuations for Reynolds decomposition is not always straightforward. A method commonly used at this purpose is the multiresolution decomposition (MRD), also applied in Section 2.4.5, which yields information on the scale dependence of variances and covariances (Vickers and Mahrt, 2003). The scale dependence of the flux often shows a cospectral gap region that separates the turbulent scales of the cospectrum from the mesoscale transport, thus providing a method for choosing the turbulent timescale. The choice of the perturbation timescale sets an upper-limit on the range of scales included in the computed variances and covariances. While in unstable conditions the turbulent flux is large and accidentally including non-turbulent motion in Reynolds averaging is thought to have a small impact on the flux, the same is not true for stable conditions, where turbulence is weaker. As mentioned several times throughout the thesis, stably stratified flows are also characterised by many non-turbulent motions and including their contribution in turbulent flux can strongly affect the magnitude, and even change the sign of the flux. Thus, the MRD technique is widely used in SBL studies (Vickers and Mahrt, 2006; Voronovich and Kiely, 2007; Vercauteren et al., 2016, 2019a).

A.1 Method

The MRD technique uses a wavelet approach, based on the Haar transform, and partitions the data record into simple block averages on different scales. For efficient calculations, the MRD analysis requires a power of two number of data points, thus studying dyadic scales. There are several algorithms to perform multi-resolution decomposition, and two of them are reported here.

A.1.1 MRD from fluctuations time series

Let's consider a time series $u(t)$, and let's study the scale dependence of the variance in a record of 2^M data points. In order to obtain the M components of the multiresolution decomposition, each one corresponding to a different range of scales, the procedure to follow is:

1. Compute the average $\overline{u}_M$ over the record and compute the corresponding fluctuations time series $u'_M(t)$;
2. Separate $u'_M(t)$ in 2 records, (1) and (2), of 2^{M-1} data points, with (1) corresponding to the first half of data points in the record of 2^M points, and (2) to the second half;
3. Compute the average $\overline{u'}$ for each record, $\overline{u'}_{(1)}$ and $\overline{u'}_{(2)}$, and the corresponding fluctuations time series $u''_{(1)}(t)$ and $u''_{(2)}(t)$, with $u''_{M-1}(t) = \left[u''_{(1)}(t), u''_{(2)}(t)\right]$;
4. Separate $u''_{M-1}(t)$ in 2^2 records, (1_1),(1_2),(2_1) and (2_2), of 2^{M-2} data points, with (1_1) corresponding to the first half of data points in the record (1),(1_2) to the second half of data points in the record (1),(2_1) to the first half of data points in the record (2) and (2_2) to the second half of data points in the record (2);
5. Compute the average $\overline{u''}$ for each record, $\overline{u''}_{(1_1)}$, $\overline{u''}_{(1_2)}$, $\overline{u''}_{(2_1)}$ and $\overline{u''}_{(2_2)}$, and the corresponding fluctuations time series $u'''_{(1_1)}(t)$,$u'''_{(1_2)}(t)$,$u'''_{(2_1)}(t)$ and $u'''_{(2_2)}(t)$, with $u'''_{M-2}(t) = \left[u'''_{(1_1)}(t), u'''_{(1_2)}(t), u'''_{(2_1)}(t), u'''_{(2_2)}(t)\right]$;
6. and so on, until the 2^M records with only 1 point.

The labelling used for windows is shown in Figure A.1, and the MRD components are estimated from the averages $\overline{u'}_{(.)}, \overline{u''}_{(.)}$, etc. The first MRD component is:

$$D_{uu}(M) = \frac{\overline{u'}^2_{(1)} + \overline{u'}^2_{(2)}}{2}$$

The second MRD component is

$$D_{uu}(M-1) = \frac{\overline{u''}^2_{(1_1)} + \overline{u''}^2_{(1_2)} + \overline{u''}^2_{(2_1)} + \overline{u''}^2_{(2_2)}}{2^2}$$

and so on.
The MR spectra is made up of the MRD components, which can be interpreted as the second moments about the mean of the M series made of $\{\overline{u'}_{(.)}\}$, $\{\overline{u''}_{(.)}\}$, $\{\overline{u'''}_{(.)}\}$, etc, as the mean of each of these time series is zero by definition
$\left(u_M = \overline{u}_M + u'_M \text{ and } \overline{u'}_M = 0, u'_{(1)} = \overline{u'}_{(1)} + u''_{(1)} \text{ and } \overline{u''}_{(1)} = 0, \text{ etc.}\right)$.
For example $\frac{\overline{u'}_{(1)}+\overline{u'}_{(2)}}{2} = 0$ or $\frac{\overline{u''}_{(1_1)}+\overline{u''}_{(1_2)}+\overline{u''}_{(2_1)}+\overline{u''}_{(2_2)}}{4} = 0$.
MR cospectra can also be defined, applying the previous procedure to each time series

separately and then computing the MRD components using the product of the means obtained from the different time series. For example, the first MRD component of the MR cospectra of u(t) and v(t) will be:

$$D_{uv}(M) = \frac{\overline{u'}_{(1)}\overline{v'}_{(1)} + \overline{u'}_{(2)}\overline{v'}_{(2)}}{2}$$

Unlike Fourier decomposition, the method does not assume periodicity and the scale dependence of MRD depends on the scale of the fluctuations and not on the periodicity. If the record analysed is made of 2^M data points, with a sampling frequency of 20 Hz ($\delta t = 0.05\,\mathrm{s}$), the timescales in the MR (co)spectrum span in the range $\tau = [2\delta t, 2^M \delta t]$. If the record analysed is $\sim$ 1 hour long ($M = 16$), then $[0.1\,\mathrm{s}, \sim 55\,\mathrm{min}]$, and the $D(n)$ component of the MR (co)spectrum is the contribution to the total (co)variance of structures with scales ranging in $[2^{(n-1)}\delta t, 2^n \delta t]$.

A.1.2 MRD from averages

If few rules of averaging are taken into account ($\overline{\overline{a}} = \overline{a}$ and $\overline{a+b} = \overline{a} + \overline{b}$), the previous procedure to obtain MRD components can be simplified. In fact, it is possible to compute the MRD components only considering the original record of 2^M data points and averages at different scales, $\overline{u}_{(.)}$, thus avoiding to compute the fluctuations time series at each scale. Averaging the original record using different averaging lengths is equivalent to view the data at different resolutions, with the average acting as a low-pass filter.
The first MRD component can be rewritten as:

$$D_{uu}(M) = \frac{\overline{u'}^2_{(1)} + \overline{u'}^2_{(2)}}{2} = \frac{\overline{u_{(1)} - \overline{u}_M}^2 + \overline{u_{(2)} - \overline{u}_M}^2}{2} = \frac{(\overline{u}_{(1)} - \overline{u}_M)^2 + (\overline{u}_{(2)} - \overline{u}_M)^2}{2}$$

Since $\overline{u}_{(1)} + \overline{u}_{(2)} = 2\overline{u}_M$, then:

$$D_{uu}(M) = \frac{(2\overline{u}_M - \overline{u}_{(2)} - \overline{u}_M)^2 + (\overline{u}_{(2)} - \overline{u}_M)^2}{2} = (\overline{u}_{(2)} - \overline{u}_M)^2$$

With a similar reasoning $\Big(\overline{u}_{(1_1)} + \overline{u}_{(1_2)} = 2\overline{u}_{(1)}, \quad \overline{u}_{(1_{1_1})} + \overline{u}_{(1_{1_2})} = 2\overline{u}_{(1_1)}, \text{ etc.}\Big)$:

$$D_{uu}(M-1) = \frac{(\overline{u}_{(1_1)} - \overline{u}_{(1)})^2 + (\overline{u}_{(2_1)} - \overline{u}_{(2)})^2}{2}$$

$$D_{uu}(M-2) = \frac{(\overline{u}_{(1_{1_1})} - \overline{u}_{(1_1)})^2 + (\overline{u}_{(1_{2_1})} - \overline{u}_{(1_2)})^2 + (\overline{u}_{(2_{1_1})} - \overline{u}_{(2_1)})^2 + (\overline{u}_{(2_{2_1})} - \overline{u}_{(2_2)})^2}{4}$$

and so on, where averaging windows are labelled with the same convention of previous section (Figure A.1). The last step, to estimate $D_{uu}(1)$, is based on differences of 1 point averages (that is the individual data points in the original record) and 2 point averages. Differences between data at two different resolutions (averaging lengths) generate the multiresolution decomposition, thus making the interpretation of MR spectra simpler.

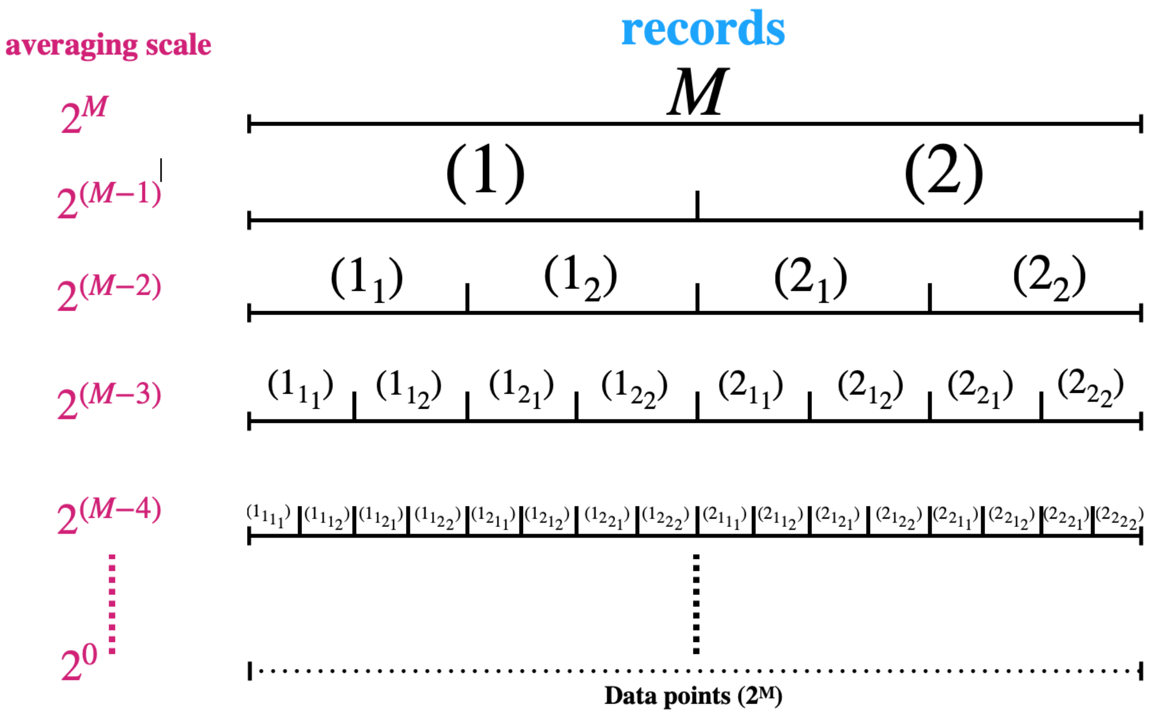

Figure A.1: Multiresolution averaging windows with label convention used in the text.

Each component is the variance associated with scales between the short and long averaging length considered. Table A.1 shows an example of multiresolution decomposition, using both formulations, for a record of 2^4 data points.

A.2 Relation between Reynolds averaging and MRD components

As summarized in Howell and Mahrt (1977), MRD analysis has some advantages with respect to Fourier analysis for studying scale dependence of turbulent fluxes. In particular, an explicit relationship between components of the Fourier spectra and Reynolds averaging does not exist, while this limitation is overcome in MR spectra. Each component in MR spectra can be interpreted in terms of unweighted (nonoverlapping) moving averages (as evident from Section A.1.2), thus satisfying the rules of Reynolds averaging. The MRD analysis leads to average (co)variances at a given timescale, within the selected record of the original time series. In fact, the average ($< \cdot_{2^i} >$) (co)variance at timescale τ can be computed as the sum of the MRD components from the smallest resolvable scale (2^1) up to scale τ. For example, considering a record of 2^M data points in the previous time series $u(t)$, the average variance at timescale $\tau = 2^{M-1}\delta t$ is:

$$< \overline{u'u'}_\tau >= \frac{\overline{u'u'}_{(1)} + \overline{u'u'}_{(2)}}{2} = \sum_{i=1}^{M-1} D_{uu}(i) = \frac{\overline{u''_{(1)}u''_{(1)}} + \overline{u''_{(2)}u''_{(2)}}}{2}$$

$u(t) \quad = \quad [1, 3, 2, 5, 1, 2, 1, 3]$

scale	$D_{uu}(n)$	$\overline{u}_{(.)}$	$\overline{u'}^2_{(.)}, \overline{u''}^2_{(.)}, \overline{u'''}^2_{(.)}$	$\overline{u'u'}_{2^n}$	$\sum_{i=1}^{n} D(i)$
n=3	0.25	2.25	0.25 0.25	1.6875	1.6875
n=2	0.3125	2.75 1.75	0.5625 0.5625 0.0625 0.0625	2.1875 0.6875	1.4375
n=1	1.125	2.00 3.50 1.50 2.0	1.00 1.00 2.25 2.25 0.25 0.25 1.00 1.00	1.00 2.25 0.25 1.00	1.125

Table A.1: Multiresolution orthogonal decomposition method applied to the time series with eight data points on the top of the table (M=3). Terms in each formulation of the MRD method, described in Section A.1.1 and Section A.1.2 respectively, are shown.

The total flux in the 2^M record, equivalent to the flux with Reynolds averaging of 2^M data points, can be computed summing all MRD components (M terms).

A.2.1 Cospectral gap

MRD analysis can be used to study the cospectral gap scale of the flow (if any), which is the timescale that separates turbulent and mesoscale fluxes of heat, moisture and momentum between the atmosphere and the surface. Using the gap timescale to calculate the eddy correlation flux reduces contamination by mesoscale motions. In Chapter 2 the presence of a cospectral gap in the MR heat flux cospectrum (Figure 2.13b), was used to validate the ~ 1 min timescale applied to evaluate the anisotropy of the Reynolds stress tensor at small scales. The level off to zero of the MR heat flux cospectrum $D_{wT}(i)$ in a specific range of scales, after the peak of transport associated with turbulence, means that those scales do not contribute to the transport of heat, and a timescale including only turbulent motions can be defined. Summing the components of the MR cospectrum up to the gap scale provides an estimate of the turbulent heat flux. However, it was noted that non-stationarity (the approximately linear trend due to the wave contribution) in the record was not removed by the MRD analysis, and the timescale obtained through the cospectral gap still included some non-turbulent scales, thus contaminating the turbulent flux estimate. Methods based on the Empirical Mode Decomposition (EMD), referred to as the Hilbert-Huang transform, seem to be better for studying non-linear and non-stationary time series (Huang et al., 1998; Wei et al., 2016). The main idea of EMD is to locally estimate a signal as a sum of a local trend and a local detail: the local trend is a low frequency part, and the local detail a superposed high frequency (Schmitt et al., 2009), thus this method might overcome the issue mentioned about Figure 2.13.

A.2.2 Anisotropy of the Reynolds stress tensor at different scales

MRD analysis can be used to know how much of the total (co)variance in a record is due to motions at different scales. Since MRD analysis is directly related to Reynolds averaging, an interesting application of the method is to study how much of the total

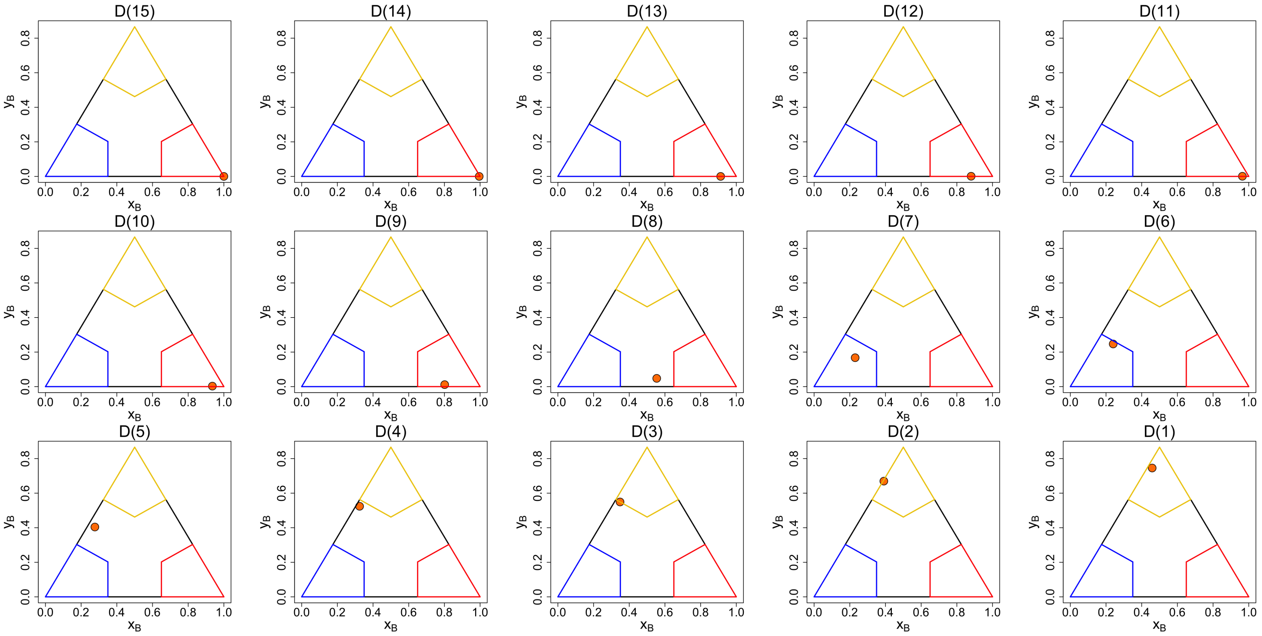

Figure A.2: Anisotropy analysis for each scale of the MR spectra of the 2^{15} data shown in Figure 2.13, corresponding to the wave observed at Dumosa. From top left to bottom right, barycentric coordinates $[x_B, y_B]$ of the Reynolds stress tensor at decreasing timescale.

anisotropy of the Reynolds stress tensor in a record is due to motions at different scales. At this purpose the multiresolution decomposition needs to be applied to each of the 6 independent terms in the Reynolds stress tensor, $[\overline{uu}, \overline{vv}, \overline{ww}, \overline{uv}, \overline{uw}, \overline{vw}]$, then build the Reynolds stress tensor at a specific scale from the corresponding MRD components and compute the barycentric coordinates defined in Section 2.3.1, Eq. 2.2. The M pairs $[x_B, y_B]$ describe the anisotropic contribution to the total Reynolds stress tensor of each scale considered in the MR (co)spectra. An example of such an analysis is shown in Figure A.2, for the data presented in Section 2.4.5 of the wave observed at Dumosa. It is worth noting that the Reynolds stress tensor made of the first component, $D(M)$ with $M = 15$, of the MR (co)spectra of $[\overline{uu}, \overline{vv}, \overline{ww}, \overline{uv}, \overline{uw}, \overline{vw}]$ falls exactly in the one-component limit, which was also observed in Klipp (2010). Indeed, the one-component contribution of the largest component of the MR spectra can be proved analytically, as it will be shown. The next smaller scales are also very close to the one-component limit, while the smallest scales are close to the isotropic limit, as expected.

Each of the M Reynolds stress tensors in Figure A.2 is not the average Reynolds stress tensor at the scale considered, made of $[<\overline{uu}>_\tau, <\overline{vv}>_\tau, <\overline{ww}>_\tau, <\overline{uv}>_\tau, <\overline{uw}>_\tau, <\overline{vw}>_\tau]$. As explained at the beginning of Section A.2, it would be so if the terms of the tensor were computed by summing all MRD components up to the scale of interest. For sake of clarity, Figure A.3 compares several estimates of anisotropy, $[x_B, y_B]$, for the same data at different scales, without the estimate already shown in Figure A.2. The several estimates at each scale 2^n are the following:

- $2^{(M-n)}$ Reynolds stress tensors are computed, where Reynolds averaging is applied

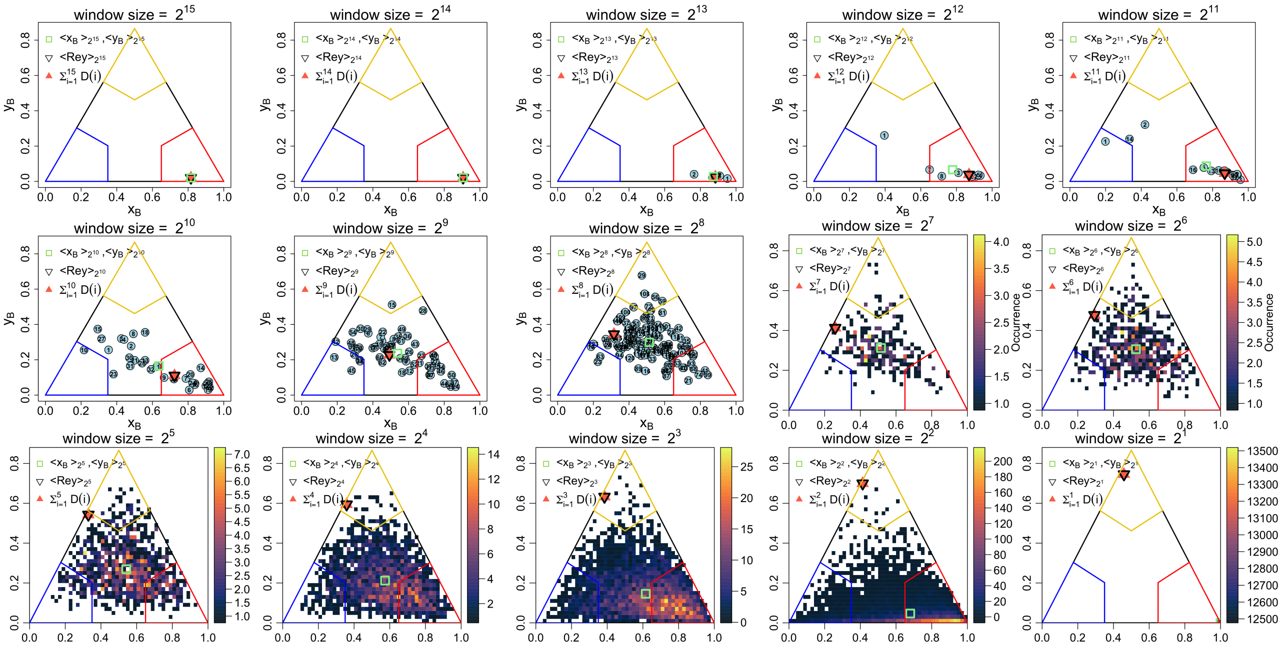

Figure A.3: Different estimates of barycentric coordinates to quantify scale dependence of Reynolds stress tensor anisotropy. They are computed according to four definitions listed in Section A.2.2. From top left to bottom right, barycentric maps with decreasing scale. In each plot, background points are the barycentric coordinates of all Reynolds stress tensors in the record, obtained by averaging over a window of 2^i data points (for a better visualization, occurrence is shown when the number of Reynolds stress tensors is larger than $2^{(15-8)} = 128$.

over windows of size 2^n data points. The $2^{(M-n)}$ pairs of barycentric coordinates are computed (background points in Figure A.3);

- $2^{(M-n)}$ Reynolds stress tensors are computed, where Reynolds averaging is applied over windows of size 2^n data points. The $2^{(M-n)}$ pairs of barycentric coordinates are computed and anisotropy is estimated by averaging each coordinate over all pairs, $[< x_B >_{2^n}, < y_B >_{2^n},]$ (green square in Figure A.3);
- $2^{(M-n)}$ lists of $[\overline{uu}, \overline{vv}, \overline{ww}, \overline{uv}, \overline{uw}, \overline{vw}]$ are computed, where Reynolds averaging is applied over windows of size 2^n data points. Each term is averaged over the $2^{(M-n)}$ lists and the average Reynolds stress tensor, $< Rey >_{2^n}$, is built, as well as the corresponding pair of barycentric coordinates (black triangle in Figure A.3);
- each term of the Reynolds stress tensor is computed as the sum of the components of the corresponding MR spectra up to scale 2^n,$\sum_{i=1}^{n} D(i)$, and the corresponding pair of barycentric coordinate is computed (orange triangle in Figure A.3).

As expected from the discussion at the beginning of Section A.2, barycentric coordinates estimated from $< Rey >_{2^n}$ and $\sum_{i=1}^{n} D(i)$ are equivalent. Instead, it is worth noting that each of the 2^{M-1} Reynolds stress tensors obtained by applying Reynolds averaging over windows of size 2^1 data points falls exactly in the one-component limit (bottom right panel in Figure A.3), and thus also $[< x_B >_{2^n}, < y_B >_{2^n},] = [1, 0]$.

One-component contribution to the total Reynolds stress tensor

Both the Reynolds stress tensor obtained from the largest scale of the MR (co)spectra, D(M) (top left panel in Figure A.2), and the 2^{M-1} Reynolds stress tensors obtained by applying Reynolds averaging over windows of size 2^1 data points (bottom right panel in Figure A.3), are characterized exactly by a one-component anisotropy. These Reynolds stress tensors have in common that are derived by pairs of fluctuations equal in magnitude with opposite sign, such as:

$$u=[u_1,u_2] \xrightarrow{\overline{u'}=0} u'=[-A,A] \qquad \overline{u'u'}=A^2 \quad \overline{u'v'}=AB \quad \overline{u'w'}=AC \tag{A.1}$$

$$v=[v_1,v_2] \xrightarrow{\overline{v'}=0} v'=[-B,B] \qquad \overline{v'v'}=B^2 \tag{A.2}$$

$$w=[w_1,w_2] \xrightarrow{\overline{w'}=0} w'=[-C,C] \qquad \overline{w'w'}=C^2 \tag{A.3}$$

In fact, according to the MRD formulation of Section A.1.2, $\left(\overline{u}_{(2)}-\overline{u}_M\right)=-\left(\overline{u}_{(1)}-\overline{u}_M\right)$ and $D(M)$ can be interpreted as the second moment about the mean of the record $\left[\left(\overline{u}_{(1)}-\overline{u}_M\right),-\left(\overline{u}_{(1)}-\overline{u}_M\right)\right]$. By using the definition of the normalized anisotropic Reynolds stress tensor, also adopted in Chapter 2, $b_{ij}=\frac{a_{ij}}{2k}=\frac{\overline{u_i'u_j'}}{2k}-\frac{1}{3}\delta_{ij}$, anisotropy is analysed by studying the second and third invariant ($II=-\frac{1}{2}b_{ij}b_{ji}, III=\frac{1}{3}b_{ij}b_{jk}b_{ki}$) of the following tensor:

$$\begin{pmatrix} \frac{A^2}{A^2+B^2+C^2}-\frac{1}{3} & \frac{AB}{A^2+B^2+C^2} & \frac{AC}{A^2+B^2+C^2} \\ \frac{AB}{A^2+B^2+C^2} & \frac{B^2}{A^2+B^2+C^2}-\frac{1}{3} & \frac{BC}{A^2+B^2+C^2} \\ \frac{AC}{A^2+B^2+C^2} & \frac{BC}{A^2+B^2+C^2} & \frac{B^2}{A^2+B^2+C^2}-\frac{1}{3} \end{pmatrix}$$

The one-component anisotropic state is characterised by $-2II=\frac{2}{3}$ and $3III=\frac{2}{9}$, which satisfy the axisymmetric relation $III=\pm 2\left(\frac{-II}{3}\right)^{\frac{3}{2}}$. These values of II and III are exactly the invariants of the previous tensor, as it will be shown.

$$\begin{aligned}
&-2II=b_{ij}b_{ji}=b_{1j}b_{j1}+b_{2j}b_{j2}+b_{3j}b_{j3}=\\
&\quad=\left(\frac{A^4}{(A^2+B^2+C^2)^2}+\frac{1}{9}-\frac{2}{3}\frac{A^2}{A^2+B^2+C^2}\right)+\frac{(AB)^2}{(A^2+B^2+C^2)^2}+\frac{(AC)^2}{(A^2+B^2+C^2)^2}+\\
&\quad+\left(\frac{B^4}{(A^2+B^2+C^2)^2}+\frac{1}{9}-\frac{2}{3}\frac{B^2}{A^2+B^2+C^2}\right)+\frac{(AB)^2}{(A^2+B^2+C^2)^2}+\frac{(BC)^2}{(A^2+B^2+C^2)^2}+\\
&\quad+\left(\frac{C^4}{(A^2+B^2+C^2)^2}+\frac{1}{9}-\frac{2}{3}\frac{C^2}{A^2+B^2+C^2}\right)+\frac{(AC)^2}{(A^2+B^2+C^2)^2}+\frac{(BC)^2}{(A^2+B^2+C^2)^2}=\\
&\quad=\left(\frac{A^4+B^4+C^4}{(A^2+B^2+C^2)^2}+\frac{3}{9}-\frac{2}{3}\frac{A^2+B^2+C^2}{A^2+B^2+C^2}\right)+\frac{2(AB)^2+2(AC)^2+2(BC)^2}{(A^2+B^2+C^2)^2}=\\
&\quad=-\frac{1}{3}+\frac{A^4+B^4+C^4}{(A^2+B^2+C^2)^2}+\frac{2(AB)^2+2(AC)^2+2(BC)^2}{(A^2+B^2+C^2)^2}=-\frac{1}{3}+\frac{(A^2+B^2+C^2)^2}{(A^2+B^2+C^2)^2}=\\
&\quad=\frac{2}{3}
\end{aligned}$$

$$
\begin{aligned}
3III &= b_{ij}b_{jk}b_{ki} \overset{b_{ij}=b_{ji}}{=} b_{ij}b_{ik}b_{jk}\\
&= \sum_{k=1}^{3}\sum_{(i=j)i=1}^{3} b_{ii}b_{ik}b_{ki} + \sum_{k=1}^{3}\sum_{(i=1)j=2}^{3} b_{1j}b_{jk}b_{k1} + \sum_{k=1}^{3}\sum_{(i=2)j=2}^{3} b_{2j}b_{jk}b_{k2} + \sum_{k=1}^{3}\sum_{(i=3)j=2}^{3} b_{3j}b_{jk}b_{k3} =\\
&\overset{b_{ij}=b_{ji}}{=} b_{11}^3 + b_{11}b_{12}^2 + b_{11}b_{13}^2 + b_{22}^3 + b_{22}b_{21}^2 + b_{22}b_{23}^2 + b_{33}^3 + b_{33}b_{31}^2 + b_{33}b_{32}^2 +\\
&+ b_{12}^2b_{11} + b_{12}^2b_{22} + b_{12}b_{13}b_{23} + b_{13}^2b_{11} + b_{13}b_{12}b_{32} + b_{13}^2b_{33} +\\
&+ b_{21}^2b_{11} + b_{21}^2b_{22} + b_{21}b_{23}b_{13} + b_{23}b_{21}b_{31} + b_{23}^2b_{22} + b_{23}^2b_{33} +\\
&+ b_{32}b_{31}b_{21} + b_{32}^2b_{22} + b_{32}^2b_{33} + b_{31}^2b_{11} + b_{31}b_{32}b_{12} + b_{31}^2b_{33} =\\
&\overset{b_{ij}=b_{ji}}{=} \left(b_{11}^3 + b_{22}^3 + b_{33}^3\right) + \left(3b_{12}^2b_{11} + 3b_{12}^2b_{22}\right) + 6b_{12}b_{13}b_{23} + \left(3b_{23}^2b_{22} + 3b_{23}^2b_{33}\right) + \left(3b_{31}^2b_{11} + 3b_{31}^2b_{33}\right)\\
&= \left(\frac{A^6+B^6+C^6}{(A^2+B^2+C^2)^3} - \frac{3}{27} - \frac{(A^4+B^4+C^4)}{(A^2+B^2+C^2)^2} + \frac{3}{9}\frac{(A^2+B^2+C^2)}{(A^2+B^2+C^2)}\right) +\\
&+ \left(\frac{3A^2B^2A^2}{(A^2+B^2+C^2)^3} - \frac{A^2B^2}{(A^2+B^2+C^2)^2} + \frac{3A^2B^2B^2}{(A^2+B^2+C^2)^3} - \frac{A^2B^2}{(A^2+B^2+C^2)^2}\right) +\\
&+ \frac{6A^2B^2C^2}{(A^2+B^2+C^2)^3} +\\
&+ \left(\frac{3B^2C^2B^2}{(A^2+B^2+C^2)^3} - \frac{B^2C^2}{(A^2+B^2+C^2)^2} + \frac{3B^2C^2C^2}{(A^2+B^2+C^2)^3} - \frac{B^2C^2}{(A^2+B^2+C^2)^2}\right) +\\
&+ \left(\frac{3A^2C^2A^2}{(A^2+B^2+C^2)^3} - \frac{A^2C^2}{(A^2+B^2+C^2)^2} + \frac{3A^2C^2C^2}{(A^2+B^2+C^2)^3} - \frac{A^2C^2}{(A^2+B^2+C^2)^2}\right) =\\
&= \frac{(A^2+B^2+C^2)^3}{(A^2+B^2+C^2)^3} - \frac{(A^2+B^2+C^2)^2}{(A^2+B^2+C^2)^2} - \frac{1}{9} + \frac{3}{9} =\\
&= \frac{2}{9}
\end{aligned}
$$

The present work combines experimental and numerical analyses to improve current understanding of turbulence in stably stratified flows.

An extensive literature review is presented on the mechanisms governing turbulence under stratified conditions, with a special focus on the Richardson number parameter, as it is often adopted as a switch to turn turbulence modelling on/off. Anisotropization of turbulence is investigated, as it is found to be an important mechanism for turbulence survival at any Richardson number, but usually overlooked in turbulence parameterizations.

For this purpose, an experimental dataset previously collected over an Alpine glacier is used, with a focus on the anisotropy of the Reynolds stress tensor, as the scientific community has recently shown improvements in the description of the atmospheric surface layer by taking this aspect into account. Different sources leading stresses to deviate from the isotropic limit are explored, as well as energy exchanges across scales and between kinetic and potential reservoirs, in order to identify the main processes that should be included in turbulence parameterizations to properly represent anisotropic turbulence under stable conditions.

High-resolution numerical simulations are then performed with the Weather Research and Forecasting (WRF) model to evaluate different PBL parameterizations in reproducing specific stable atmospheric conditions developing over complex terrain, and their influence on the local circulation. For this purpose, two wintertime case studies in a basin-like area of an Alpine valley are investigated. Both are fair-weather episodes with weak synoptic forcing and well-developed diurnal local circulations, differing by the thermal stratification in the basin. In particular, the influence of thermal stratification on the outbreak of a valley-exit wind coming from a tributary valley is investigated, and the influence of such type of flows on turbulence anisotropy in stably stratified conditions is discussed for future investigations.

Federica Gucci